ORGANIC RADICAL POLYMERS FOR ENERGY STORAGE

A Dissertation

by

SHAOYANG WANG

Submitted to the Office of Graduate and Professional Studies of
Texas A&M University
in partial fulfillment of the requirements for the degree of

DOCTOR OF PHILOSOPHY

Chair of Committee,	Jodie L. Lutkenhaus
Committee Members,	Perla B. Balbuena
	Yossef A. Elabd
	Lei Fang
Head of Department,	Micah J. Green

December 2020

Major Subject: Chemical Engineering

ABSTRACT

Organic radical polymers were studied from two aspects – electron/ion transfer during the reduction-oxidation reaction and their application as battery electrodes. The former revealed fundamental reaction mechanisms that govern electrochemical behaviors of the organic radical polymers, while the latter tackled practical issues of electrode dissolution by a synthetic approach.

The doping mechanism of nitroxide radical polymer PTMA was quantitatively investigated using quartz crystal microbalance with dissipation monitoring (EQCM-D) during electrochemical processes. Results showed that two doping mechanisms exist – doping by lithium expulsion and anion uptake. The relative dominance of one over the other was controlled by anion type, electrolyte concentration, and timescale. These results could apply in any scenario in which electrolyte is in contact with a nonconjugated redox-active polymer and present a means of quantifying doping effects.

A one-step post-synthetic, carbon-compatible crosslinking method was developed to effectively crosslink the PTMA electrode and prevent its dissolution. The highest electrode capacity of 104 mAh g^{-1} (*vs*. a theoretical capacity of 111 mAh g^{-1}) was achieved by introducing 1 mol% of the crosslinker, whereas the highest capacity retention (99.6%) was obtained with 3 mol% crosslinker. Both lithium expulsion and anion uptake were observed in doping, and the dominance was related to crosslinking density (i.e. free volume) in the electrode. This study indicated the importance of

forming a network using a minimum amount of crosslinker, persevering radical content during crosslinking, and allowing enough free volume for electrolyte penetration.

The electron and ion transfer mechanism of conjugated radical polymers (CRPs) with intentionally varied radical loadings (0, 25 or 100%) was studied to understand their inferior capacity compared to their nonconjugated partners. Results showed that the electron transfer shifted from delocalized electron transfer to localized electron hopping under higher radical loading. The extent of internal charge transfer between the conjugated backbone and the pendant radical was dominated by the radical loading. Doping occurred by exchanging one anion and one solvent molecule for every electron transferred in the CRP with 100% radical loading. For future design, the trade-off between radical loading and electronic conductivity need to be balanced.

DEDICATION

This work is dedicated to my parents, who have raised me to be the person I am today.

ACKNOWLEDGEMENTS

I sincerely thank my committee chair, Prof. Lutkenhaus, for giving me the opportunity to grow as a researcher in her laboratory and for supporting me through all the hard situations. Thanks also go to my committee members, Prof. Balbuena, Prof. Elabd and Prof. Fang for their time and helpful feedback throughout my Ph.D.

I also thank all the members in the Lutkenhaus lab for their selfless help and strong sense of responsibility to maintain a safe and productive work area. In particular, I would like to thank Dr. Fei Li for all the guidance and training since I started as a first-year Ph.D. student. Thanks also go to my closest friends and lab mates, Fei Li, Yanpu Zhang, Yilan Ye, Ian Echols, Ting Ma, and Junyeong Yun for making my life in College Station enjoyable and memorable. I thank my best friends Lin Qu and Yi Teng for their accompanies since our high school.

I thank our collaborators, Prof. Gregory Fuchs and Prof. Christopher Ober from Cornell University, for conducting measurements and providing materials for us. I thank Dr. Archana Jaiwal and Dr. Matthew Dixon from Nanoscience Instrument for their assistance with the EQCM-D. I deeply thank Dr. Jacob Ketter for his knowledge on electrochemistry, which helped me understand a key issue in my EQCM-D project.

Finally, my mother and father have my deepest thanks for their mental and financial support throughout my study in the U.S. in the past ten years. Without them, I would not be able to pursue my career as a scientist. I also thank my boyfriend for his love, patience and encouragement through all this time. Thanks for coming into my life.

CONTRIBUTORS AND FUNDING SOURCES

Contributors

This work was supervised by a dissertation committee consisting of Professor Jodie L. Lutkenhaus, Professor Perla B. Balbuena and Professor Yossef A. Elabd of the Department of Chemical Engineering, and Professor Lei Fang of the Department of Chemistry.

The solid-state electron paramagnetic resonance (EPR) data in Section 3 was provided by Albert M.G. Park and Professor Gregory D. Fuchs of School of Applied and Engineering Physics at Cornell University. In Section 4, the conjugated radical polymers studied was provided by Yiren Zhang and Professor Christopher K. Ober of the Department of Materials Science and Engineering at Cornell University. The cyclic voltammogram of the polythiophene (P3HT) thin film in electrochemical quartz crystal microbalance with dissipation (EQCM-D) was provided by Ratul M. Thakur. The EQCM-D data and the corresponding cyclic voltammogram of the radical containing polythiophene (P3HT-TEMPO-100) was obtained by Alexandra D. Easley.

All other work conducted for the dissertation was completed by the student independently.

Funding Sources

Graduate study was supported by grant DE-SC0014006 funded by the US Department of Energy, Office of Science.

NOMENCLATURE

CRP	Conjugated Radical Polymer
EPR	Electron Paramagnetic Resonance
EQCM-D	Electrochemical Quartz Crystal Microbalance with Dissipation
GMA	Glycidyl Metharylate
P3HT	Polythiophene
PTMA	Poly(2,2,6,6-tetramethylpiperidinyloxy-4-yl) methacrylate
TEMPO	2,2,6,6-tetramethyl-1-piperidinyloxy
ORB	Organic Radical Battery
T_g	Glass Transition Temperature

TABLE OF CONTENTS

Page

LIST OF FIGURES

Page

LIST OF TABLES

Page

1. INTRODUCTION

1.1. Introductory Remarks

In recent years, organic radical polymers have received much attention as active materials for battery electrodes.[1] Compared to conventional lithium metal oxide electrodes, organic radical polymers offer fast charging, high synthetic flexibility and less environmental impact. Organic radical polymers are electrochemically active owing to the reversible reduction-oxidation (redox) reaction of their pendant radical groups attached to nonconjugated backbones.[2] They have theoretical capacities of >100 mAh g^{-1},[3-5] comparable to that of current Li-ion battery cathode materials.[6, 7] Also, the singly occupied molecular orbitals in the radical groups allows rapid charging-discharging (as high as 50 C, where 1 C is the current required to discharge a battery in one hour),[3, 8, 9] because the redox reaction does not involve bond breaking or formation. The steric (and/or) resonance effects protect the radical from side reactions and lead to exceptional stability (more than 1000 cycles).[3, 4]

So far, the best-studied organic radical polymer is poly(2,2,6,6-tetramethylpiperidinyloxy-4-yl methacrylate) (PTMA). This redox-active polymer consists of stable nitroxyl radical groups (2,2,6,6-tetramethyl-1-piperidinyloxy, TEMPO) attached to a poly(methyl methacrylate) backbone. Nakahara et al. demonstrated the first application of PTMA as a cathode material in 2002.[10] The redox reaction of PTMA is shown in **Figure 1-1**. Upon oxidation or charging, the neutral TEMPO radical transfers an electron to the current collector, resulting in an oxoammonium cation. Simultaneously, anions dope the polymer cathode to maintain charge neutrality. Upon reduction or discharge, the polymer is de-doped, and the neutral TEMPO radical is retrieved.

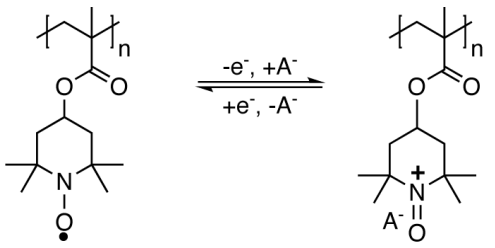

Figure 1-1. Schematic representation of the PTMA redox reaction. PTMA undergoes oxidation by doping, converting the neutral organic radical to an oxoammonium cation. A^- symbolizes a generic anion.

Although promising, there are several challenges that hinders the commercialization of organic radical batteries (ORBs, batteries using organic radical polymer as the electrode). These issues include 1) low capacity compared to that of lithium metal oxide, 2) insulating nature of the polymer film, 3) electrode dissolution in the electrolyte, and 4) limited understanding of the fundamental electron and mass transfer (i.e. doping) mechanism. Most previous research tackled issue 1-3 through modifying the synthesis routine and materials processing technique. A few studies characterized the electron transfer mechanism of PTMA during redox reaction, but the mass transfer process remains unclear, especially for the mass transfer mechanism.

This work presents fundamental studies for homogenous organic radical polymers, organic radical polymer networks, and conjugated radical polymers, with an emphasis on electron and ion transfer during redox reactions. The doping mechanism of homogeneous PTMA was investigated using electrochemical quartz crystal microbalance with dissipation (EQCM-D), which enabled in situ monitoring of mass changes on the polymer electrodes. PTMA dissolution was later tackled by crosslinking. The doping mechanism of PTMA network under various crosslinking density was also investigated using EQCM-D. For conjugated radical polymers

(CRPs), in which the pendant radicals are attached to a conjugated backbone, the internal electron transfer between the π electrons in the conjugated backbone and the pendent radical was studied, and the doping mechanism in the CRP was also observed using EQCM-D. These studies provided critical knowledge of the fundamentals of their redox reaction, which will guide future design of the polymer electrodes and aid their commercialization.

1.2. Synthesis

The synthetic flexibility of organic radical polymers enables numerous molecular designs to achieve desired electrochemical properties.[11] Significant efforts have been dedicated to optimize the synthesis routine of PTMA and develop organic radical polymers with novel molecular structure. The main purposes for these synthetic modifications are: 1) developing controlled radical polymerization for PTMA[12, 13], and 2) improving specific capacity.[14-19]

In early studies, PTMA was synthesized from free radical polymerization of 2,2,6,6-tetramethylpiperidine methacrylate monomer (TMPM) followed by oxidation using either meta-chloroperoxybenzoic acid (mCPBA) or hydrogen peroxide (H_2O_2).[10, 20] PTMA generated from free radical polymerization usually exhibit a wide range of molecular weight distribution. This is problematic because polymers with low molecular weight are prone to dissolution in the electrolyte, causing capacity fade in the batteries.

Thus, controlled radical polymerization has been developed for PTMA synthesis to reach a narrow molecular weight distribution. Boudouris et al. first synthesized PTMA from reversible addition-fragmentation chain transfer (RAFT).[13] Prior to oxidation using mCPBA, the RAFT terminus was removed using azobisisobutyronitrile (AIBN). Gohy et al. demonstrated PTMA synthesis using atom transfer radical polymerization (ATRP).[12] Both methods yield PTMA with

a low polydispersity (D < 1.2).[12, 13] Moreover, these controlled radical polymerization technique enables the synthesis of radical containing block copolymers that phase-separate upon annealing. Using ATRP, Gohy et al. further synthesized crosslinkable PTMA-b-poly(styrene) (PTMA-b-PS) diblock copolymer[21]; Boudouris et al. later incorporated an electro-active block into ordered nanostructures by synthesizing polydimethylsiloxane-b-PTMA (PDMS-b-PTMA)[22]; Ober et al. observed a cylindrical morphology in a block copolymer containing PTMA and fluorinated methacrylate.[23] Thus, adding a second polymer block to the electro-active moiety provides a new pathway to control the electrode structure at the nanoscale.

Besides controlled radical polymerization, a lot of synthetic modifications aimed at improving the capacities.[14-19] The first approach is to increase the radical concentration in the organic radical polymer. Ideally, if every repeating unit has an active free radical (i.e., 100% radical concentration), the charge storage capacity in the polymer is maximized and equal to its theoretical capacity. However, the oxidation step typically yields PTMA with 65 to 81% radical concentration.[17, 24, 25] Since the redox-active radical species are reactive toward carbon centered radicals generated by the initiator, direct radical polymerization of the radical-bearing monomer is problematic and requires special synthesis condition.[11] Nesvadba et al. developed group-transfer polymerization of 4-methacryloyloxy-TEMPO (TMA) under the presence of 1-methoxy-2-methyl-1-trimethylsilyloxypropane.[17] This method achieved 100% radical yield in the PTMA, though the polydispersity is relatively high (PDI > 3).[17] The Nishide group also demonstrated successful anionic polymerization of TMA using methyl methacrylate-capped 1,1-diphenylhexylithium as the initiator.[16] The polymer product has a radical concentration over 98% and a low polydispersity (PDI < 1.1).[16]

Other approaches to improve the electrode capacity are reducing the molecular weight of TEMPO-bearing repeating unit, and preventing polymer dissolution through crosslinking.[12, 14, 15, 18, 19] The Nishide group attached the TEMPO radical to a five-membered proxyl ring with a polyether backbone.[18] This synthetic modification towards a smaller ring and simpler backbone structure compared elevated the theoretical specific capacity to 147 mAh g^{-1}.[18] Crosslinking is also an effective way to maintain capacity as it prevents the organic electrode dissolution and thus capacity fade. In 2007, Suga et al. reported photo-crosslinkable TEMPO-substituted polynorbornenes.[14] More recently, Nakamura et al. obtained a redox-active gel through free radical polymerization of TMPM and a crosslinker, ethylene glycol dimethacryalte (EDGMA).[15]

1.3. Charge Transfer Mechanism of Organic Radical Polymers*

Understanding the reduction-oxidation mechanism of macromolecular radicals is important to applications in batteries and data storage. However, only now is the community beginning to deeply understand how ions and electrons transport in these materials. Since PTMA has an insulating backbone, electron transfer is expected to occur *via* a hopping mechanism among redox centers. As described by Equation 1-1, a free electron on site $i^{\cdot}$ is transferred to a nearby cation site j^{+}. The rate of electron transfer from a neutral site to a cation site is described by Marcus theory, Equation 1-2.

---

* Modified and reprinted with permission from the American Chemical Society. https://doi.org/10.1021/acsmacrolett.0c00063 "100th Anniversary of macromolecular science viewpoint: fundamentals for the future of macromolecular nitroxide radicals" by Shaoyang Wang, Alexandra D. Easley and Jodie L. Lutkenhaus, *ACS Macro Letters*, 2020, 9(3), 358 – 370, Copyright 2020, American Chemical Society

$$i^{\cdot} + j^{+} \rightarrow i^{+} + j^{\cdot} \qquad \text{(Equation 1-1)}$$

$$k_{ET}^{ij} = \frac{V_{ij}^2}{\hbar}\left[\frac{\pi}{k_B T \lambda}\right]^{1/2} exp\left[-\frac{(\lambda+\Delta G^{\circ})^2}{4\lambda k_B T}\right] \qquad \text{(Equation 1-2)}$$

where T is temperature, V_{ij} is the electronic-coupling matrix element between site i and j, λ is the reorganization energy, ΔG° is the free energy associated with the charge-transfer reaction, and $\hbar$ and k_B is Plank's constant and Boltzmann constant, respectively.

A series of molecular simulation studies on electronic coupling and conformational changes of PTMA provides important insights to fundamental mass and electron transfer mechanisms. Kemper et al. studied the arrangement and charge transfer of amorphous PTMA oligomers using molecular dynamics (MD) simulations.[26] The authors showed that the polymer chains were well-separated due to steric hinderance between bulky nitroxyl groups.[26] This led to three types of packing motifs – head-on arrangement of nitroxyl groups, oxygen-nitrogen bond stacking, and TEMPO ring stacking.[26] The authors also focused specifically on the electronic coupling matrix element (V_{ij}) term to relate "microscopic information of electron transfer rates that depend on V_{ij} and lengths that depend on atomic separation to a macroscopic diffusion constant (D)".[26] Importantly, it was proposed that electron coupling predominantly occurs between radicals on different chains, because the distances between interchain TEMPO N-O bonds were shorter as compared to the TEMPO N-O bonds along the same chain (intrachain).[26] The effective electron transfer length was found to be 5.5 Å with nearly 85% of electron coupling occurred between radicals on different chains.[26] Regarding the accompanied mass transfer, the authors speculate that the bulky TEMPO groups create enough voids for counter ion and solvent molecules to diffuse during redox reactions.[26]

In the above study, the reorganization energy "related to geometric and dielectric relaxation during electron transfer was considered constant".[26] In a subsequent study by Kemper et al., two other terms in the Marcus theory were evaluated: the reorganization energy (λ) was calculated using density functional theory, and the energy disorder ($\Delta G_{ij}°$) was examined in terms of both steric and electrostatic effects.[27] The computed rate of charge transfer (k_{CT}) increased with increasing site disorder, decreased with larger reorganization energy, and remained stable under different temperatures.[27] This study also showed that local energetic disorder led to nearly isolated sites (or trap sites).[27] These trap sites had significantly lower energy than their neighbors and accounted for 3% of the sites under room temperature.[27] In addition, tightly coupled sites that had large electronic coupling and nearly zero energetic disorder formed effectively paired sites.[27] Under this circumstance, the stable radical hops quickly back and forth between the two sites, but this rapid hopping is not part of the bulk charge transport.[27] If the time scale to escape a pair is considerably larger than that of the intersite hopping, then the paired sites actually act as a single site.[27] The author determined that about 4% of the sites were paired and could be treated as a single site.[27]

Previous simulations centered on the Marcus theory were applied to solid state PTMA.[26, 27] In a subsequent study by Kemper et al., solvent molecules (acetonitrile) and anions (BF_4^-) were introduced into the system.[28] It was found that the TEMPO group packing in the three primary motifs identified in previous work[26] remained stable after swelling in acetonitrile, and the electronic coupling (V_{ij}) was also likely unaffected by solvent swelling.[28] The effective binding energy between TEMPO cations (oxidized form) and BF_4^- anions was evaluated through potential of mean force (PMF).[28] It was found that the binding energy decreased with higher state of charge (SOC) and that BF_4^- anions bound strongly to TEMPO cations.[28] This implies that

BF_4^- anions might complex with TEMPO cations and lead to incomplete discharge of the organic electrode unless applying a large underpotential.[28] The counterion also stabilized the cation site by more than 1 eV.[28] As a result, the TEMPO cations might be excluded from the electrical conduction network, but it does not affect the conductivity of other uncomplexed sites.[28]

Most recently, Joo et al. utilized Monte Carlo simulations to show the radial network formation in a poly(TEMPO ethylene oxide), which has a more flexible backbone as compared to PTMA.[29] They concluded that annealing of the polymer films was critical to form the percolating domains of TEMPO pendant groups and enhance conductivity once a critical radical loading is reached.[29]

To compliment the simulation work, experiments were also conducted to determine the charge and mass transport of these redox polymers. Electron transfer is described by the electron self-exchange between the stable radicals and the oxoammonium cations (k_{ex}), the heterogeneous electron transfer from the polymer electrode to the current collector (k^0), and the electron diffusion coefficient (D).

Characterization of charge transfer in organic radical species started from nitroxide-containing small molecules using chronoamperometry, cyclic voltammetry, rotating disk, and AC impedance.[4, 30] The measured heterogeneous electron-transfer rate constant (k^0) and diffusion coefficient (D) were on the order of 10^{-1}-10^{-2} cm s^{-1}, and 10^{-5}-10^{-6} cm^2 s^{-1}, respectively.[4] The electron self-exchange reaction rate constant (k_{ex}) was calculated from the diffusion coefficient and was on the order of 10^8 M^{-1} s^{-1}.[4, 31] Later, similar studies were performed on macromolecular radicals such as PTMA, and the measured k_{ex}, k^0, and D values were on the order of 10^{5-7} M^{-1} s^{-1}, 10^{-4}-10^{-6} cm s^{-1}, and 10^{-8}-10^{-10} cm^2 s^{-1}, respectively.[31] This 10^{3-4} orders of magnitude decrease of

electron transfer rate constant in polymers *vs*. small molecules is widely observed, regardless of the type of redox center, polymer chains, and electrolytes.[31]

To explain this phenomenon, Sato et al. reported the first diffusion-cooperative model for charge transport of nonconjugated redox-active polymers.[31] The authors first calculated the electron transfer rate constant and electron self-exchange rate constant using Marcus-Hush theory for monomeric species and the polymer.[31] This model is considered as a frozen-molecule model because it assumes that there is no physical movement of the chain or the redox-center.[31] The electronic coupling and the activation energy in the Marcus theory were estimated by ab initio quantum mechanics calculations.[31] The calculated kinetic parameters for the monomeric species show good agreement with the measured experimental values.[31] However, the estimated electron self-exchange rate constant is 5 orders of magnitude smaller than the experimental value, meaning that the frozen-molecule model is inappropriate to describe charge transport in nonconjugated redox-active polymers.[31]

To address the discrepancy, the diffusion-cooperative model takes Brownian motion into account by considering the physical diffusion coefficient (D_{phys}) in estimating the heterogeneous and apparent bimolecular electron self-exchange rate constants, k^0 and $k_{ex,app}$, respectively, Equations 1-3 to 1-6.[31] κ_{el} is the electron transmission coefficient, D_{phys} is the physical diffusion coefficient of redox sites, and L is the mean free distance.

$$k^0 = \kappa_{el} \frac{3D_{phys}}{2L} exp\left(-\frac{\lambda}{4k_bT}\right) \quad \text{(Equation 1-3)}$$

$$\frac{1}{k_{ex,app}} = \frac{1}{k_{ex}} + \frac{1}{k_{diff}} \quad \text{(Equation 1-4)}$$

k_{ex} is bimolecular electron self-exchange reaction rate constant and can be calculated from the Dahms – Ruff equation (Equation 1-5), where D is diffusion coefficient for electron transfer, C_E is total concentration of redox sites, and δ is site distance.

$$D = \frac{1}{6} k_{ex} C_E \delta^2 \qquad \text{(Equation 1-5)}$$

k_{diff} is physical diffusion constant and is approximated by Smoluchowski model of rigid spheres as reactants (Equation 1-6), where a is radius of the sites and N_A is Avogadro constant.

$$\frac{1}{k_{diff}} = 16\pi D_{phys} a N_A \qquad \text{(Equation 1-6)}$$

The physical diffusion coefficient refers to coupled Brownian motion of both the polymer backbones and the bound redox centers, measured using DLS.[31] Then the authors predicted the kinetics parameters for a broad series nonconjugated redox-active polymers using this diffusion-cooperative mode with good agreement.[31] Thus, the limited physical diffusion of the redox sites in swollen polymers is a key step in homogeneous and heterogeneous charge transport.[31] It is also worth mentioning that "diffusion is a percolation (i.e. random walk) process of electron hopping".[31] The diffusion of ions in the swollen polymer is in general much faster compared that of the redox sites.[31] Thus, ion diffusion should not be the rate-limiting factor in charge transfer, which is consistent with the observation that the redox reactions have been limited by electron diffusion.[32]

1.4. Electrochemical Quartz Crystal Microbalance with Dissipation (EQCM-D)

Electrochemical quartz crystal microbalance (EQCM - without dissipation monitoring) has been applied to quantify mass changes during cycling in studies of the solid electrolyte

interface in lithium-ion batteries[33], porous carbon electrode ion dynamics[34, 35], and mass transfer in electro-active polymers.[36-39] The active material to be interrogated is coated onto a metal-coated quartz crystal sensor and used as the working electrode in a three-electrode cell. The piezoelectric quartz crystal oscillates at a fundamental frequency (*f*), displaying different harmonics or overtones (f_n) under the application of an electric field.[40]

For a stiff and perfectly elastic electrode, the mass change on the electrode can be directly obtained from oscillation frequency according to the Sauerbrey model (Equation 1-7).[41] In this case, the oscillation frequency of the coating is approximately the same as the oscillation frequency of the quartz crystal.[41]

$$\Delta m = -C\frac{1}{n}\Delta f \qquad \text{(Equation 1-7)}$$

where Δm is the mass change on the sensor, C is a constant and equals 17.7 ng cm^{-2} s^{-1}, n is overtone, and Δf is the measured frequency change.

However, PTMA interacts with the liquid electrolyte such that a viscous response occurs, and the Sauerbrey equation is no longer valid. Therefore, we chose to use a Voigt model. The energy dissipation of the crystal to the environment is measured by periodically removing the electric field. The dissipation factor (*D*) is defined by the following equation[42]:

$$D = \frac{E_{dissipated}}{2\pi E_{stored}} \qquad \text{(Equation 1-8)}$$

where $E_{dissipated}$ is the energy loss after the removal of the electric field and E_{stored} is the energy stored in the oscillating crystal. The magnitude of energy decay in the oscillator depends on both the properties of the deposited layer and the contact medium.[43, 44]

1.5. Thesis Overview

In this thesis, the fundamental electron and/or mass transfer (i.e., doping) process during redox reaction was studied for 1) homogenous organic radical polymers, 2) organic radical polymer networks, and 3) conjugated radical polymers.

The doping mechanism of homogenous PTMA was studied using EQCM-D. PTMA was deposited on an EQCM-D sensor and used as the working electrode. The frequency and dissipation were measured in the EQCM-D during cyclic voltammetry at different scan rates. The same experiment was conducted using three different electrolytes to study the effect of anion type on doping. Mass and shear modulus were extracted from the EQCM-D data from the viscoelastic model. The mass exchanged per electron transfer was examined, and two doping mechanisms were proposed in Section 2. The degree of solvent participation was also characterized by a mass balance. The analysis method developed in this study could apply to other non-conjugated redox-active polymers for which electrolyte has an important role.

In Section 3, a one-step post-synthetic, carbon-compatible crosslinking method was developed to form a PTMA network and suppress electrode dissolution observed in the previous chapter. The amount of crosslinker added was varied to investigate the effect of crosslinking on swelling and electrochemical performance. Crosslinking was carried out under UV exposure with a photo-initiator or heat. The efficiency of the two crosslinking methods was evaluated by solid-state electron paramagnetic resonance. Coin cells were assembled using the crosslinked electrodes, and the cell performances were evaluated. EQCM-D was used to characterize the doping mechanism of the crosslinked electrodes with different crosslinking densities.

Finally, the electron and ion transfer mechanisms of conjugated radical polymers were studied for polythiophenes with intentionally varied TEMPO loading. Cyclic voltammetry,

galvanostatic charge-discharge, and open circuit potential were conducted to probe the electron transfer. Section 4 describes the effect of radical content on 1) electron transfer mechanism and 2) internal charge transfer between the conjugated polythiophene backbone and the TEMPO radical. The effect of polymer packing on charge transfer was also discussed. In addition, the doping mechanism in polythiophene-TEMPO was investigated using the EQCM-D.

Conclusions and general outlook for organic radical polymers were detailed in Section 5.

2. DOPING MECHANISM IN NITROXIDE RADICAL POLYMERS*

2.1. Introduction

Although there is much more understood about electron transfer[31, 45-47] and conductivity[13, 48-51] in organic radical polymers, there is significantly less understood regarding mass transfer and doping, which is equally important for identifying the overall redox mechanism. Only a few studies have focused on the effect of the electrolyte salt type on the charge transfer reaction.[28, 47] Nakahara et al. experimentally showed that anion (PF_6^- and BF_4^-) mobility strongly influenced charge transfer and electron self-exchange in swollen PTMA.[47] Using simulations, Kemper et al. found that BF_4^- stabilized and strongly bound to the oxoammonium.[28]

Describing mass transport in the polymer electrode system is complex because the organic radical polymer is swollen with electrolyte, so transport of dopant anions may occur internally or externally from the bulk electrolyte. Some amount of solvent may also be dragged into the electrode, further complicating interpretation. More importantly, since the redox-active TEMPO moieties are immobilized in the polymer, the electrons on the free radicals are the only mobile species toward the current collector. Thus, the diffusion coefficient and kinetic rate constants deduced from electrochemical measurements (such as cyclic voltammetry, chronoamperometry and AC impedance) in general describe the electron transfer mechanism. Direct evidence of mass transfer, or the doping mechanism, is hard to obtain solely from

---

electrochemical tests. Without resolving the doping mechanism, it is impossible to quantify and understand the nature of the redox reaction in real time, the physical property changes of the electrode during doping, and the influence of anion type.

Here, we quantify the real-time mass transfer of anions and solvent during the reduction and oxidation of PTMA, which allows for the separation of lithium expulsion and anion uptake in an organic radical polymer. This is accomplished using in situ electrochemical quartz crystal microbalance with dissipation monitoring (EQCM-D) during cyclic voltammetry, a method that yields the instantaneous electrode mass change and shear modulus via viscoelastic modeling. We present an analysis method for PTMA by which the mass exchanged per electron transferred is quantified, and, in some cases, the number of solvent molecules transferred can also be calculated. The effect of dopant anion type (i.e., $CF_3SO_3^-$, ClO_4^-, and BF_4^-), the degree of solvent participation, and the effect on charge storage behavior with mass transport is correlated to polymer-dopant and dopant-solvent interactions. Understanding the detailed mass and charge transport process helps to describe the redox reaction doping mechanism in organic radical polymers and adds to the discussion of the nature of electron transport, given that the two are intimately coupled. In turn, this may impact the future design of organic radical polymers for any application in which the polymer is in contact with electrolyte (organic batteries, electrochromics, sensors).

2.2. Materials and Methods

2.2.1. Materials

All chemicals were used as received from Sigma-Aldrich unless otherwise noted. 2,2'-Azeobis(2-methylpropionitrile) (AIBN) was recrystallized using methanol at reduced

temperature, and vacuum dried overnight under room temperature. *m*-Chloroperoxybenzoic acid (*m*CPBA) was first dissolved in diethyl ether, and then washed with pH 7 buffer three times, then by water and brine solution, once each. The organic extract was dried over Na_2SO_4, and the solvent was removed by rotary evaporator. The remainder was vacuum dried overnight at room temperature. Subsequently, the *m*CPBA was recrystallized using dichloromethane (DCM) at reduced temperature and vacuum dried overnight again.

2.2.2. PTMA Synthesis

PTMA was synthesized using free radical polymerization, as reported elsewhere.[10] The polymerization of 2,2,6,6-tetramethyl-4-piperidinyl methacrylate (TMPM) was initiated by AIBN in toluene. The neutral polymer product was oxidized to the stable radical form using *m*CPBA. PTMA appeared as a pale orange powder upon washing, precipitation, and drying. Some partial oxidation of the as-synthesized PTMA was observed (72.5% radical functionalization), but the neutral organic radical form should be retrieved during electrochemical cycling. The number average molecular weight of PTMA was 50,200 g/mol and the dispersity was 3.5.

2.2.3. Baseline Measurement

Gold-coated, planar AT-cut quartz crystals with a fundamental resonance frequency of 4.95 MHz were used as the substrate for EQCM-D measurements (E1 module, Biolin Scientific). A baseline for the clean crystal in static air was recorded first. Subsequently, the lithium salt electrolyte solution was pumped into the chamber at a flow rate of 150 µL/min until a stable frequency response was measured. The flow was ceased, and the crystal was allowed to equilibrate in static electrolyte for an additional 5 min, afterwards the baseline for the crystal in static electrolyte was recorded.

2.2.4. PTMA-coated Sensor Preparation

After baseline measurements, the quartz crystals were treated in an O_2-plasma etcher for 5 min, immersed in water (5): NH_4OH (1): H_2O_2 (1) by volume at 75 °C for 5 min, dried under nitrogen, and plasma-treated again for 5 min. 10 mg of synthesized PTMA was dissolved in 1 ml chloroform ($CHCl_3$, BDH) under moderate stirring for 10 min. A thin layer of PTMA was spin-coated on the substrate by adding 40 µL of the $CHCl_3$ solution of PTMA and spinning at 500 rpm for 1 minute. Scanning electron microscopy (SEM) revealed that the polymer layer was uniformly distributed on the substrate. The PTMA coated substrate was vacuum dried overnight at 50 ºC to remove any remaining solvent and moisture.

2.2.5. Estimation of PTMA Coating Thickness

The thicknesses of the PTMA coatings were estimated by measuring baselines for the bare and PTMA-coated quartz crystal in air using EQCM-D. The bare and coated baselines in air for the exact same sensor were stitched in QSoft (Biolin Scientific) and modeled in QTools (Biolin Scientific) using the Sauerbrey equation. The estimated thicknesses varied from 150 nm to 200 nm.

2.2.6. EQCM-D Measurements

A three-electrode electrochemical cell was used. The PTMA coated crystal served as the working electrode. Platinum plate and silver wire served as counter and quasi-reference electrodes, respectively. Three electrolyte solutions were used: 1) 0.5 M $LiClO_4$, 2) 0.5 M $LiCF_3SO_3$, and 3) 0.5 M $LiBF_4$ in propylene carbonate, unless otherwise stated. Electrolyte solutions were prepared and stored in an inert argon environment. All EQCM-D experiments, including the baseline measurements, were carried out in normal laboratory conditions and the temperature was kept at 25 °C in the EQCM-D chamber. The same electrolyte solution as in the

baseline measurement was pumped into the cell under the same flow rate until stable frequency and dissipation responses were measured. The PTMA-coated crystal was allowed to equilibrate in static liquid electrolyte for an additional 3 to 5 min. EQCM-D and cyclic voltammetry measurements were started at the same time. Cyclic voltammetry at different scan rates was performed using a Gamry Interface 1000. Each sample was run in the sequence of two cycles at 10 mV s^{-1}, two cycles at 25 mV s^{-1}, two cycles at 50 mV s^{-1}, and two cycles at 100 mV s^{-1}. The resting time in between each scan rate was 100 s. The "standard" experiment was therefore 8 cycles.

2.2.7. EQCM-D Data Analysis

To quantify the mass and viscoelastic property changes during electrochemical processes at the electrode surface, raw EQCM-D data was modeled using a viscoelastic Voigt model in QTools software. Voinova et al. have shown that in the Voigt model, both Δf and ΔD are functions of density (ρ), viscosity (η), elasticity (μ) and thickness (δ) of the film, and viscosity and density of the surrounding liquid.[52] QTools modeling utilizes measured Δf and ΔD and specified fluid properties to calculate film properties, which are viscosity, shear modulus and thickness (or mass). In the modeling platform, fluid density, fluid viscosity and density of the film-liquid interacting layer are three inputs and kept constant throughout. The electrolyte solutions were assumed to have a viscosity of 0.0025 kg/ms, and a density of 1200 kg/m^3 at 25 ºC, based on the properties of propylene carbonate. The density of the polymer-electrolyte interacting layer (L1) was approximated to have the same density as the electrolyte solvent, 1200 kg m^{-3}. For each sample, at least three overtones out of the third, fifth, seventh and ninth overtones were modeled to obtain reliable results. Fitting was conducted so as to provide a

minimum χ^2, while reflecting characteristic trends of the measured frequency and dissipation (**Table 2-1**).

Table 2-1. Fitting parameters inputted in EQCM-D.

Fitting Parameters:	*Minimum*	*Maximum*	*Step (Iterations)*
L1 Viscosity (kg m^{-1} s^{-1})	0.0001	0.1	50
L1 Shear (Pa)	1E5	1E7	50
L1 Thickness (m)	1E-9	1E-7	21

2.3. EQCM-D Response and Cyclic Voltammetry

Figure 2-1 shows the EQCM-D response for the third overtone of a PTMA-coated Au sensor immersed in 0.5 M $LiCF_3SO_3$ in propylene carbonate during cyclic voltammetry. The EQCM-D response tracks well with cyclic voltammetry, as the frequency and dissipation changes overlap with the redox peaks. With the exception of the first 200 s, the response was generally stable and reversible. Both the frequency and dissipation responses returned to their initial values after a complete cycle, indicating that the mass and viscoelastic property changes were recoverable on the experimental time scale.[39] The positive shift in f_3 in the first 200 s corresponds to about 14 wt% mass loss, probably a result from the dissolution of low-molecular-weight polymer. As will be discussed in the next section, cross-linked PTMA shows no such mass loss, similar to the stability in cross-linked PTMA observed elsewhere.[53]

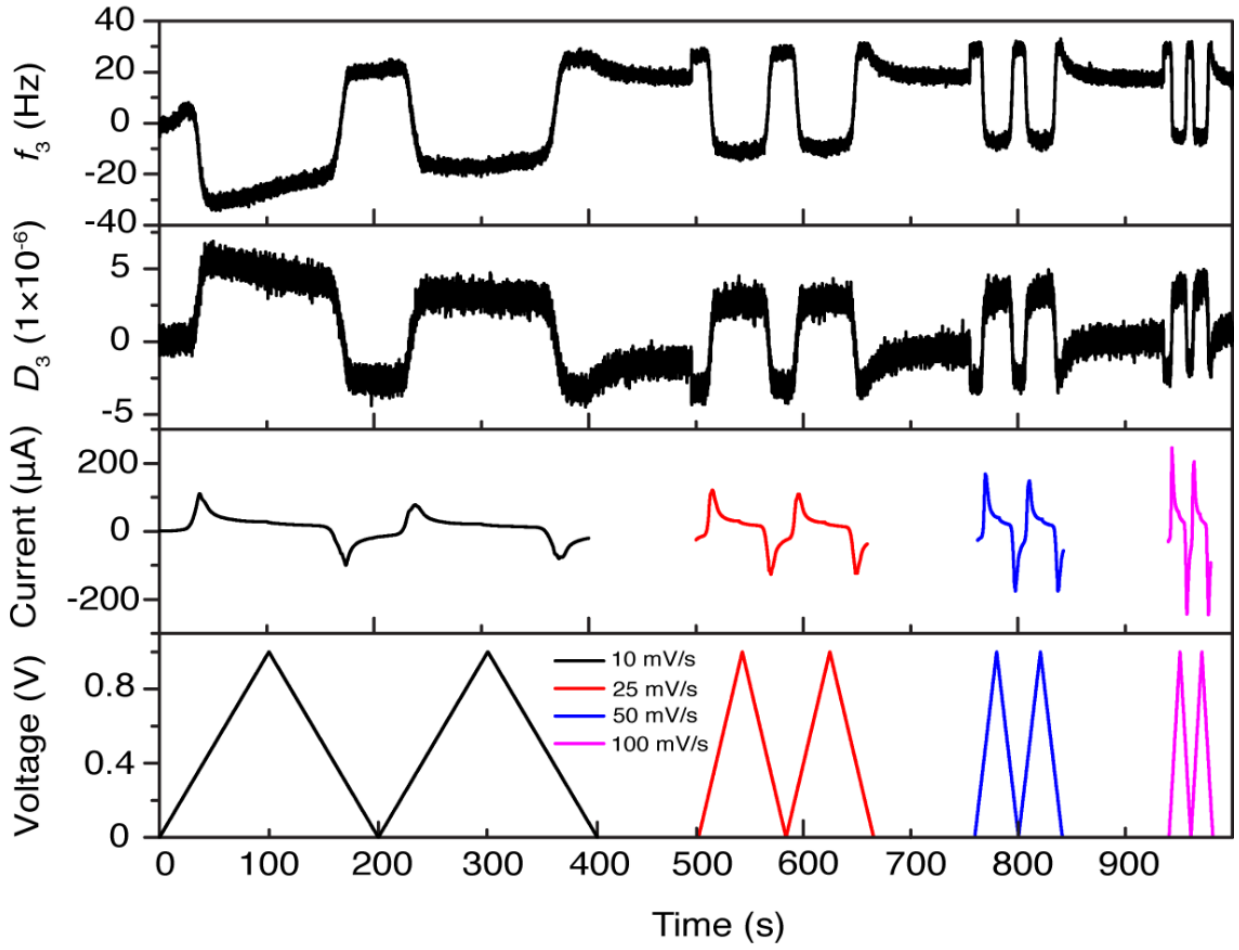

Figure 2-1. Frequency (f_3) and dissipation (D_3) responses of the third overtone from EQCM-D during cyclic voltammetry at the indicated scan rates. Two cycles at each scan rate were performed, followed by equilibration in the liquid electrolyte for 100 s.

For a closer view, the frequency and dissipation responses during oxidation and reduction from **Figure 2-1** were superimposed and shown in **Figure 2-2** with their corresponding cyclic voltammograms. The redox potential $E_{1/2}$ for PTMA was about 0.37 V *vs*. silver wire QRE, which corresponded to 3.6 V *vs*. Li/Li$^+$ (using ferrocene as a standard[21, 54]), consistent with a previous report.[10] As voltage increased from 0–1 V, PTMA oxidation occurred and f_3 decreased in a stepwise manner, indicating a qualitative increase in the mass of the electrode. This points to

the doping of PTMA, in which the neutral form of PTMA oxidizes to a cationic form with oxoammonium sites through electron transfer. To maintain charge neutrality, an anion (in this case $CF_3SO_3^-$) diffuses into the PTMA electrode, and the electrode mass increases. Concomitant with this process, D_3 increased upon oxidation, which indicated a softening of the PTMA electrode. In the reverse process, the voltage decreased from 1–0 V, and PTMA reduction occurred. Both f_3 and D_3 retraced their paths, increasing and decreasing, respectively, in a stepwise manner with little hysteresis. This correlated to a net decrease in electrode mass by the expulsion of the dopant $CF_3SO_3^-$ ions, and a simultaneous stiffening of the PTMA electrode for these conditions. Other electrolytes ($LiClO_4$ and $LiBF_4$) exhibited generally similar EQCM-D responses, as shown in **Figure 2-3**.

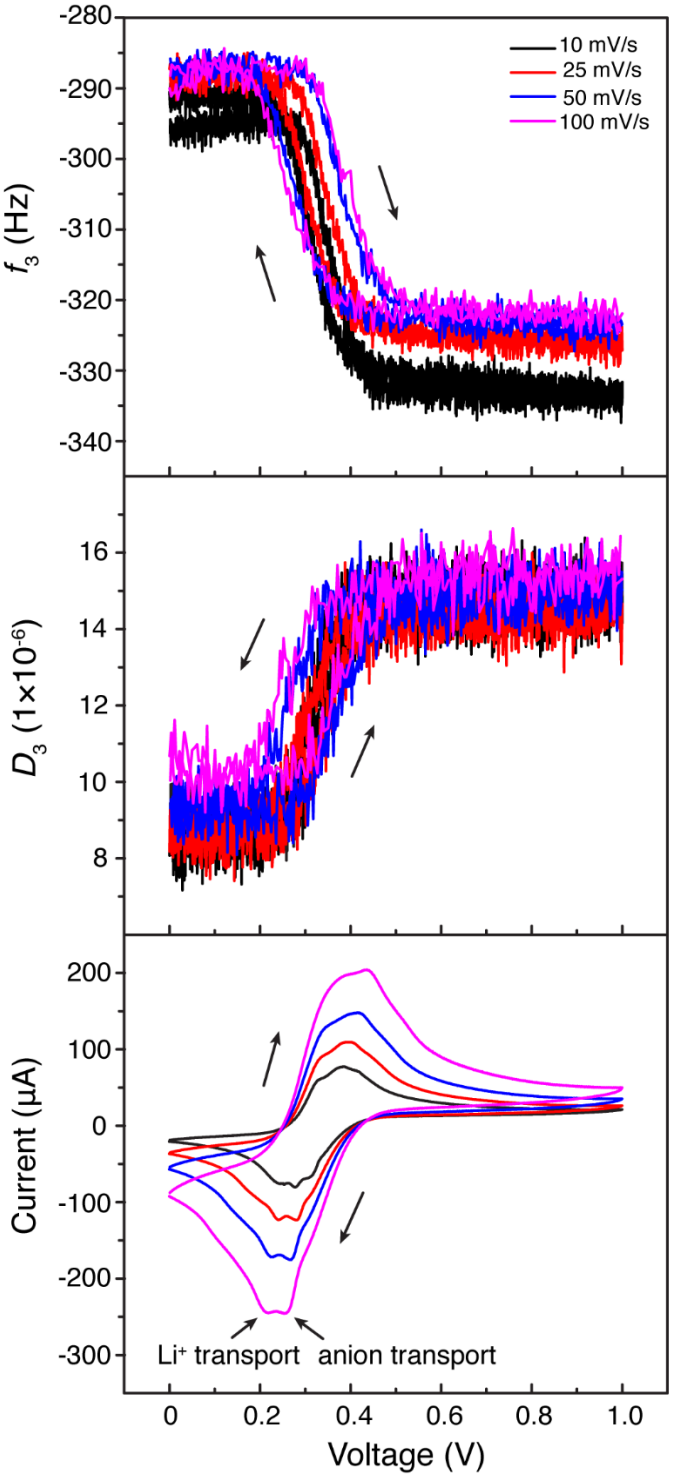

Figure 2-2. Frequency (f_3) and dissipation (D_3) responses of the third overtone from EQCM-D during cyclic voltammetry at the indicated scan rates.

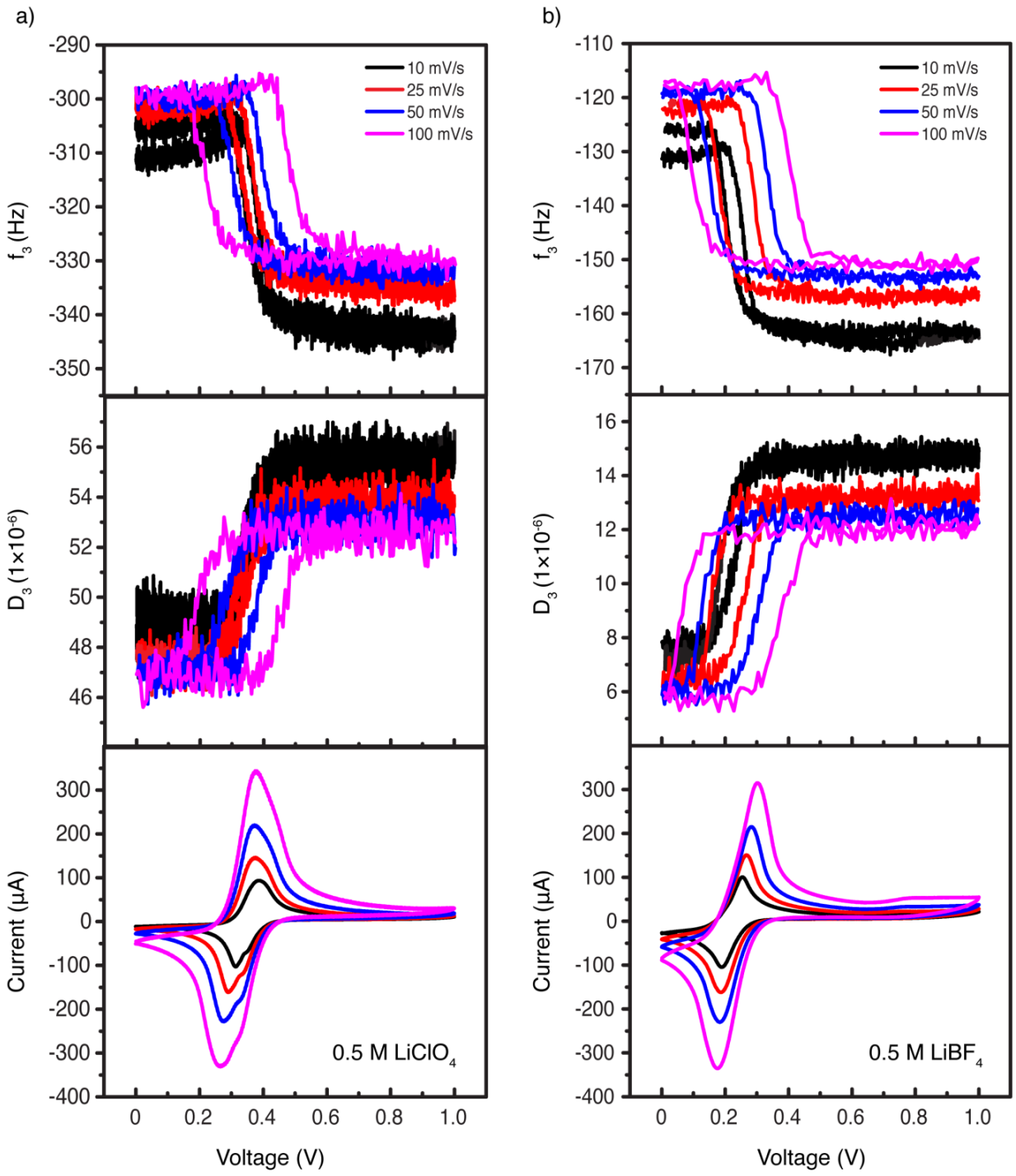

Figure 2-3. Frequency (f_3) and dissipation (D_3) responses of the third overtone from EQCM-D during cyclic voltammetry at the indicated scan rates. The working electrode was PTMA, and the electrolytes were a) 0.5 M $LiClO_4$ in propylene carbonate, and b) 0.5 M $LiBF_4$ in propylene carbonate. The potential window was 0–1 V *vs*. silver wire quasi-reference electrode (QRE). Second cycles are taken from the general sequence shown in Figure 2-1.

Although scan rate did not affect the general EQCM-D responses, some small hysteresis between oxidation and reduction steps was observed, especially at higher scan rates for all lithium salts investigated. Similar hysteretic behavior was observed in the EQCM investigation of polyaniline,[38] polyvinylferrocene,[39] and polyviologen hydrogel[37] due to the formation of a diffusion layer at higher scan rates or under different electrolyte concentrations. The magnitude of hysteresis in EQCM tracks with and mimics with the peak separation in cyclic voltammetry. In addition, the hysteresis has roughly the same magnitude as the peak separation, because the electron transfer is accompanied by ion and solvent transport, reflected as frequency (mass) change in the EQCM. In brief, the hysteresis in the QCMD signal comes from the natural hysteresis due to the electrochemical process, as mass and electron transport are coupled.

2.4. Mass, Shear Modulus and Integrated Charge

Changes in mass and viscoelastic properties of the PTMA cathode were extracted using a Voigt model applied to the EQCM-D data. **Figure 2-4** show the mass and shear modulus profiles during oxidation at various scan rates for 0.5 M $LiCF_3SO_3$. Consistent with the results of **Figure 2-2**, the mass of the PTMA cathode increased and the shear modulus decreased upon oxidation due to doping for $LiCF_3SO_3$. During reduction, the mass and shear modulus trends reversed and recovered their original values albeit with some transient hysteresis at higher scan rates.

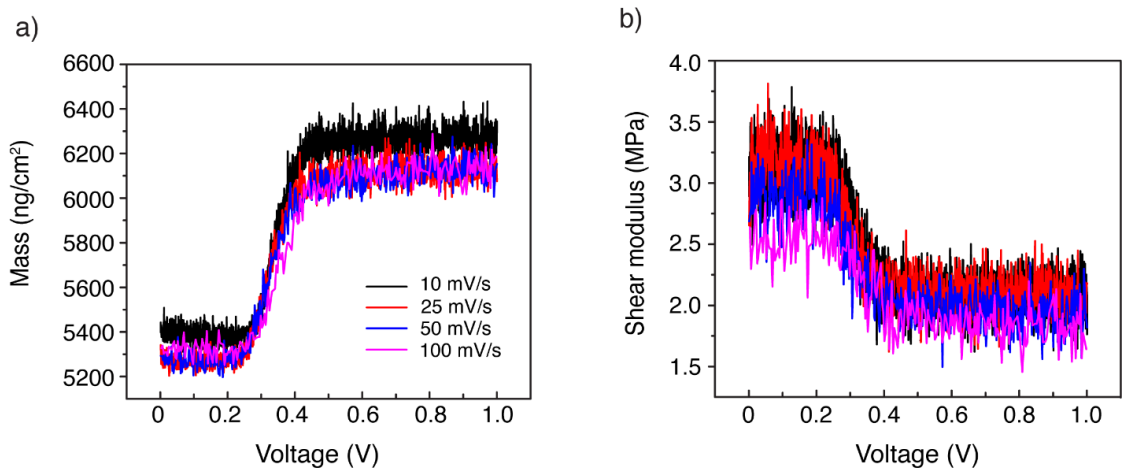

Figure 2-4. a) Mass and b) shear modulus profiles of a PTMA cathode during oxidation at all scan rates.

The net changes in electrode mass (Δm) and integrated charge (Q) during oxidation are plotted *vs*. scan rate and scan rate$^{-1/2}$ in **Figure 2-5**, **Figure 2-6** and **Figure 2-7** for 0.5 M $LiCF_3SO_3$, $LiClO_4$ and $LiBF_4$, respectively. The net mass change and integrated charge decreased with increasing scan rate. Since the experimental timescale is much shorter at higher scan rates, the redox reaction of the free radical does not have enough time to proceed to full extent, resulting in less charge and mass transfer (i.e., less participating free radicals and ions).

The mass exchange did not correlate with $v^{-1/2}$, as would have been expected for a mass-diffusion-limited process.[55] Interestingly, the integrated charge decreased as $Q \sim v^{-1/2}$, indicative of electron-diffusion-limited behavior.[55] The relationship of $Q \sim v^{-1/2}$ has also been observed for polyvinylferrocene in an aqueous electrolyte.[39] Electron-diffusion-limited behavior arises from the hopping of electrons from site-to-site, in which hopping is influenced by the diffusion of those sites and the segmental motion of the polymer chain.[31]

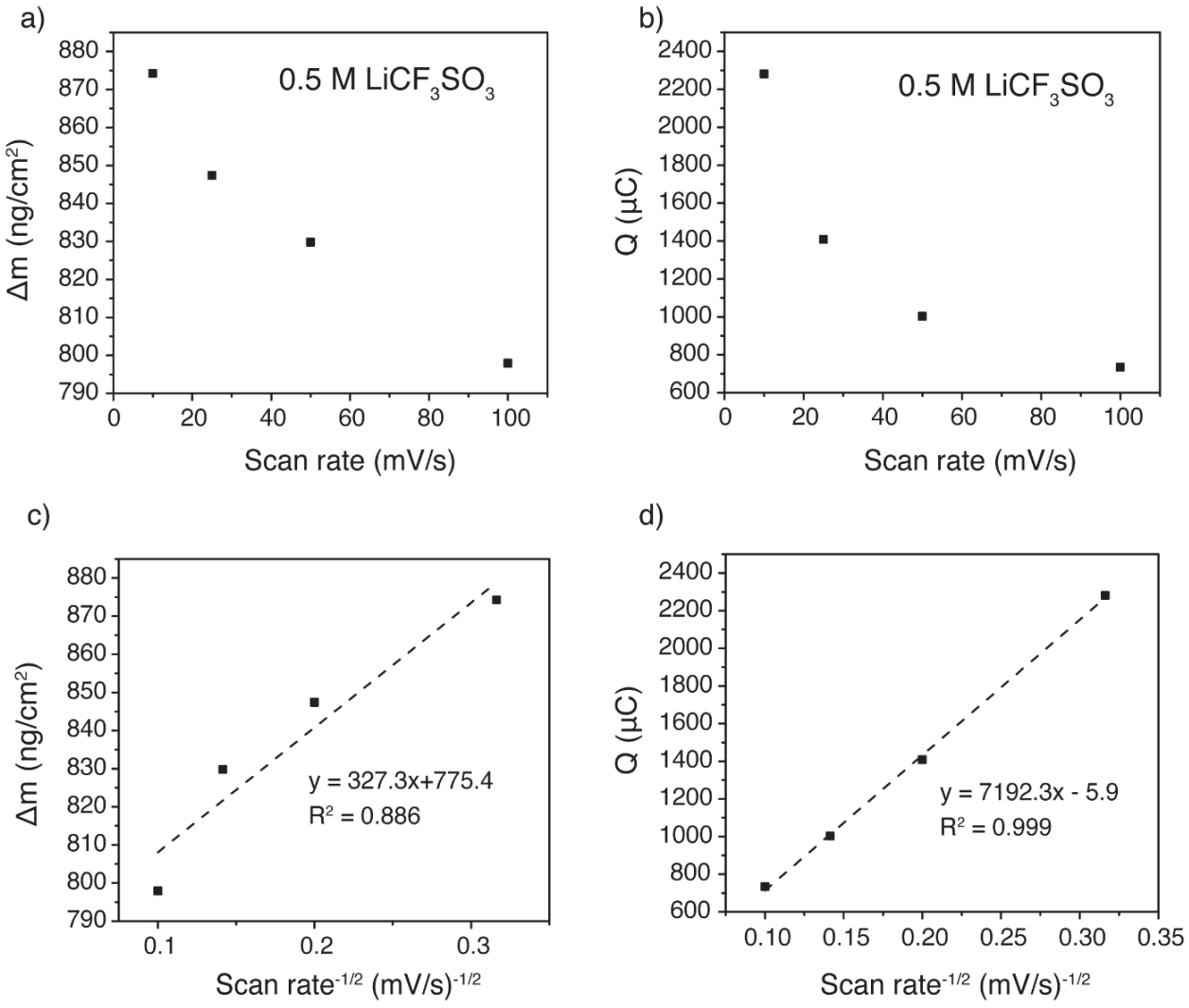

Figure 2-5. Data obtained from EQCM-D of PTMA in 0.5 M $LiCF_3SO_3$ in propylene carbonate. a) Δ*m vs*. scan rate, b) integrated charge transfer *Q vs*. scan rate for oxidation, c) Δ*m vs*. scan rate$^{-1/2}$ with linear fit, and d) *Q vs*. scan rate$^{-1/2}$ with linear fit.

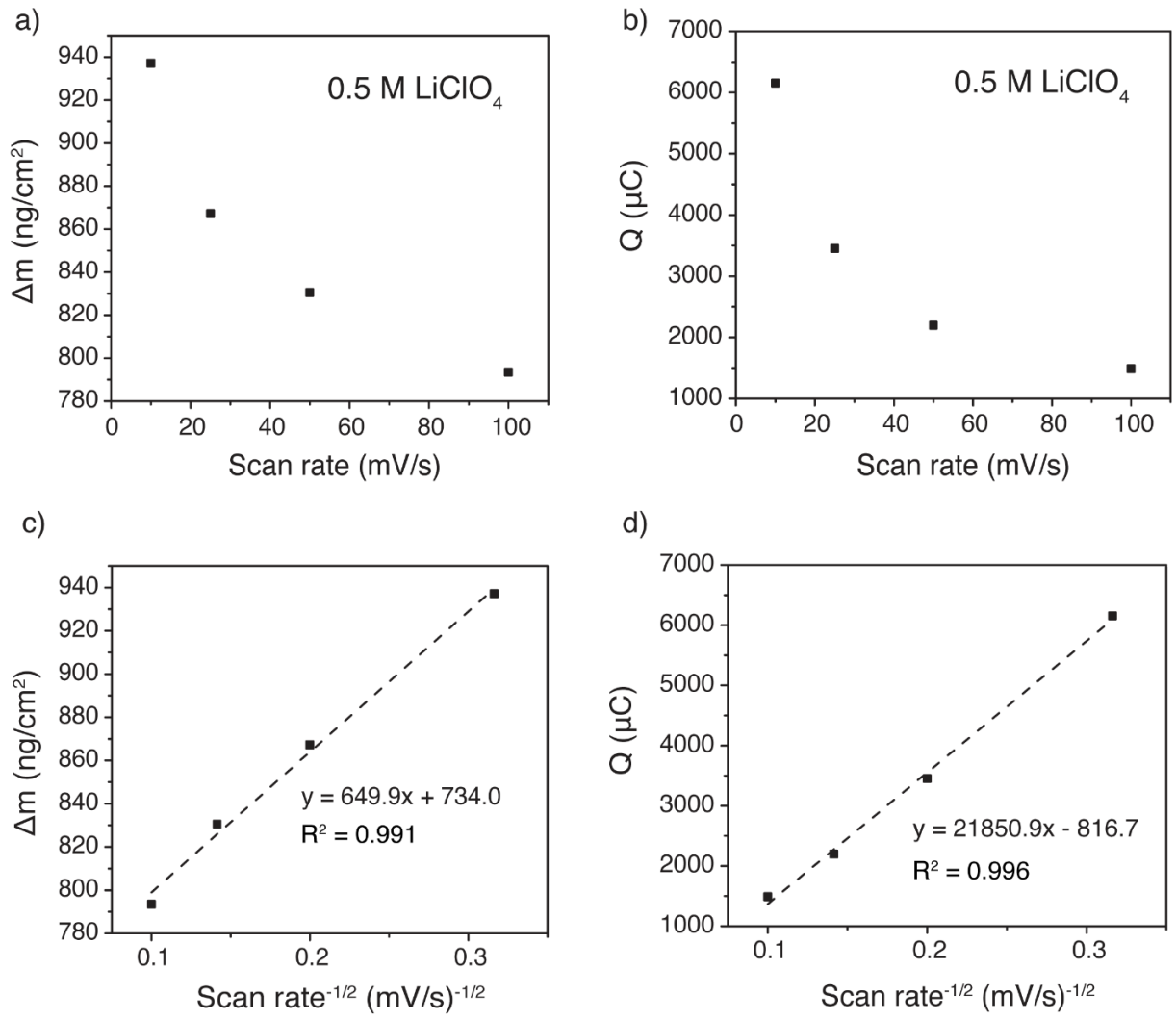

Figure 2-6. Data obtained from EQCM-D of PTMA in 0.5 M $LiClO_4$ in propylene carbonate. a) Δm *vs*. scan rate, b) integrated charge transfer Q *vs*. scan rate for oxidation, c) Δm *vs*. scan rate$^{-1/2}$ with linear fit, and d) Q *vs*. scan rate$^{-1/2}$ with linear fit.

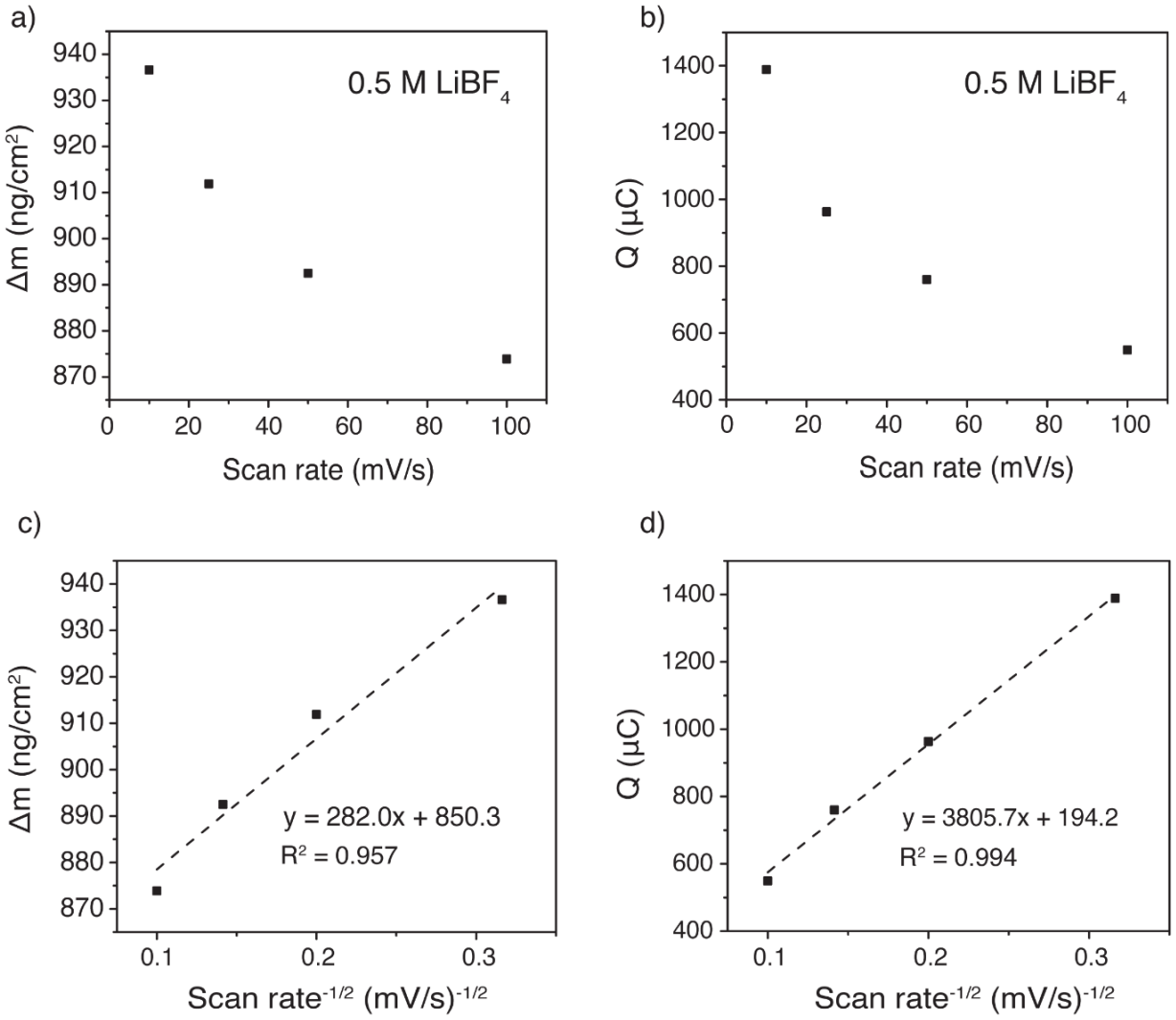

Figure 2-7. Data obtained from EQCM-D of PTMA in 0.5 M $LiBF_4$ in propylene carbonate. a) Δm *vs*. scan rate, b) integrated charge transfer Q *vs*. scan rate for oxidation, c) Δm *vs*. scan rate$^{-1/2}$ with linear fit, and d) Q *vs*. scan rate$^{-1/2}$ with linear fit.

Figure 2-8 shows the differences in shear modulus between oxidation and reduced state of the PTMA electrode in the three electrolytes. In all cases, the shear modulus decreased upon oxidation, as seen by a negative value in delta shear modulus. For the varying salts the absolute change in shear modulus during oxidation followed the order of $LiCF_3SO_3$ > $LiBF_4$ > $LiClO_4$.

The varying trends of delta shear modulus with scan rate and salt are difficult to interpret, as they are a mixed result of complex and interrelated factors such as electrolyte concentration in the neutral PTMA film, solvent molecules dragged into or out of the film, competing contributions from lithium expulsion and anion uptake, and ion size.

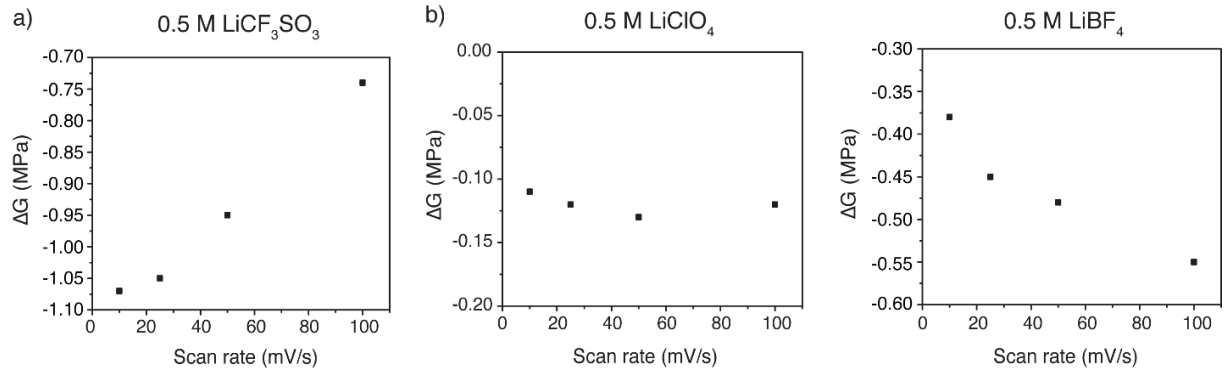

Figure 2-8. The difference in shear modulus between oxidized and reduced states of the PTMA electrode in a) 0.5 M $LiCF_3SO_3$, b) 0.5 M $LiClO_4$, and c) 0.5 M $LiBF_4$ in propylene carbonate.

2.5. The Doping Mechanism of PTMA

To gain further insight into the charge and mass transfer process, the mass change per electron charge transferred ($\Delta m/e$) was calculated as Δm/Q. Assuming each positive charge is doped by an anion in the bulk electrolyte, one mole of the oxoammonium cation requires one mole of counter-ions (for example, $CF_3SO_3^-$) to diffuse into the swollen PTMA cathode. Thus, the theoretical $\Delta m/e$ ratio is only dependent on the molecular weight of the anion, regardless of the scan rate. For the case of $LiCF_3SO_3$, the theoretical $\Delta m/e$ was calculated as below.

$$\frac{\Delta m}{e} = \frac{Mw(CF_3SO_3^-)}{Faraday\ const.} \times \frac{1000\ mg}{g}$$

$$= \frac{149.07\frac{g}{mol}}{96485\frac{C}{mol}} \times \frac{1000\ mg}{g} = 1.55\frac{mg}{C} \qquad \text{(Equation 2-1)}$$

Experimentally, Δm was calculated by first averaging the two mass plateaus at the reduced and oxidized state, and then taking the difference between the two averages. Charge transfer was integrated from current *vs*. time in cyclic voltammetry for each half cycle (i.e., oxidation or reduction). **Figure 2-9** shows a graphic illustration for the $\Delta m/e$ calculation.

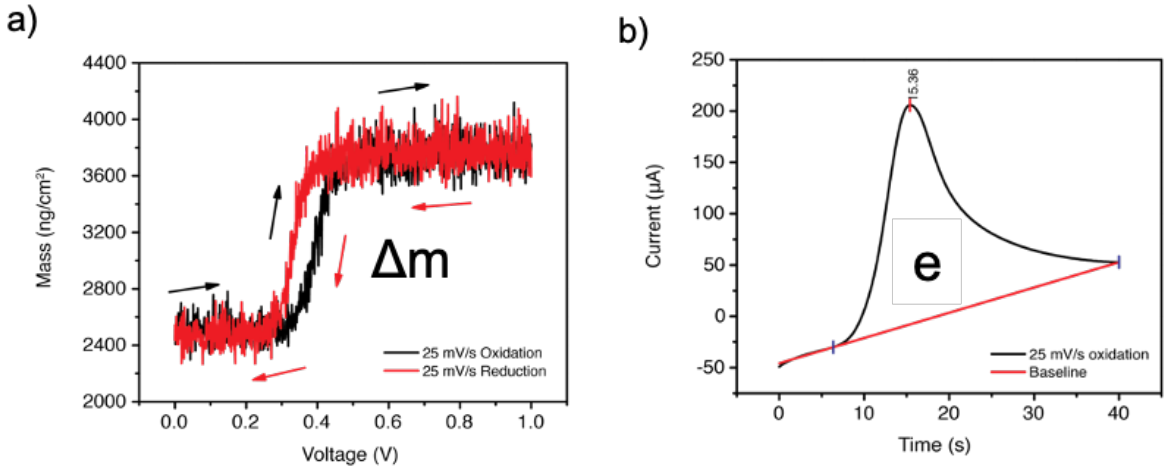

Figure 2-9. Graphic illustration of a) Δm between the oxidized and reduced state, and b) charge integration from current *vs*. time.

Figure 2-10a shows the experimental value of Δ*m/e* for 0.5 M $LiCF_3SO_3$, and the corresponding theoretical Δ*m/e* ratio is shown as the blue dashed line. Notably, a linear relationship between Δ*m/e* and $v^{1/2}$ is observed because of the dominating behavior of *Q,* which scales with $v^{-1/2}$. The experimental Δ*m/e* value was consistently lower than the theoretical value of 1.55 mg C^{-1} for $CF_3SO_3^-$. This indicates that the doping mechanism deviates from the previous assumption of doping by anion diffusion from the bulk electrolyte.

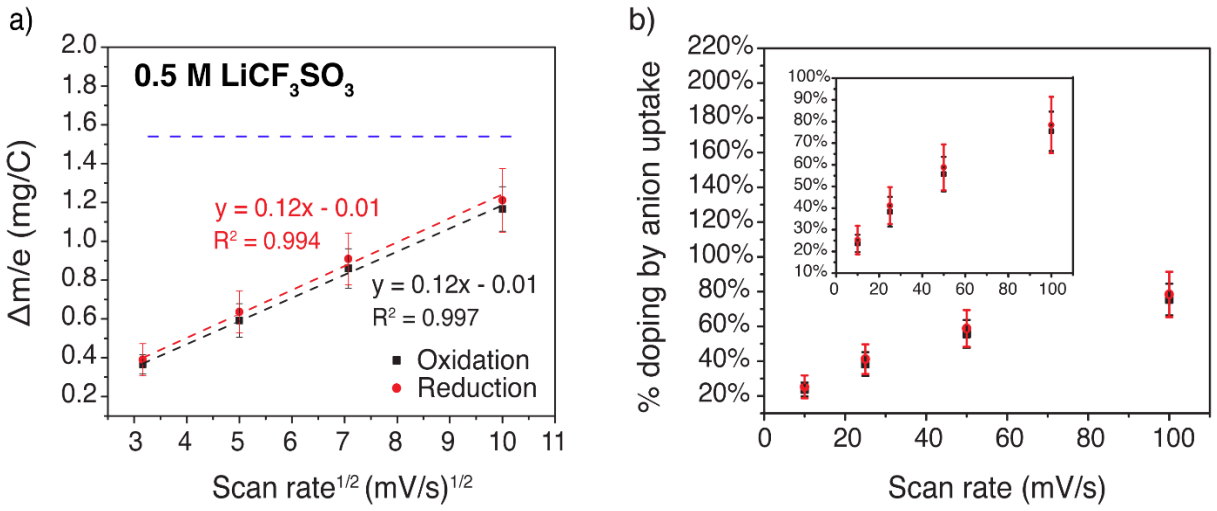

Figure 2-10. a) Δ*m/e* and b) percent doping by anion uptake for 0.5 M $LiCF_3SO_3$ in propylene carbonate with linear regression of Δ*m/e vs*. scan rate$^{1/2}$. The theoretical Δ*m/e* value is 1.55 mg C^{-1}, assuming one $CF_3SO_3^-$ anion transporting from the bulk solution. The error bars represent the average and standard deviations of at least three independent samples, using the second cycle at the respective scan rate from the sequence shown in Figure 2-1.

The lower experimental Δ*m/e* ratios might be due to inadequate mass transfer or excess charge transfer. Thus, we calculated a "theoretical" charge transfer simply by dividing the Δ*m* from EQCM-D with the theoretical Δ*m/e* ratio of 1.55 mg C^{-1} for the case of $LiCF_3SO_3$. **Table 2-2** summarizes the Δ*m/e* comparison of the "theoretical" charge (column 3) and the integrated charge (column 4) from cyclic voltammetry. Since the measured charge transfer is much greater than the "theoretical" charge transfer, there should exist additional electrochemical processes that consumes charge transfer while not causing significant mass change on the EQCM-D sensor. In other words, the most plausible explanation is that there is a mixture of doping mechanisms occurring within the PTMA electrode.[56]

Table 2-2. Comparison of charge transfer values.

Scan rate ($mV\ s^{-1}$)	Δm from EQCM-D (ng/cm2)	"Theoretical" charge transfer (μC)	Measured charge transfer (μC)	Percentage of doping by anion uptake
10	1411.3	1033.1	4514.9	22.9%
25	1330.8	974.2	2424.9	40.2%
50	1313.1	961.2	1601.2	60.0%
100	1195.4	875.0	1070.6	81.7%

We propose three doping processes in **Figure 2-11**: doping by lithium expulsion, doping by anion uptake I, and doping by anion uptake II. In the first case, PTMA that is swollen with electrolyte oxidizes by the doping of an anion internal to the film, resulting in the expulsion of a lithium cation into the bulk electrolyte (**Figure 2-11a**). By this process, the electrode mass will

decrease as $\Delta m/e$ = -0.072 mg C^{-1}. In contrast, a second process of exchanging an anion with the external electrolyte may occur, yielding $\Delta m/e$ = +1.55 mg C^{-1} when the anion is $CF_3SO_3^-$ (**Figure 2-11b**). In a third process, PTMA oxidation occurs by internal doping from an anion, which is balanced by the uptake of anion from the external electrolyte (**Figure 2-11c**). Because we are not able to distinguish between anion uptake I and II using EQCM-D, we treat them as a combined process separate from lithium expulsion (see below).

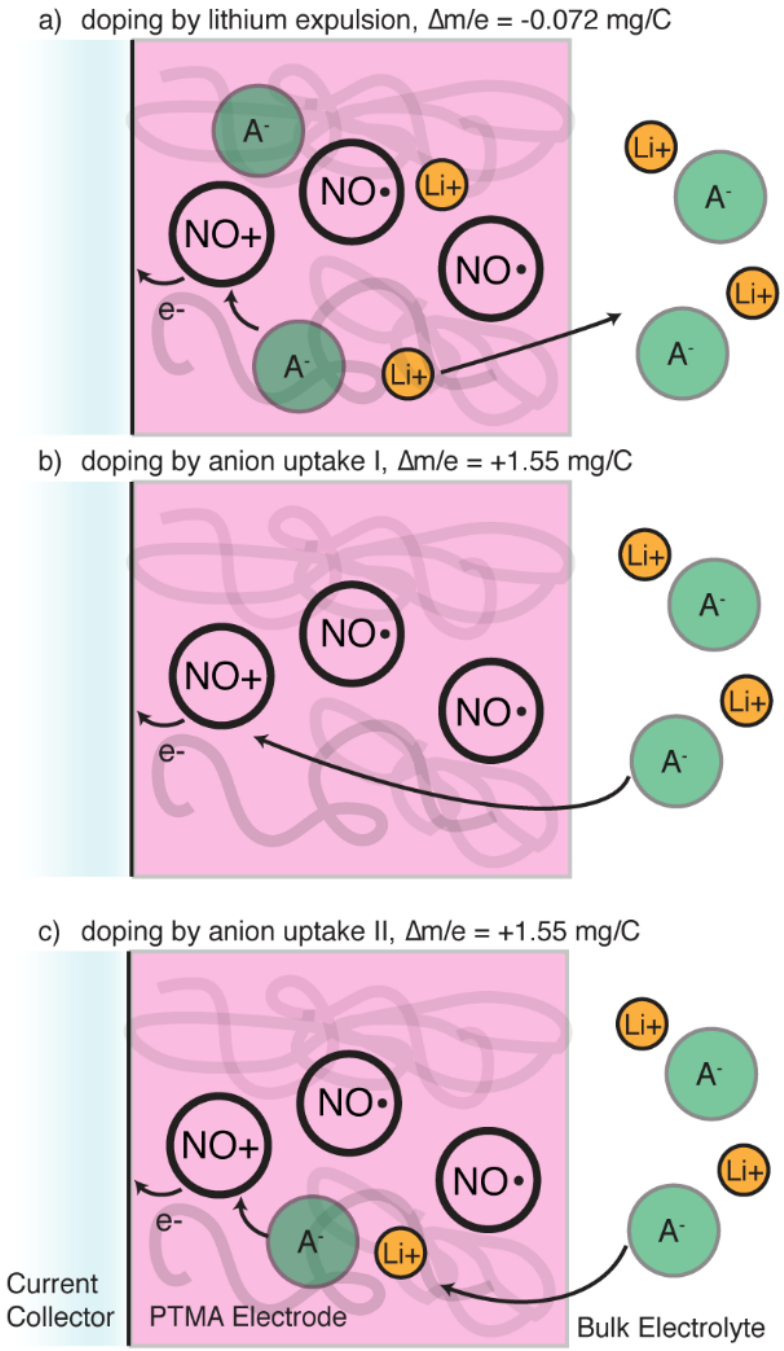

Figure 2-11. Three modes of anionic doping in a swollen PTMA electrode. a) Doping by lithium expulsion, in which an anion (A^-) already imbibed into the polymer dopes PTMA, expelling a lithium cation. b) Doping by anion uptake I, in which an anion from the bulk electrolyte dopes PTMA. c) Doping by anion uptake II, in which an anion imbibed in the polymer dopes PTMA, and an anion from the bulk electrolyte balances the imbibed lithium cation. $\Delta m/e$ values are given for the case of when $A^- = CF_3SO_3^-$. NO• represents PTMA in the neutral organic radical state and NO^+ represents the oxidized form of PTMA.

The percentage of doping by anion uptake was determined simply by dividing the "theoretical" charge transfer with the measured overall charge transfer (column 5 in **Table 2-2 and Figure 2-10b**), because the "theoretical" charge transfer was calculated by assuming anion uptake is the only doping process. As scan rate increases, the Δ*m/e* ratios and percentages of doping by anion uptake also increased. This generally indicates that doping by lithium expulsion dominates at low scan rates and doping by anion uptake increases at higher scan rates. The concept of doping by lithium expulsion and anion uptake in organic radical polymers is consistent with the recent qualitative findings from Tokue et al. for copolymer containing the TEMPO radical and charge neutralization anion trifluoromethanesulfonylimide ($TFSI^-$).[56] Cyclic voltammetry of this copolymer showed two peaks, which were attributed separately to lithium expulsion and anion uptake. Here, we also observed two peaks in our cyclic voltammograms, **Figure 2-2**. The peak at the lower potential is assigned to internal doping by lithium expulsion, and the higher potential peak is assigned to doping by anion uptake. These peaks were more pronounced in the reduction scan relative to the oxidation scan, where similar behavior has been observed for conjugated polymers that vary in conductivity as a function of potential.[57, 58]

2.6. Effect of Electrolyte Concentration on Doping

To demonstrate the manipulation of lithium expulsion *vs*. anion uptake, EQCM-D of PTMA at a lower electrolyte concentration (0.01 M $LiCF_3SO_3$ in propylene carbonate) was performed, **Figure 2-12**. At this low concentration, fewer ions are absorbed into the PTMA thin film so doping by lithium expulsion should be diminished. **Figure 2-12a** shows pronounced peak splitting in the reduction wave at 10 mV s^{-1}. As scan rate increased, the low-potential peak attributed to lithium expulsion diminished relative to the high-potential peak attributed to anion

uptake. In comparison, **Figure 2-2** shows a stronger contribution from the lower potential peak associated with lithium expulsion for 0.5 M $LiCF_3SO_3$, thus confirming the effect of electrolyte concentration on the doping process.

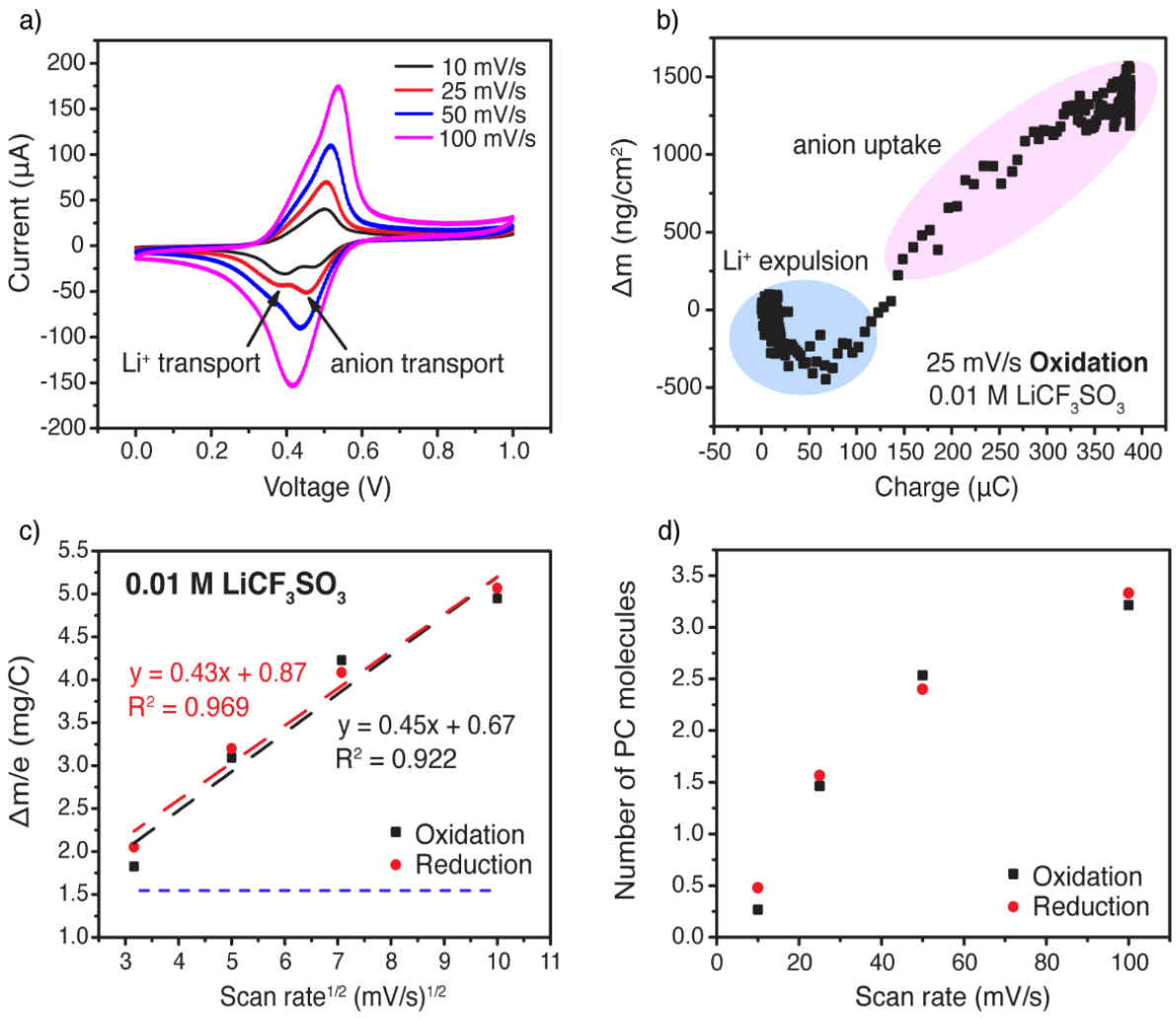

Figure 2-12. Anionic doping in low-concentration electrolyte. a) Cyclic voltammetry of PTMA at the low electrolyte concentration of 0.01 M $LiCF_3SO_3$ in propylene carbonate, showing peaks attributed to lithium expulsion and anion uptake b) Change in electrode mass *vs*. charge passed during PTMA oxidation at 25 mV s^{-1} via EQCM-D. The blue region highlights doping by lithium expulsion and the pink region highlights doping by anion uptake. c) Δ*m/e* ratios of PTMA at different scan rates. d) The number of propylene carbonate molecules being transported with the anion, in this case $CF_3SO_3^-$. The data shown here are attributed to a sample following the sequence shown in Figure 2-2, with data taken from the second cycle at the respective scan rate.

This then raises the question of whether the doping mechanisms occurs simultaneously or sequentially. To examine this, the mass change during the oxidation of PTMA in 0.01 M $LiCF_3SO_3$ at 25 mV s^{-1} was plotted against the electronic charge exchanged, calculated from the integrated cyclic voltammetry current (**Figure 2-12b**). At the beginning of the oxidation process, the electrode mass change became negative, corresponding to Li^+ ion expulsion and internal doping. Further into the oxidation process, the electrode mass change became positive, consistent with doping by anion uptake. These observations suggest that doping occurs first by lithium expulsion and second by anion uptake in partially overlapping processes.

Interestingly, $\Delta m/e$ for PTMA in 0.01 M $LiCF_3SO_3$ in propylene carbonate was consistently greater than the theoretical $\Delta m/e$ value of 1.55 mg C^{-1} (**Figure 2-12c**). The extra mass arises from the anion dragging associated solvent molecules into the electrode during the external doping process. This is quantified by a mass balance (Equation 2-2) assuming purely external doping and by treating the remaining mass differences as propylene carbonate molecules.[37] As the scan rate increased, the number of propylene carbonate molecules per anion increased as well, ranging from 0.27 at 10 mV s^{-1} to 3.22 at 100 mV s^{-1} in oxidation (**Figure 2-12d**).

$$\frac{\Delta mF}{e} - Mw_{anion} = \#\ PC\ molecules\ \times\ Mw_{PC} \qquad \text{(Equation 2-2)}$$

where F is the Faraday constant, Mw_{anion} and Mw_{PC} are the molecular weight of anion (in this case $CF_3SO_3^-$) and propylene carbonate, respectively.

It is curious that so much propylene carbonate would transfer into the electrode upon oxidation for 0.01 M $LiCF_3SO_3$, but not for 0.5 M $LiCF_3SO_3$. The explanation is related to whether or not $LiCF_3SO_3$ exists in solvent-separated or contact ion pairs in the external

electrolyte. $LiCF_3SO_3$ mostly exists in contact ion pairs and aggregated states for a concentration of 0.5 M.[59, 60] At sufficiently low concentrations (21.3:1 PC to $LiCF_3SO_3$) solvent-separated ion pairs form, as is the case for 0.01 M $LiCF_3SO_3$ (1175:1 PC to $LiCF_3SO_3$). At 0.01 M, there is not enough time for $CF_3SO_3^-$ to shed its surrounding solvent shell, causing the number of propylene molecules imbibed into the electrode to increase (**Figure 2-12d**). At 0.5 M, the majority of $LiCF_3SO_3$ exists in contact ion pairs, and transport effects from propylene carbonate are minor (**Figure 2-10b**).

2.7. Relative Dominance of Lithium Expulsion *vs*. Anion Uptake

The relative dominance of lithium expulsion over anion uptake at lower scan rates can be attributed to a number of competing phenomena including electrolyte dissociation in the film *vs*. the bulk, mobility of the anion, kinetics of the redox reaction front, and local availability of anions within the PTMA electrode.

At lower scan rates, locally available (internal) ions have more time to dissociate, and we believe that doping by lithium expulsion is favorable. This is supported by the fact that this process occurs at a less positive potential and by the following ideas. At a lower scan rate, the effect of ion dissociation is more pronounced, because 1) the imbibed anions are locally available to $PTMA^+$ because the diffusion distance to the cation site is shorter than diffusing from the bulk electrolyte, and 2) the A^- has to dissociate from Li^+ in order to dope the $PTMA^+$. There is sufficient time for electrolyte dissociation within PTMA and doping by lithium expulsion can proceed.

However, the lithium expulsion process is not kinetically favored, which is why it loses prominence at higher scan rate. The extent of $[Li^+A^-]$ dissociation is related to the dielectric

constant of the media. Propylene carbonate, which is our bulk electrolyte, has a high dielectric constant (64.92 at 25 °C), which means that propylene carbonate can easily dissolve a wide variety of lithium salts.[61, 62] However, PTMA has a much lower dielectric constant (3.4 at 25 °C).[63] This means that the lithium salt experiences two very different dielectric media such that $[Li^+A^-]$ is less likely to dissociate in PTMA than in the bulk electrolyte. This can offset the favorability attained by being spatially close to the PTMA site such that internal $[Li^+A^-]$ does not have enough time to dissociate and participate in the doping mechanism at high scan rate.

At higher scan rate, a sharper concentration gradient may arise. As a result, the ion diffusion process may become facilitated at higher scan rate (i.e., the second peak in cyclic voltammetry). With all of these added effects (greater driving force, facilitated ion dissociation in the electrolyte, slow dissociation of locally imbibed ions), the lithium expulsion mechanism is no longer favorable under short experimental timescales. Thus, doping by anion uptake dominates at higher scan rates.

The relative speed and spatial location of the redox reaction front is also a competing factor, in which the front will initiate from the PTMA|current-collector interface.[45, 46] Internal doping and lithium expulsion may be favored in this case because the internal anions are proximally close. As scan rate increases, the speed of the redox reaction front accelerates and approaches the PTMA|bulk electrolyte interface more quickly, allowing external anion doping to increase. At higher scan rates, the resulting polarization in the film may present a larger driving force for external anion doping as well. Further work is needed to resolve the relative contributions of these factors.

2.8. Effect of Anions on Doping

To understand how various anions affect the mass and charge transfer process in PTMA, two other electrolytes were investigated: $LiClO_4$ and $LiBF_4$ at 0.5 M in propylene carbonate. The comparison of $LiClO_4$ and $LiBF_4$ with $LiCF_3SO_3$ is shown in **Figure 2-13**. $LiClO_4$ electrolyte yields $\Delta m/e$ values that are mostly below theoretical, whereas $LiBF_4$ electrolyte $\Delta m/e$ values are mostly greater. These differences may be attributed to variations in ion mobility, dissociation constant of each salt, and solvent participation. From highest to lowest, the mobilities are ranked as $LiBF_4 > LiClO_4 > LiCF_3SO_3$, and the dissociation constants are ranked as $LiClO_4 > LiBF_4 > LiCF_3SO_3$.[64, 65] The high mobility of BF_4^- indicates that it diffuses at a faster rate in the electrolyte than the other two anions. In constrast, $LiCF_3SO_3$ commonly exists in contact ion pairs in the electrolyte[60, 61, 65], so it is more difficult to extract $CF_3SO_3^-$ anions from the electrolyte. $LiClO_4$, with its largest dissociation constant but relatively low ion mobility, shows moderate behavior.

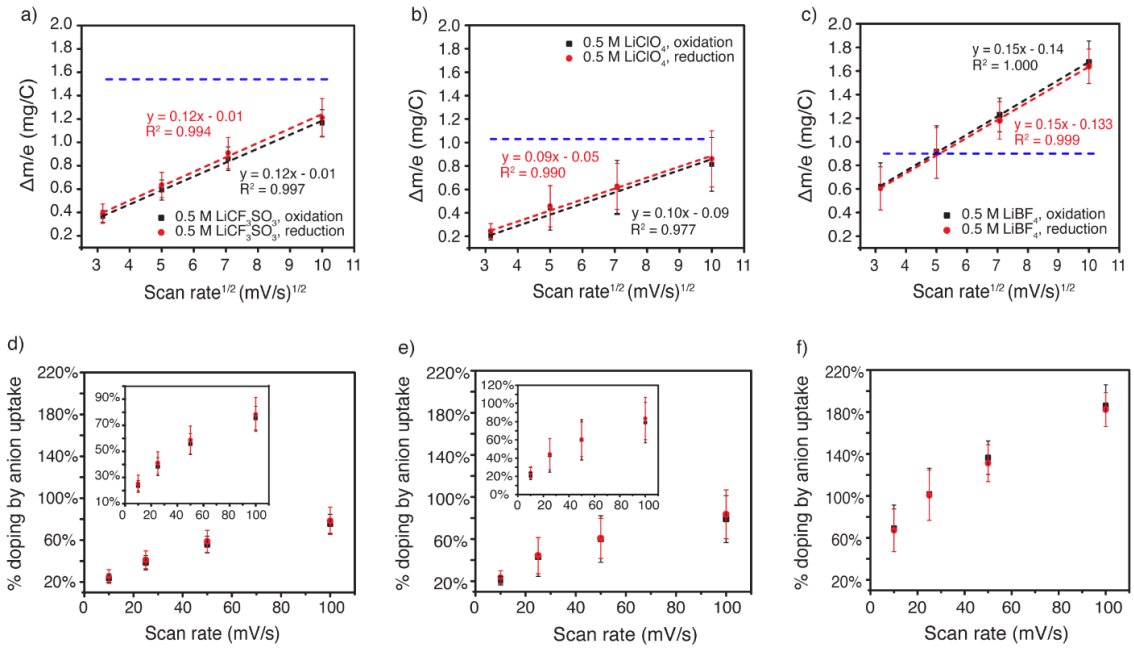

Figure 2-13. Δ*m/e* and doping for various electrolytes. a-c), Comparison of experimental and theoretical Δ*m/e* ratios for 0.5 M a) $LiCF_3SO_3$, b) $LiClO_4$ and c) $LiBF_4$ in propylene carbonate with linear regression of Δ*m/e vs.* (scan rate)$^{1/2}$. The theoretical Δ*m/e* values (blue dashed line) for $LiCF_3SO_3$, $LiClO_4$ and $LiBF_4$ are 1.55, 1.03 and 0.90 mg C^{-1}, respectively, assuming one anion is transported from the bulk solution. d-f), Percentage doping by anion uptake for d) $LiCF_3SO_3$, e) $LiClO_4$ and f) $LiBF_4$. The error bars represent the average and standard deviations of at least three independent samples, using the second cycles at the respective scan rate from the sequence shown in Figure 2-2.

2.9. Conclusion

In conclusion, the contributions of ion doping to the redox mechanism of PTMA have been quantified to reveal a dual doping process for the first time. The dual doping mechanism and this EQCM-D methodology could apply to other non-conjugated redox-active polymer for which electrolyte plays a significant role, such as electrochromics, sensors, and energy storage. For further consideration, the extent of the lithium expulsion and anion uptake doping contributions should depend on the electrolyte and solvent choice, the affinity of the electrolyte

and solvent to the polymer, the mechanical properties of the polymer, and the orientation of the polymer.[50, 66-69] These results provide insight into how organic radical polymers operate and key features for their future design. It is desirable to have some degree of lithium expulsion, as it allows the reaction to occur at a lower potential, and probably facilitates the rapid redox PTMA reaction. However, lithium expulsion requires the uptake of electrolyte solution, and risks dissolution of the polymer, so this feature should be balanced carefully. This finding also indicates that the electrolyte should be chosen wisely so as to avoid solvent transport, which could possibly cause volumetric changes in the electrode and lower the response time (which is important for electrochromics and sensors). This points to using more concentrated electrolytes or anions that are less likely to interact strongly with the solvent. Finally, an intriguing feature is that Q scales with $v^{-1/2}$ and that the reaction is limited by electron diffusion, thus adding further interpretation of the conduction mechanism for organic radical polymers.[13, 31, 45, 46, 48-50, 70]

3. THERMALLY CROSSLINKABLE ORGANIC RADICAL POLYMER*

3.1. Introduction

A major challenge for PTMA cathodes is that capacity fade occurs because of its gradual dissolution during long-term cycling. PTMA can be synthesized either from free radical[10, 20] or controlled radical polymerization.[13, 71] In general, free radical polymerization yields PTMA with higher molecular weights (up to 89,000 g mol^{-1})[10] but also a wider molecular weight distribution.[32] A high dispersity is undesirable because low-molecular-weight polymer chains dispersed within the electrode gradually dissolve into the electrolyte.[32] In contrast, controlled radical polymerization usually yields PTMA with a low dispersity ($Đ < 1.2$), but it is exceedingly difficult to achieve high molecular weights (> 24,000 g/mol) because of reversible chain transfer.[13, 51, 71] Single electron transfer-living radical polymerization can yield even higher PTMA molecular weights of 169,000 g/mol,[72, 73] but capacity fade is still an issue.

Two main strategies to address dissolution of the active radical polymer include using a block copolymer motif in which one block is non-dissolving (but electrochemically inactive) and adding crosslinkable groups to form a non-dissolving electroactive network. Utilizing the former strategy, Hauffman et al. used atom transfer radical polymerization (ATRP) to synthesize PTMA-b-poly(styrene) (PTMA-b-PS) block copolymer, which did not dissolve in the electrolyte.[71] As for the latter strategy, ethylene glycol dimethacrylate (EGDMA) was

* Modified and reprinted with permission from Wiley. https://doi.org/10.1002/cssc.201903554 "Solution-processable thermally crosslinked organic radical polymer battery cathodes" by Shaoyang Wang, Albert Min Gyu Park, Paraskevi Flouda, Alexandra D. Easley, Fei Li, Ting Ma, Gregory D. Fuchs, and Jodie L. Lutkenhaus, *ChemSusChem*, 2020, 13, 2371 – 2378, Copyright 2020, Wiley-VCH Verlag GmbH & Co.

polymerized with 2,2,6,6-tetramethylpiperidin-4-yl methacrylate (TMPM, a precursor monomer of PTMA) to obtain crosslinked PTMA.[15, 17, 19] Vlad et al. demonstrated solvent-free melt-polymerization of TMPM and EGDMA with dispersed carbon black nanoparticles in the reaction mixture.[19] Iwasa et al. modified the free radical polymerization of PTMA by directly including EGDMA in the solvent mixture, resulting in an electrolyte-swollen PTMA gel.[15] Elsewhere, Bugnon et al. added EGDMA into a radical bearing monomer, 4-methacryloyloxy-2,2,6,6-tetramethylpiperidine-N-oxyl, and obtained crosslinked PTMA via group-transfer polymerization.[17] In all above-mentioned studies, cathodes made from crosslinked PTMA showed better cycling stability than the non-crosslinked cells because PTMA dissolution was suppressed.[15, 17, 19] However, PTMA crosslinked with EGDMA is insoluble in organic solvents, which prohibits solution-processing to directly obtain battery electrodes with conductive carbon additives.[14] Although this initially appears to be a minor detail, it prevents the materials from being manufactured into electrodes by an approach that is compatible with currently used methodologies for today's transition metal oxides. Therefore, the current status of crosslinkable PTMA presents a barrier to scalability for organic battery manufacturing.

Thus, researchers have also investigated post-crosslinking methods after solution processing of the polymer electrodes.[14, 74-76] Suga et al. photo-crosslinked TEMPO-substituted polynorbornene by using a bis(azide) derivative.[14] TEMPO-substituted polynorbornene, photo-crosslinker, and carbon nanofibers were mixed in a toluene-ethyl acetate solution and molded into electrodes prior to UV exposure.[14] The resulting crosslinked cathode showed a high capacity (106 mAh g^{-1} *vs.* theoretical capacity of 109 mAh g^{-1}), and stable cycling stability (up to 1000 cycles).[14] Most recently, Zheng et al. introduced photo-crosslinkable benzophenone moieties into PTMA by copolymerizing TMPM and benzoylphenyl methacrylate.[74] Besides photo-

crosslinking, Ibe et al. developed another crosslinking method – thermal curing of TEMPO-bearing acetoacetate (TEMPO-AcAc) and acryloyl derivatives via Michael polyaddition on glassy carbon substrates.[75] Janoschka et al. used a multifunctional epoxide to crosslink reversible addition-fragmentation chain transfer (RAFT)-polymerized linear PTMA. A slurry made from PTMA, an epoxide crosslinker, and carbon nano-powder was deposited on graphite foil by inkjet printing to form an electrode.[76] Upon heating at 130 °C, the epoxide crosslinker reacted with residual amines in PTMA and crosslinked the electrode.[76]

These post-crosslinking methods facilitate solution processing, but still have major drawbacks. The thickness of the photo-crosslinked polynorbornene polymer electrode was limited to only the micron-scale due to diffusion-controlled charge transfer limitations in thicker films.[14, 75] Moreover, photo-crosslinking might not be effective because carbon additives strongly absorb light.[76] Although the earlier crosslinking study using Michael addition improved the polymer film thickness to 10 μm, the electrode capacity was rather low (around 55 mAh g^{-1}).[75] Similar low capacity was observed with an inkjet-printed PTMA composite cathode (around 50 mAh g^{-1}).[76] Therefore, the main challenges are to create crosslinked PTMA electrodes that do not dissolve, are relatively thick to achieve a high active material loading, are compatible with carbon additives, and have a high capacity.

Here, we demonstrate a simple post-synthetic method to crosslink thick (15-25 μm) PTMA cathodes with high capacity and cycling stability. Epoxy curing is widely used to create crosslinked networks by the inclusion of a curing agent to promote epoxide ring-opening.[77] We introduced epoxide groups into PTMA through free radical polymerization of TMPM and glycidyl methacrylate (GMA). Glycidyl methacrylate has been previously employed to graft TEMPO containing block copolymers onto indium tin oxide (ITO) substrate.[78] Herein, by

controlling the reaction temperature, we produced a linear PTMPM-*co*-GMA polymer and oxidized it to PTMA-*co*-GMA using *meta*-chloroperbenzoic acid (mCPBA). The as-synthesized PTMA-*co*-GMA dissolves in common organic solvents and allows solution processing such as spin-coating, drop-casting, and doctor-blading. Epoxy curing was initiated under elevated heat or UV-irradiation to obtain crosslinked PTMA, thus preventing dissolution of the active material during cycling. The effect of photo-crosslinking and thermal curing on radical content was evaluated by using solid-state electron paramagnetic resonance (EPR) spectroscopy. Furthermore, crosslinked PTMA-*co*-GMA in the organic electrolyte solvent was evaluated using a electrochemical quartz crystal microbalance with dissipation monitoring (EQCM-D) to assess the swelling, dissolution, and stability. Finally, a two-electrode coin cell was assembled to evaluate the electrochemical properties of the crosslinked PTMA-*co*-GMA. Our results show that thermal crosslinking preserved the active radical concentration whereas photo-crosslinking proved detrimental to the radical concentration. This new strategy for crosslinking PTMA allows for the solution processing of thick electrodes with carbon that will enable the manufacturing of organic radical batteries that are resistant to capacity fade by using cathode materials alternative to transitional-metal oxides.

3.2. Materials and Methods

3.2.1. Materials

The monomer for PTMA synthesis, 2,2,6,6-tetramethyl-4-piperidinyl methacrylate (TMPM) was purchased from Tokyo Chemical Industry. Vapor grown carbon fiber (VGCF) was purchased from Showa Denko K.K. Polyvinylidene fluoride (PVDF) binder was purchased from MTI corporation. All other chemicals were used as received from Sigma-Aldrich unless

otherwise noted. 2,2'-Azobis(2-methylpropionitrile) (AIBN) was recrystallized by using methanol at reduced temperature and vacuum dried overnight at room temperature.

3.2.2. Synthesis and Characterization

The PTMA-*co*-GMA copolymer synthesis was modified from a free radical polymerization of PTMA homopolymer reported elsewhere.[10] GMA was added as the crosslinker to a reaction mixture containing TMPM (22 mmol, 5 g), toluene (10 ml) and AIBN (0.67 mmol, 0.109 g). The free radical polymerization was initiated by AIBN at 60 ºC and lasted for 48 h. The yield was approximately 85%. The copolymer products were collected and oxidized to nitroxide radicals using 2 equiv. of mCPBA for 3 h. The yield was approximately 50%. To obtain copolymers with various crosslinking densities, three batches of copolymers were synthesized by adding 1 mol% (0.22 mmol, 29 μL), 3 mol% (0.44 mmol, 58 μL), and 5 mol% (0.66 mmol, 87 μL) of GMA in the feed, denoted as PTMA-*co*-GMA-1, PTMA-*co*-GMA-3, and PTMA-*co*-GMA-5, respectively.

The ^{1}H-NMR spectra for the three copolymers were collected by using an automated Bruker 400 MHz system using d-chloroform as the solvent. Size exclusion chromatography (SEC) was performed on a TOSOH EcoSEC (HLC-8320GPC) chromatogram to determine the molecular weight and dispersity ($Đ$) for the copolymers. The glass transition temperatures were measured using differential scanning calorimetry (DSC) at a scanning rate of 10 °C/min (Q200, TA instruments).

3.2.3. Crosslinking

A stock solution of copolymer (10 mg) dissolved in chloroform (1 ml) was prepared. For photo-crosslinking, the photoinitiator (10 μl, triarylsulfonium hexafluorophosphate salt, 50% in propylene carbonate) was added to the chloroform solution. A thin layer of PTMA-*co*-GMA was

deposited onto indium ITO-coated glass (Delta Technologies) either by spin-coating or drop-casting the PTMA-*co*-GMA chloroform solution. The coated substrate was placed an inch away from a short-wave UV lamp (254 nm) and the UV exposure lasted for 30 min. Subsequently, the sample was vacuum dried overnight at 50 ºC to remove any remaining solvents. For thermal curing, the PTMA-*co*-GMA-coated ITO-coated glass was heated at 175 ºC in a vacuum oven for 3 h. To characterize the thermal curing mechanism, Fourier transform infrared spectroscopy (FTIR, Nicolet 6700 series, ThermoElectron) was conducted before and after thermal crosslinking on the copolymer casted ITO samples.

3.2.4. Spin Characterization

The spin concentration was measured using a Bruker X-band EPR spectrometer at room temperature. Solution-state measurements were conducted on 1 mM PTMA-*co*-GMA in chloroform using 1 mM 2,2,6,6-tetramethyl-1-piperidinyloxy (TEMPO) in chloroform as the reference. The error bars were obtained from three parallel EPR measurements using the same stock solution for a particular copolymer. Solid-state measurements were conducted on copolymer-coated ITO substrates.

3.2.5. EQCM-D Measurements

Gold-coated, planar AT-cut quartz crystals (QSX 338) with a fundamental frequency of 4.95 MHz were used as substrates for EQCM-D (Biolin Scientific). Fresh EQCM-D sensors were rinsed with MilliQ water, dried with high velocity N_2, and plasma-treated for 5 min before mounting in the EQCM-D. A baseline for the bare crystal was recorded first in static air and second in 1:1 (*v/v*) ethylene carbonate (EC)/diethyl carbonate (DEC). A stock solution of 10 mg PTMA-*co*-GMA in 1 ml chloroform was made. A thin layer of PTMA-*co*-GMA was spin-coated onto the substrate by adding 40 µL of the stock solution at 1000 rpm. The coated EQCM-D

sensor was thermally cured in a vacuum oven at 175 °C for 3 hours. After cooling to room temperature, the PTMA-*co*-GMA coated sensor was mounted into the EQCM-D. The coated sensor was allowed to equilibrate first until the frequency drift was below 1 Hz per hour.[79] Then a new baseline was taken for the dry film in the air. To measure the swelling ratio, EC/DEC (1/1 *v/v*) was pumped into the EQCM-D chamber at 150 μL min^{-1} for 5 minutes. The film was allowed to further equilibrate in static organic solvent for 24 hours, and afterwards another baseline was taken for the swelled copolymer film. The bare sensor baseline and dry film baseline were stitched in QSoft and fitted in QTools (Biolin Scientific) using the Sauerbrey model. This provides the mass or the thickness of the dry film. Then the baseline for the swelled film was stitched to the bare sensor baseline under organic electrolyte. The swelled film thickness was analyzed by using the viscoelastic model (or the Voigt model). In the viscoelasic model, three parameters (fluid density, fluid viscosity, and layer density) were specified and kept fixed throughout. The density and viscosity of EC/DEC (1:1 *v/v*) have been reported in previous literature; the values are 1160 kg m^{-3} and 0.00164 kg $m^{-1}s^{-1}$, respectively.[80] The density of the polymer-solvent interacting layer (L1) was approximated to have the same density as the EC/DEC solvent, 1160 kg m^{-3}. For each sample, at least two overtones out of the third, fifth, seventh and ninth overtones were included in the modeling to obtain reliable results. Fitting was conducted so as to provide a minimum χ^2, while reflecting characteristic trends in the raw data.

The EQCM-D response of the copolymer films during cyclic voltammetry was recorded after measuring the swelling ratio. The electrolyte was 0.5 M lithium triflate ($LiCF_3SO_3$) in EC/DEC (1:1 *v/v*). After evacuating the EC/DEC (1:1 *v/v*) solvent, the electrolyte was introduced into the EQCM-D chamber at 150 μL min^{-1} for 10 minutes. Then flow was stopped, and the copolymer coating was left in static electrolyte for equilibrium. The film was conditioned at 10

mV s^{-1} for 10 cycles, followed by cyclic voltammetry at 0.5, 1, 2, 5, 10, 25, 50, 75, and 100 mV s^{-1}, 3 cycles at each scan rate using a Gamry Interface 1000.

3.2.6. Cell Test

Coin cells (CR2032, MTI Cooperation) were assembled under an inert atmosphere. A slurry of PTMA-co-GMA/vapor grown carbon fiber (VGCF)/PVDF (3:6:1 *w/w/w*) was made in 1-methyl-2-pyrrolidinone (NMP, anhydrous, 99.5%). The slurry was cast onto aluminum foil using doctor-blading and dried in a vacuum oven at 60 ºC overnight. Cathodes of a diameter of 12 mm were cut. The anode was lithium foil with a diameter of 14 mm. The electrolyte was 1 M lithium hexafluorophosphate ($LiPF_6$) solution in EC/DEC (1:1 *v/v*, battery grade. Two layers of separator (Celgard 2400) were inserted between the cathode and the anode.

All electrochemical testing was performed using an Arbin battery tester. Charge-discharge was measured at 0.1, 0.2, 0.5, 1, 2, 5, and 10 C between 3 and 4 volts. Cycling was conducted at 1 C for 50 cycles.

3.3. Characterization of Synthesis and Crosslinking

GMA was selected as the crosslinker for two reasons: 1) the epoxy group forms a network structure through thermal curing or photo-crosslinking, and 2) the crosslinker and the TMPM monomer share a common methacrylate unit, enabling free radical polymerization to produce a random copolymer (**Figure 3-1**). We varied the amount of GMA to assess the minimum amount of crosslinker needed to fully crosslink the electrode while still presenting the highest stable capacity. The reaction mixture after polymerization was a clear viscous liquid and became more viscous with increased GMA content. After precipitation and drying, the

copolymer remained soluble in common organic solvents. ^{1}H NMR spectroscopy confirmed the successful incorporation of GMA into PTMPM-*co*-GMA copolymers (**Figure 3-2 to 3-4**).

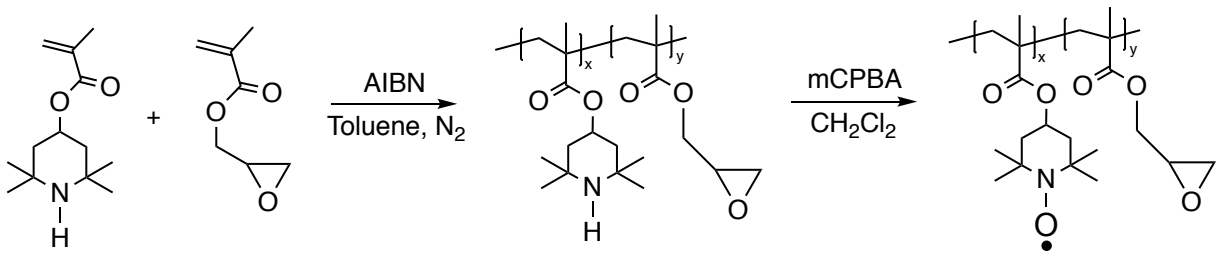

Figure 3-1. Synthesis of PTMA-*co*-GMA.

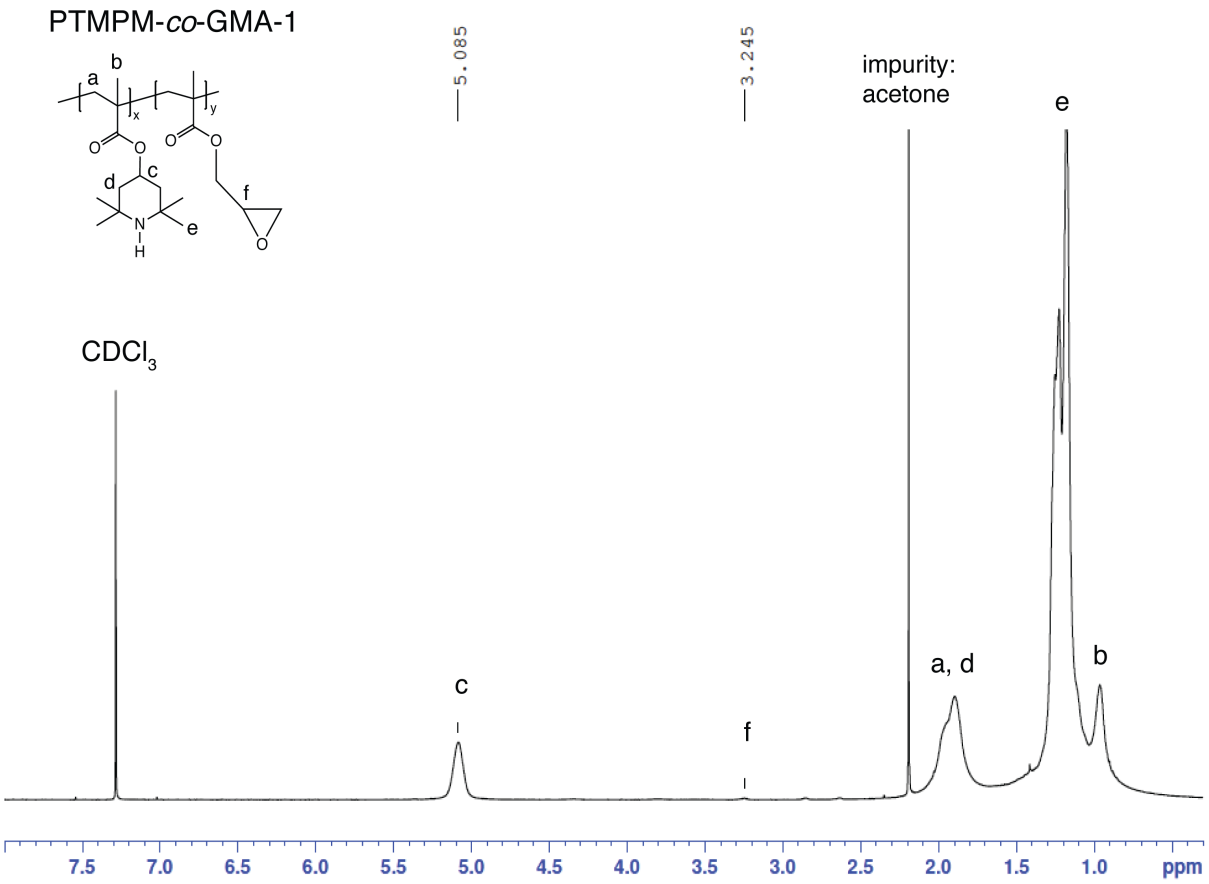

Figure 3-2. ^{1}H-NMR spectra of PTMPM-*co*-GMA-1.

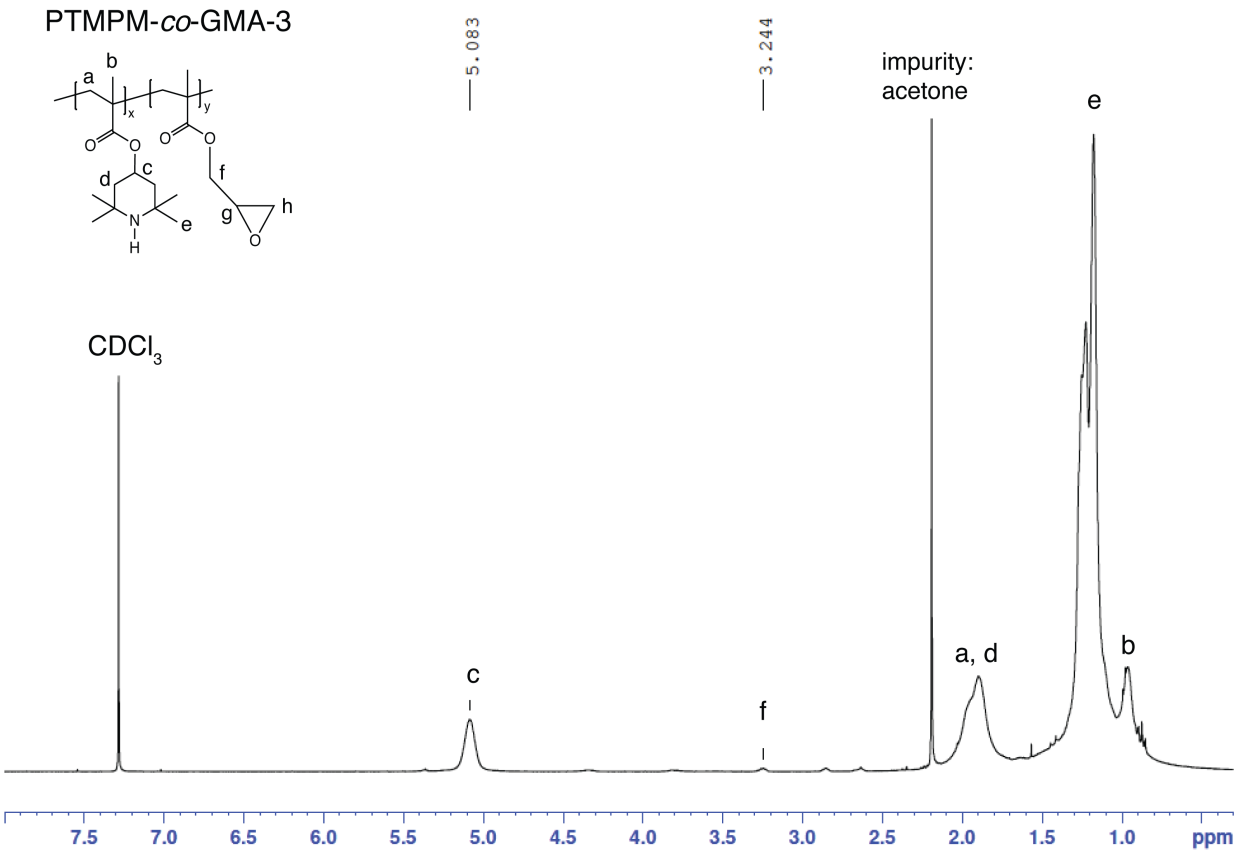

Figure 3-3. ^{1}H-NMR spectra of PTMPM-*co*-GMA-3.

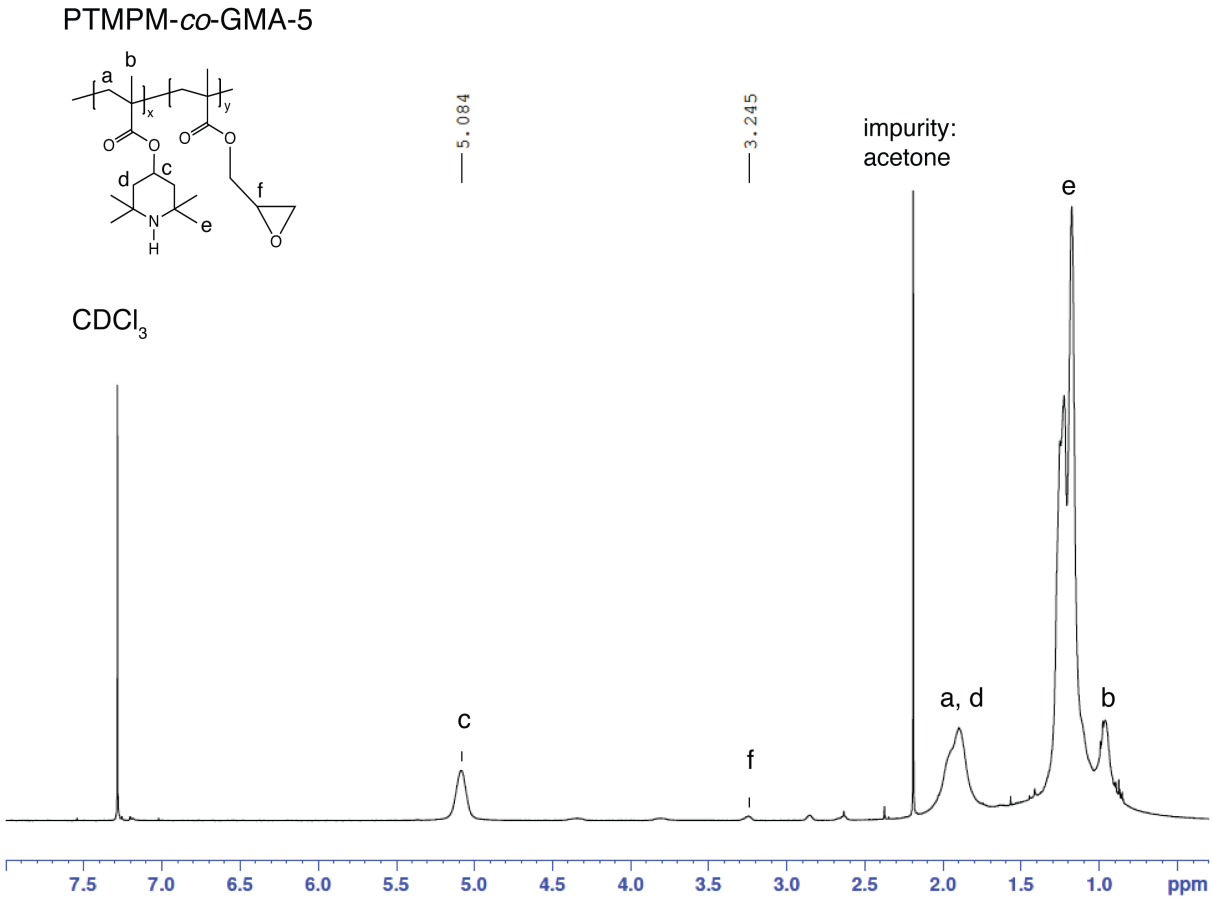

Figure 3-4. ^{1}H-NMR spectra of PTMPM-*co*-GMA-5.

As previously reported in the literature, oxidation with mCPBA never proceeds to completion and usually generates polymers with 65–81% radical content.[17] The radical concentrations in the PTMA-*co*-GMA copolymers were measured using solution-state EPR spectroscopy (**Table 3-1**, **Figure 3-5**). The copolymers all show broad peaks due to spin-spin interactions, indicating a high local concentration of nitroxide radicals along the polymer chain.[81] As the GMA content increased, the radical content decreased. The highest radical content was approximately 80 % for PTMA-*co*-GMA-1.

Table 3-1. Radical concentration of PTMA-*co*-GMA copolymers as determined using solution-state and solid-state EPR spectroscopy.

Copolymers	Solution-state (un-crosslinked)	Solid-state	
		Photo-crosslinked	Thermally cured
PTMA-*co*-GMA-1	80.3 ± 1.2%	~ 16.1%	~62.6%
PTMA-*co*-GMA-3	76.5 ± 9.9%	~9.9%	~55.1%
PTMA-*co*-GMA-5	66.3 ± 8.8%	~7.3%	~49.1%

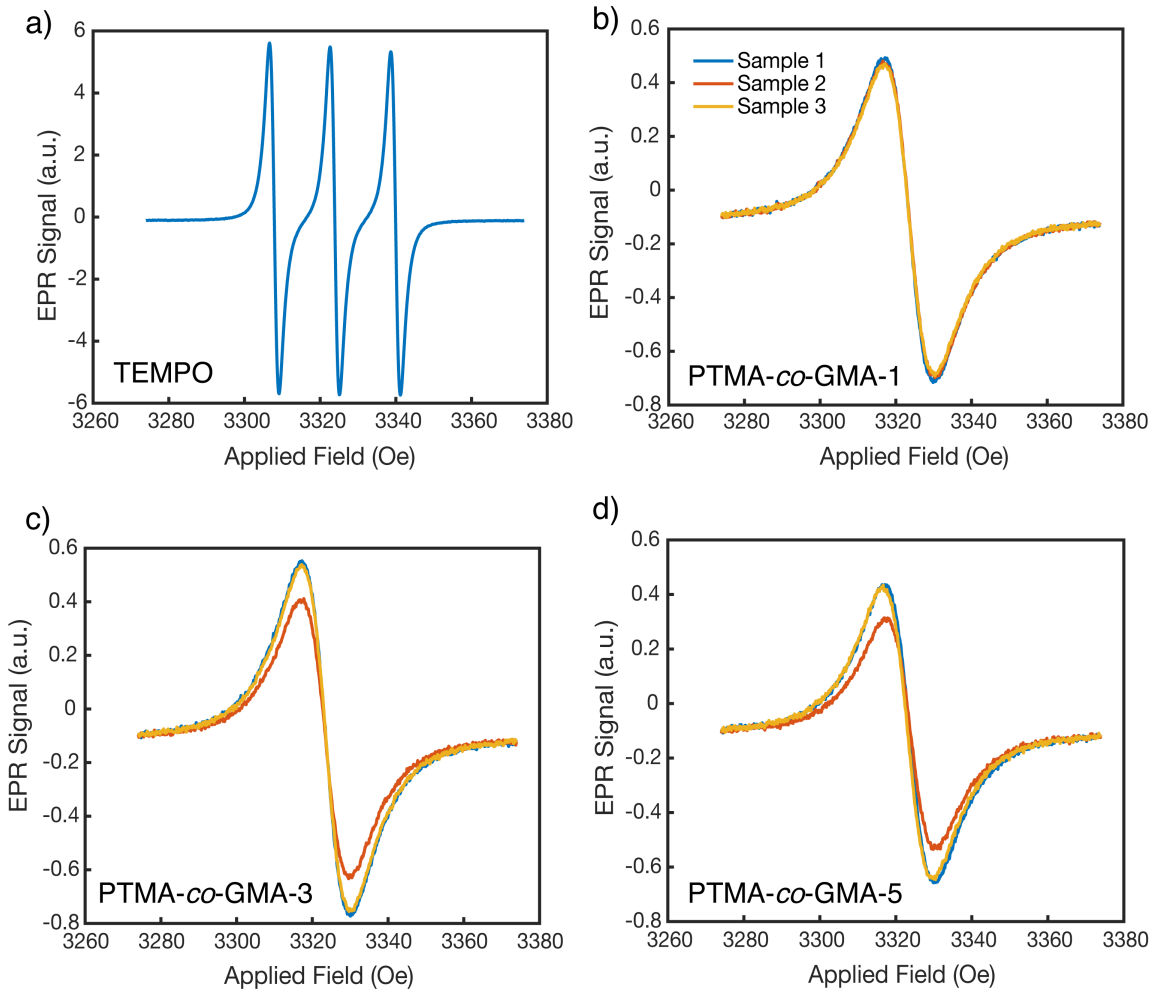

Figure 3-5. Solution state EPR for a) TEMPO-standard, b) PTMA-*co*-GMA-1, c) PTMA-*co*-GMA-3, and d) PTMA-*co*-GMA-5. All the measurements were taken at 1 mM in chloroform. Spectra for three independent samples are shown for each copolymer.

The molecular weight and dispersity ($Đ$) for PTMA-*co*-GMA copolymers are summarized in **Table 3-2**. As expected, copolymers generated from free radical polymerization yielded high molecular weights (M_n = 42,000-81,000 g/mol) and wide dispersity ($Đ$ = 2-4). The GMA content in the copolymers was estimated from NMR and summarized in **Table 3-3**. The GMA content in each copolymer is close to the mole percent of GMA added in the feed. The glass transition temperature (T_g) was approximately 165 °C for all three types of PTMA-*co*-GMA copolymers (**Figure 3-6**). The T_g values agree with previously reported values for homopolymer PTMA synthesized from controlled radical polymerization.[13]

Table 3-2. Number average and weight average molecular weight and dispersity for the uncrosslinked PTMA-GMA copolymers evaluated using GPC with RI and UV detectors.

Copolymers	RI			UV		
	M_n (g/mol)	M_w (g/mol)	PDI	M_n (g/mol)	M_w (g/mol)	PDI
PTMA-*co*-GMA-1	44400	137000	3.08	35400	132000	3.74
PTMA-*co*-GMA-3	81300	158000	1.95	70800	157000	2.22
PTMA-*co*-GMA-5	42600	157000	3.68	34600	154000	4.44

Table 3-3. The GMA content in the copolymer *vs*. in the feed. The GMA content in the random copolymer is roughly estimated by integrating the area under peak c (5.08 ppm, -CH-O in PTMPM) and peak f (3.25 ppm, -CH- in GMA) in Figure 3-2 to 3-4.

Copolymers	Integrated area under peak f	GMA content in the feed (mol%)	GMA content in the copolymer (mol%)
PTMPM-*co*-GMA-1	0.0139	1	1.4%
PTMPM-*co*-GMA-3	0.0341	3	3.3%
PTMPM-*co*-GMA-5	0.0552	5	5.2%

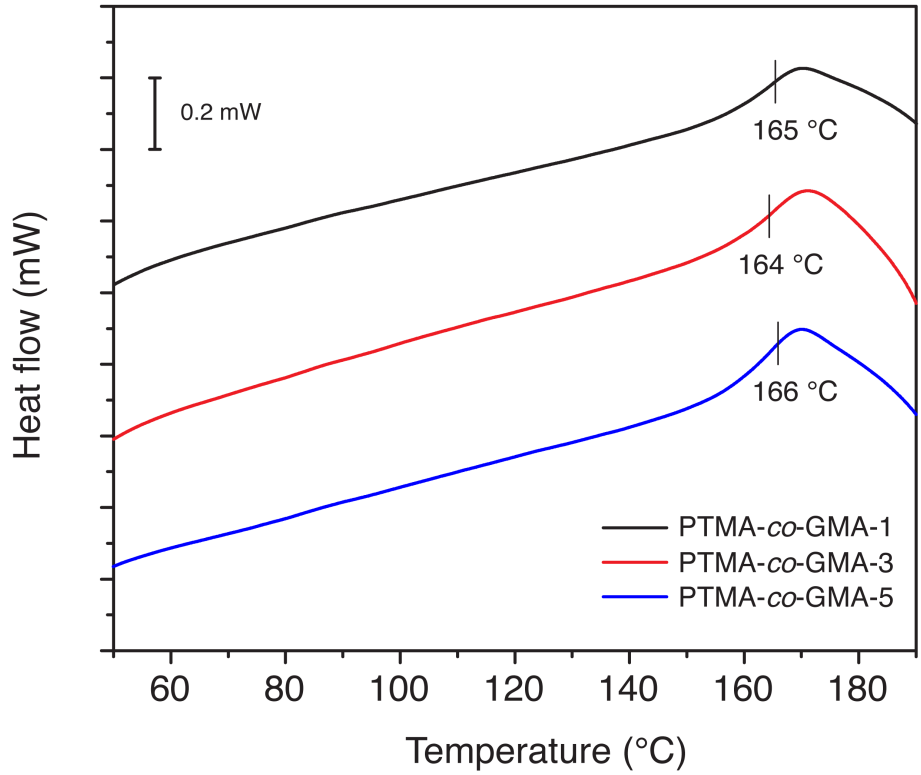

Figure 3-6. Differential scanning calorimetry for PTMA-*co*-GMA-1, -3, and -5. Scan rate of 10 °C/min, second heating scan shown, exo up.

PTMA-*co*-GMA copolymers were solution-cast from chloroform and either photo-crosslinked using a UV light source or thermally crosslinked at 175 °C overnight (above the T_g). The radical concentrations before and after crosslinking are summarized in **Table 3-1**. **Figure 3-7** shows the solid-state EPR response of PTMA-*co*-GMA-1, -3, and -5 films subjected to photo-crosslinking and thermal curing, respectively. Photo-crosslinking resulted in an 80% loss of the original radical content, whereas thermal crosslinking resulted in only a 22% loss for PTMA-*co*-GMA-1. As observed, photo-crosslinking drastically reduced the number of free radicals. This was likely because of the reactivity of nitroxide radical toward other radical species (*i.e.*, the free radicals generated by the photo-initiator), which leads to unwanted side reactions.[14] In contrast, thermal crosslinking retained over 70% of the free radicals, indicating that it is much more efficient than photo-crosslinking in terms of preserving radical density. For this reason, we restricted our investigations to thermally crosslinked PTMA.

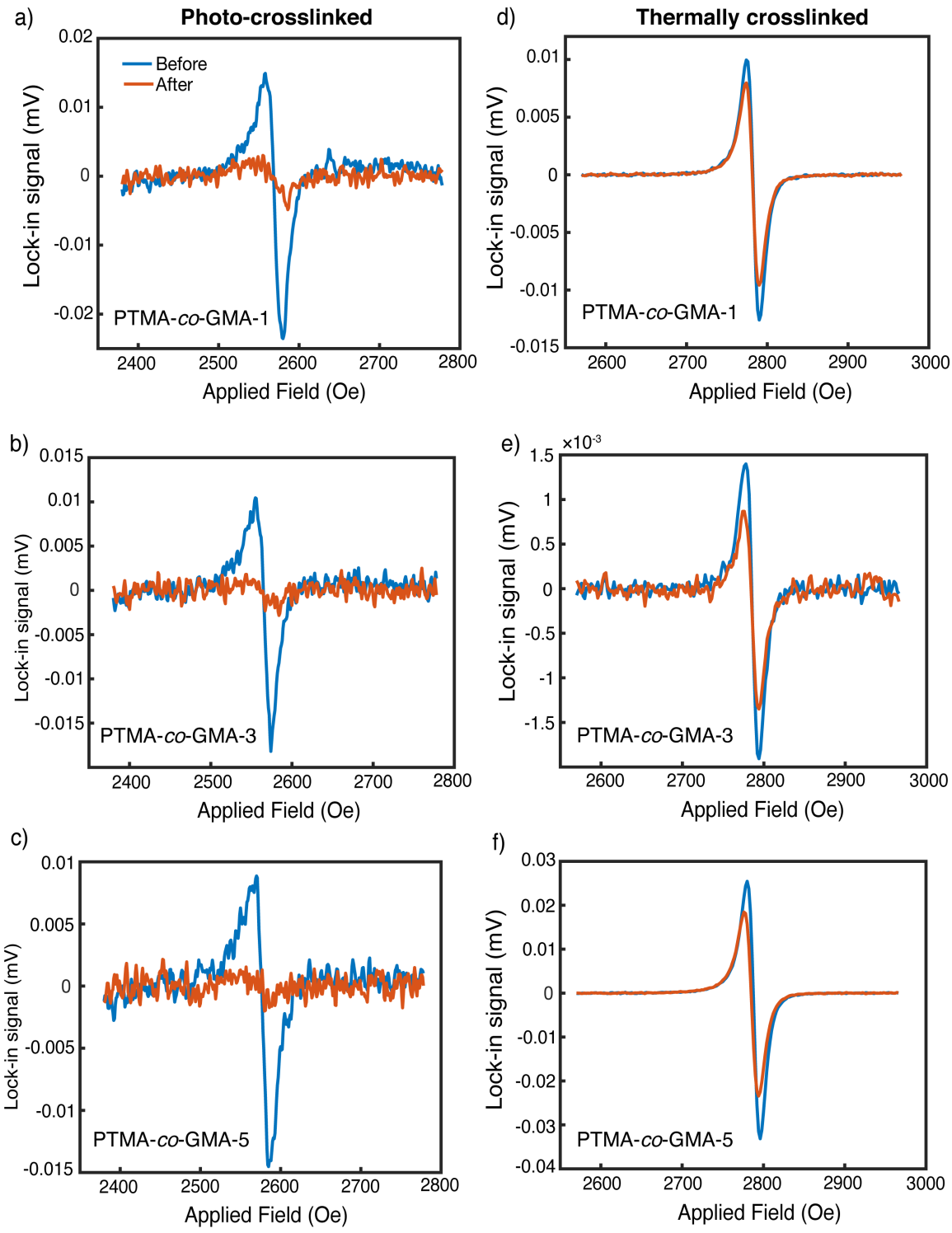

Figure 3-7. Solid-state EPR spectra before and after photo-crosslinking for a) PTMA-*co*-GMA-1, b) PTMA-*co*-GMA-3, and c) PTMA-*co*-GMA-5; Solid-state EPR spectra before and after thermal curing for d) PTMA-*co*-GMA-1, e) PTMA-*co*-GMA-3, and f) PTMA-*co*-GMA-5.

There are several possible reasons for the decrease in radical content during thermal curing. Because the oxidation reaction with mCPBA did not proceed to completion, the secondary amine in the six-membered TEMPO ring is capable of initiating epoxy-amine curing.[76] The nucleophilic amine nitrogen may attack the terminal carbon of the epoxy ring, forming a hydroxyl group on the epoxy oxygen.[82] However, we did not observe a broad hydroxyl peak in the FTIR spectra (**Figure 3-8**) obtained after thermal curing. Another possibility is that the N-O• radicals catalyzed epoxy curing. In the presence of a Lewis base, such as a tertiary amine, epoxy curing could occur via homo-polymerisation.[77] The nitroxide radical can form a resonance structure in which the oxygen withdraws one electron from the nitrogen.[3] In this case, the hybridized oxygen might act as a Lewis base and initiate epoxy homo-polymerization to form a bond with the terminal carbon in a second epoxy ring. This curing process does not generate any hydroxy groups and possibly explains the decrease in radical concentration after photocuring.

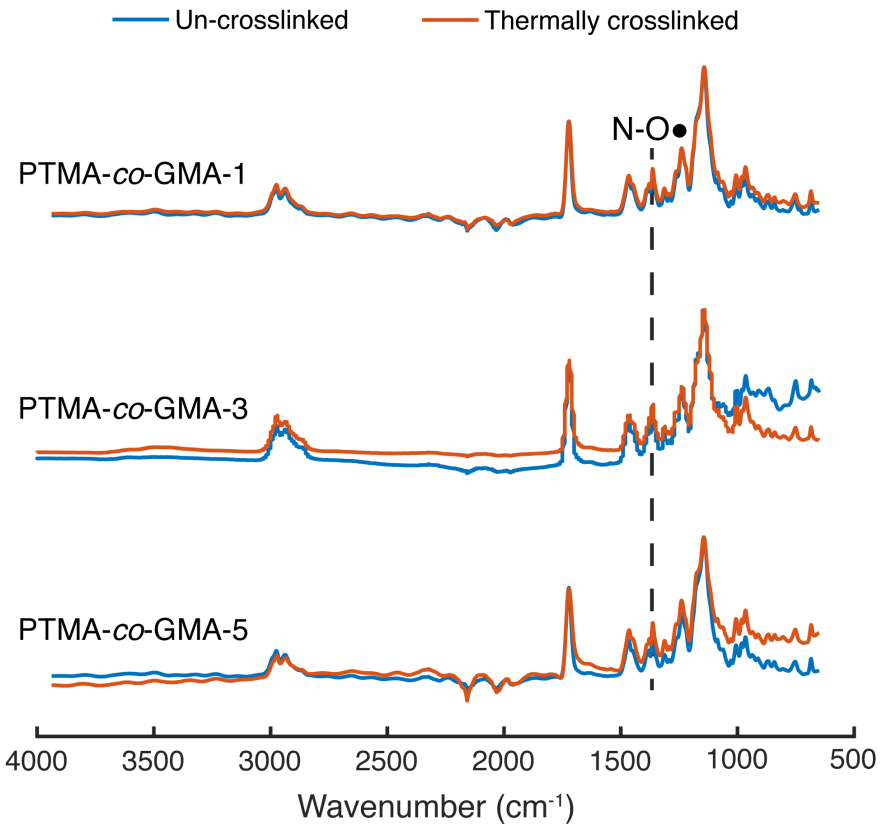

Figure 3-8. FTIR spectra before and after thermal crosslinking for PTMA-*co*-GMA-1, PTMA-*co*-GMA-3, and PTMA-*co*-GMA-5.

3.4. Swelling Ratio

QCM-D was used to measure the swelling ratio of crosslinked PTMA-*co*-GMA films in 1:1 ethylene carbonate/diethyl carbonate solvent to evaluate the effect of crosslinking density on cell performance. Assuming that swelling occurs exclusively in the z-direction (*i.e.* an increase in thickness)[79], the swelling ratio can be calculated by taking the ratio of swollen film thickness to the dry film thickness. As an example, the stitched baselines for PTMA-*co*-GMA-5 in air and in solvent are shown in **Figure 3-9.**

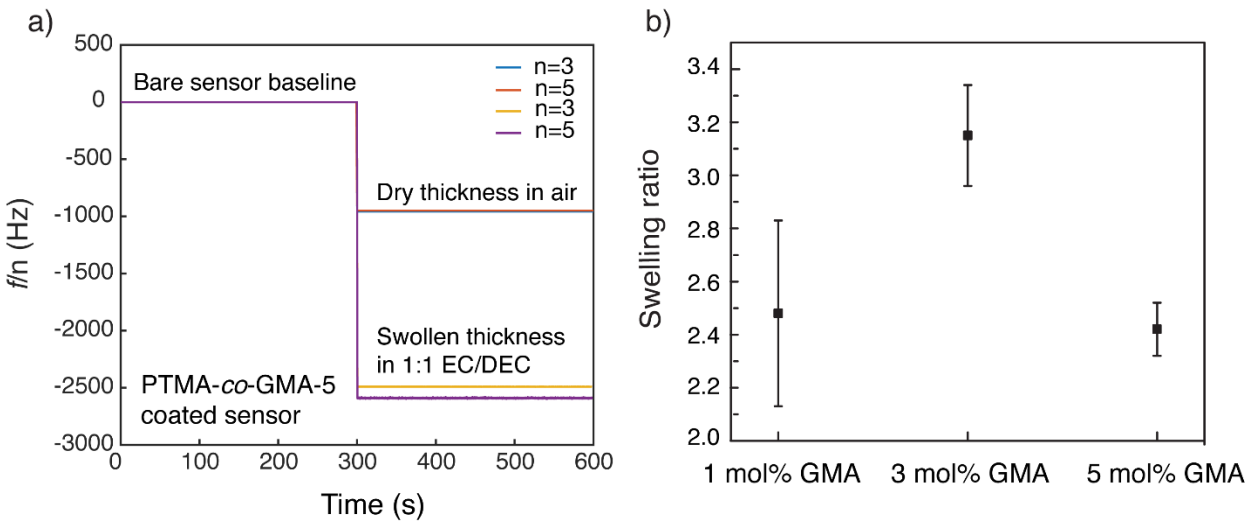

Figure 3-9. a) Frequency/overtone response for a bare sensor (t < 300s) stitched together with that of a PTMA-*co*-GMA-5-coated sensor (t > 300 s) either dry (in air) or swollen (in 1:1 EC/DEC by volume). The 3rd and 5th overtones are considered. b) Calculated swelling ratio of PTMA-*co*-GMA films, where the ratio is obtained by dividing the swollen thickness by the dry thickness.

The estimated dry film thicknesses for all the spin-coated samples were approximately 110–170 nm. The swelling ratios, calculated as the swollen thickness divided by the dry thickness, were 2.5 ± 0.4, 3.2 ± 0.2, and 2.4 ± 0.1 for PTMA-*co*-GMA-1, -3, and -5, respectively. In principle, swelling decreases with increasing crosslinking density, because there is less free volume in the denser crosslinked network for solvent penetration. Within error, the swelling ratios were all similar in value. In general, the polymers doubled or tripled in thickness upon exposure to the solvents.

3.5. EQCM-D Response during Cyclic Voltammetry

After measuring the swelling ratio, we recorded the QCM-D response during cyclic voltammetry (CV) at different scan rates in a three-electrode configuration. **Figure 3-10** shows a

representative sample of the raw data for PTMA-*co*-GMA-1, PTMA-*co*-GMA-3, and PTMA-*co*-GMA-5 during three CV cycles each at 0.5, 1, and 2 mV s^{-1}. The frequency of the third overtone is presented, in which increasing frequency indicates a decrease in the solvated mass of the polymer and *vice versa*. The QCM-D response tracked well with the redox peaks affiliated with the PTMA copolymers, as we have previously observed for a PTMA homopolymer.[32] As the copolymer oxidizes, the nitroxide radical is converted to an oxoammonium cation by doping with the triflate anion; this results in an overall electrode mass increase and a decrease in frequency, **Figure 3-10 a-c**. Upon reduction, the reverse process occurs, the triflate ion is released to the external solution, the electrode mass decreases, and the frequency increases.

Next, we examined the frequency drift over the course of a 6 h experiment to understand the longer-term dissolution or swelling of the copolymer. The frequency response of PTMA-*co*-GMA-1 showed a positive drift (**Figure 3-10a**), which corresponded to a 1.4% mass loss over the course of the 6h experiment; this observation confirmed that dissolution of a small amount of PTMA-*co*-GMA-1 occurred. However, this mass loss was negligible compared with that of homopolymer PTMA, which lost 14% of its original mass in its first 10 min of solvent exposure.[32] In contrast, the frequency gradually decreases over time, reflecting gradual swelling during cyclic voltammetry for PTMA-*co*-GMA-3 and -5 (**Figure 3-10b,c**). Specifically, PTMA-*co*-GMA-3 and -5 showed mass increases of 1.1% and 0.9 %. This observation is consistent with the gradual penetration of electrolyte into the polymer electrode aided by the cycling process. Therefore, we conclude that 1 % GMA is the minimal amount needed to effectively crosslink the PTMA electrode.

The response shapes for PTMA-*co*-GMA-1 and -3 were different from that of PTMA-*co*-GMA-5. The response of the former exhibit flat plateaus (similar to that observed with PTMA

homopolymer) and frequency changes that did not change much in magnitude at varying scan rates. The response of the latter showed a peak in frequency during reduction but a flat profile during oxidation. The frequency modulation decreased with scan rate for PTMA-*co*-GMA-5. These features may be related to the varying ion transport mechanism for PTMA-*co*-GMA-5 (see below) and possible concentration polarization due to the increased crosslinking in the PTMA film.

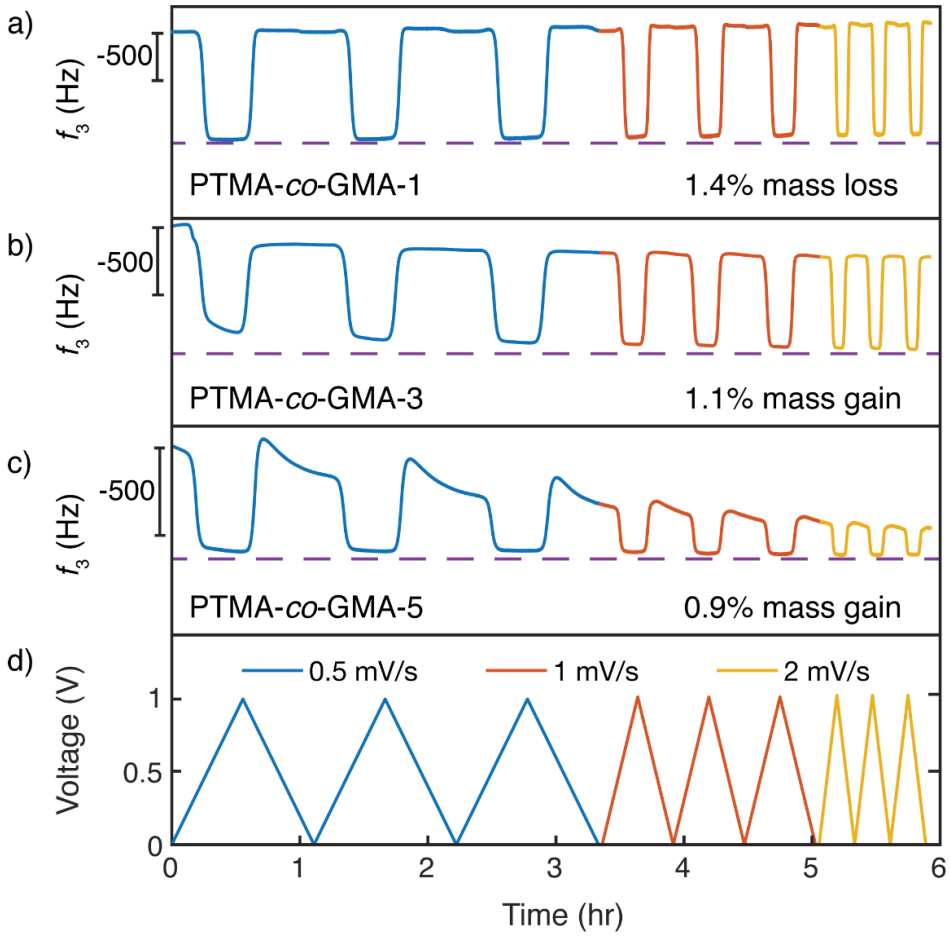

Figure 3-10. EQCM-D raw frequency (f_3) for a) PTMA-co-GMA-1, b) PTMA-co-GMA-3, and c) PTMA-co-GMA-5 during cyclic voltammetry at 0.5, 1, and 2 mV s^{-1}, in which the voltage profile is shown in (d).

3.6. The Doping Mechanism of Crosslinked Electrodes

The CV responses of the copolymer films during EQCM-D at multiple scan rates are shown in **Figure 3-11**. The peak current scaled with $\nu^{1/2}$ in all cases, consistent with a diffusion-limited process. As scan rate increased from 0.5 mV s^{-1} to 100 mV s^{-1} the peak potential separations increased from 19 mV to 221 mV, 13 mV to 222 mV, and 12 mV to 153 mV for PTMA-*co*-GMA-1, -3, and -5, respectively. The diffusion coefficient (D) of charge propagation was calculated using the Randles-Sevcik Equation. For PTMA-*co*-GMA-1, -3, and -5 the diffusion coefficients were 1.6×10^{-12}, 7.2×10^{-13}, and 8.1×10^{-12} cm^2/s, respectively. These values are about 2-3 orders of magnitude smaller than that of homogeneous PTMA, indicating that charge transfer in the crosslinked electrodes might be affected by limited physical diffusion of the redox centers in the network.[31] The redox potentials all appeared around 0.6 V *vs*. Ag wire quasi-reference electrode (QRE), with the response of PTMA-*co*-GMA-5 having a slightly lower redox potential. This may be due to uncertainty in using a QRE in which the redox potential can drift during the experiment, or else due to the more highly crosslinked structure of PTMA-*co*-GMA-5, which may yield a tighter radical packing and a slightly lower redox potential. We have also conducted internal voltage corrections using ferrocene and found that the redox potential of the three copolymers were all around 0.4 V *vs*. ferrocene/ferrocenium, which corresponds to 3.6 V *vs*. Li/Li^+. Thus, the redox potentials of the copolymers are consistent with that reported in the literature.[3]

The CV response of each copolymer at a scan rate of 1 mV s^{-1} are shown in **Figure 3-11a**. Of particular note are the overlapping peaks or shoulders observed in the cathodic scans for each copolymer. The lower potential feature was attributed to doping of the radical as dominated by Li-ion transport, and the higher potential feature was assigned to doping of the radical as

dominated by $CF_3SO_3^-$ transport, as observed elsewhere for homopolymer PTMA.[32] First focusing upon PTMA-*co*-GMA-1, the lower potential cathodic peak dominated at low scan rate, and the two features merged into one peak as scan rate increases; this suggested the prominence of Li-ion transport at slower time scales but mixed ion transport at faster time scales. Similar doping behavior has been previously observed in homopolymer PTMA.[32] Next, focusing upon PTMA-*co*-GMA-5, we observe a different trend in which the higher potential peak dominated at 1 mV s^{-1}, with merging of the two peak features as the scan rate increased; this suggested the prominence of $CF_3SO_3^-$ transport at slower time scales, with a shift to mixed ion transport at faster time scales. Comparing PTMA-*co*-GMA-1 and PTMA-*co*-GMA-5, we observed the dominance of the Li-ion and anion transport at 1 mV s^{-1}, respectively, as indicated by the reversed peak features. The reason for this is not immediately clear, but we speculate that the results may be owing to differences in free volume of the copolymers and trapping of the electrolyte into the crosslinked film.

With a higher crosslinking density, PTMA-*co*-GMA-5 should have less free volume for ion transport within the swollen film. As scan rate increases, the time scale of diffusion decreases, which is further impaired by the lower free volume. This should lead to a shift to the transport of the most mobile species (in this case the lithium ion). Indeed, this effect is observed in the EQCM-D raw data for PTMA-*co*-GMA-5, **Figure 3-10c**. As the scan rate increased, the mass change in the film decreased (the overall frequency change decreased), as transport shifted from being dominated by more massive anions to less massive lithium ions.

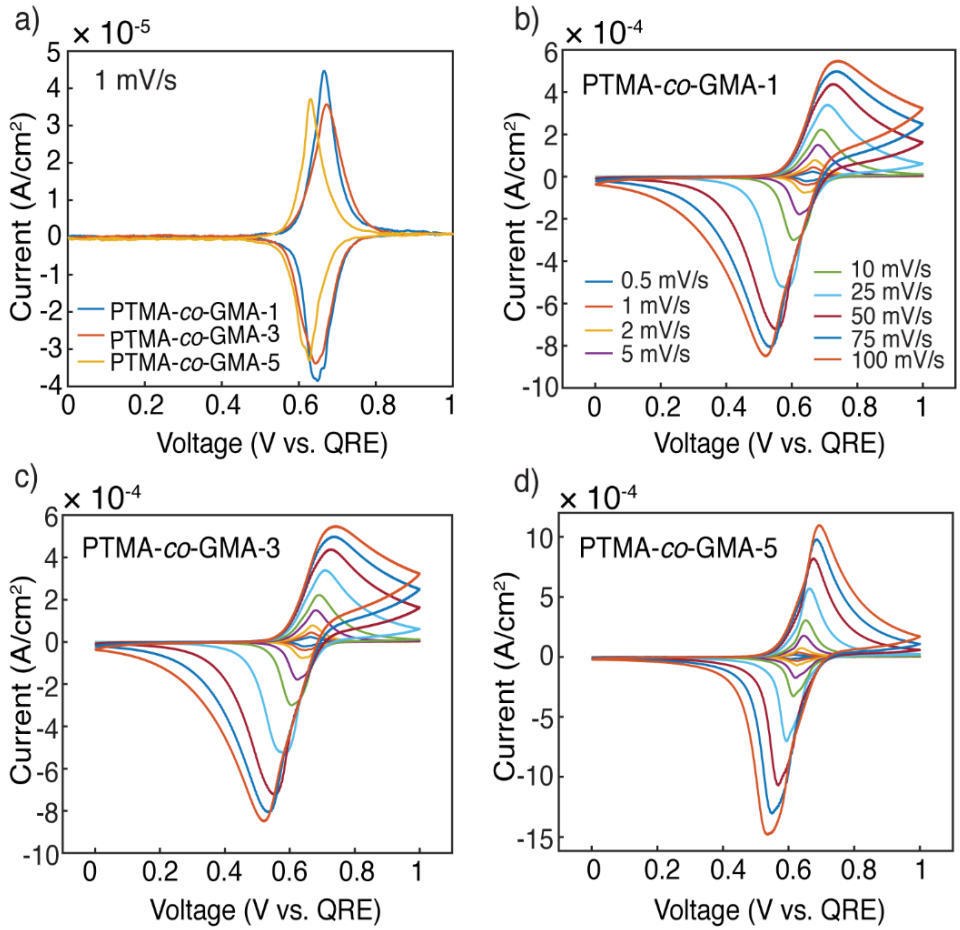

Figure 3-11. Cyclic voltammetry for a) all three copolymers at 1 mV s^{-1}, b) PTMA-*co*-GMA-1, c) PTMA-*co*-GMA-3, and d) PTMA-*co*-GMA-5 at the indicated scan rates. The legend in (b) also applies to (c) and (d).

3.7. Electrochemical Performance

Finally, we conducted electrochemical tests on two-electrode coin cells assembled from uncrosslinked and thermally cured PTMA-*co*-GMA electrodes. Each electrode contained 60 wt% vapor-grown carbon fiber, 30 wt% PTMA-*co*-GMA, and 10 wt% PVDF binder. Thermal curing proceeded at 175 °C for 3 h for the composite electrodes. SEM images (**Figure 3-12**) show no significant morphology changes upon crosslinking. The cells were subjected to galvanostatic

cycling at varying C-rates, **Figure 3-13 a-c**. The charge-discharge profile at 0.1 C (**Figure 3-13d**) indicated that all the PTMA-co-GMA copolymers exhibit a plateau at 3.6 V *vs*. Li/Li^+, consistent with redox potential of PTMA. In general, the crosslinked cells exhibited much higher capacities compared to the uncrosslinked cells, especially at higher C-rates. Specifically, crosslinked PTMA-*co*-GMA-1 exhibited a capacity of 104 mAh g^{-1} at 0.1 C, as compared to a capacity of 57 mAh g^{-1} for its uncrosslinked analogue (using PTMA as the basis). To compare across the crosslinked cells, PTMA-*co*-GMA-1 generally showed the highest capacity, ranging from 104 mAh g^{-1} at 0.1 C to 82 mAh g^{-1} at 5 C. The reason for this is likely because PTMA-*co*-GMA-1 also had the highest radical content, having the lowest amount of GMA of the three copolymers investigated.

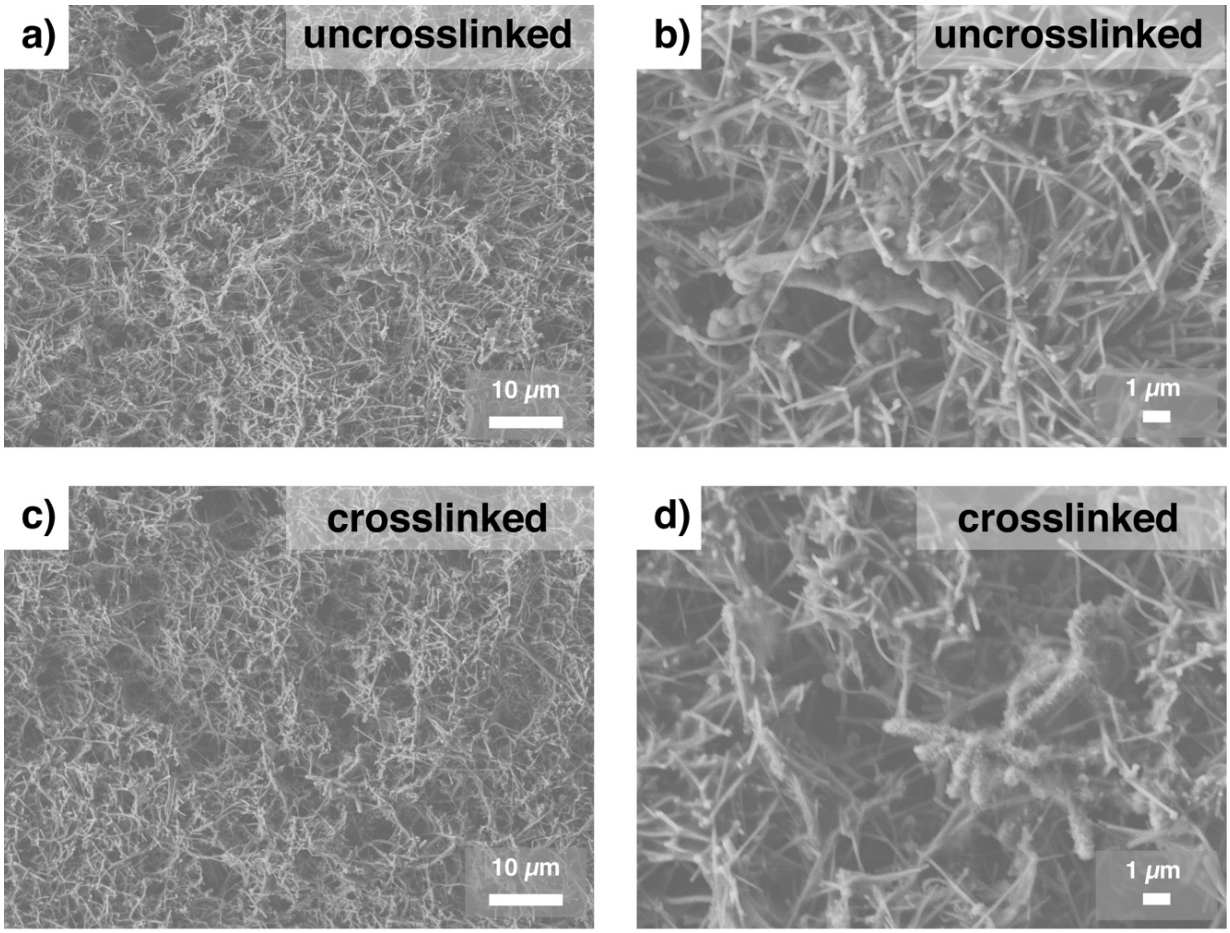

Figure 3-12. SEM images of PTMA-*co*-GMA-5.

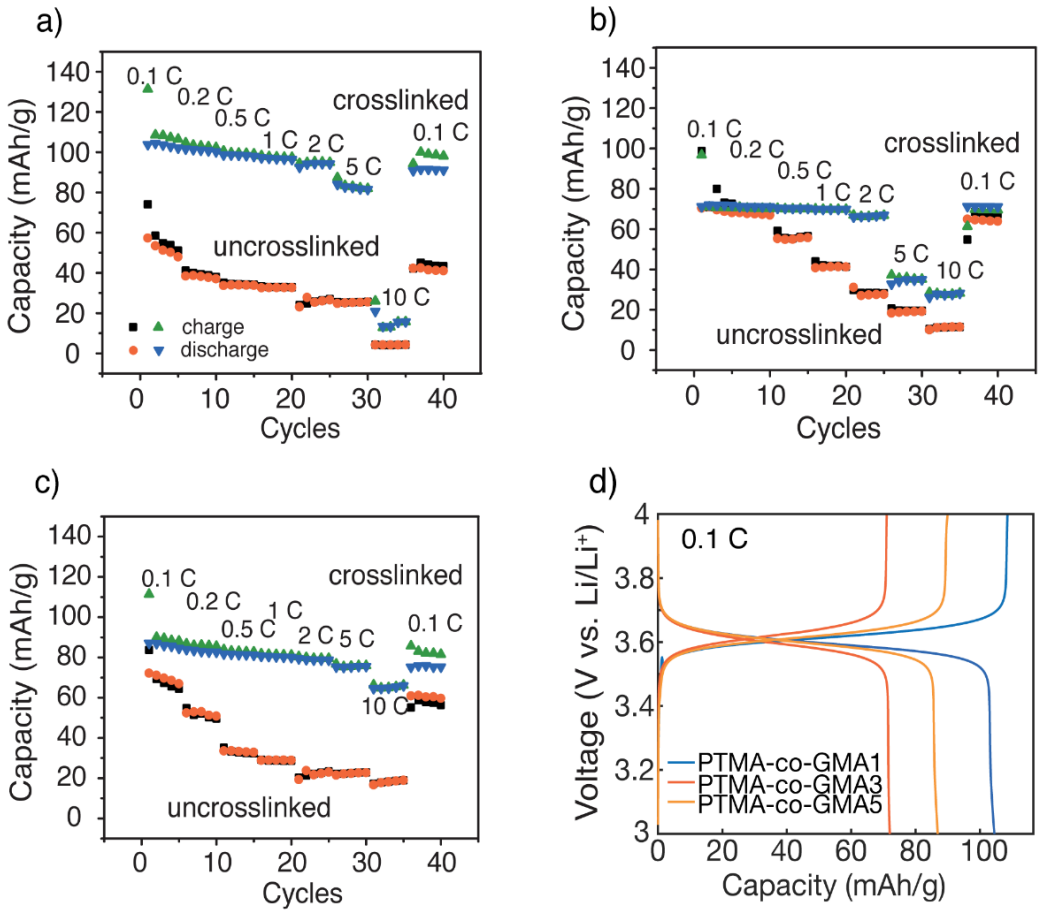

Figure 3-13. Capacity measured at various C-rates for a) PTMA-*co*-GMA-1, b) PTMA-*co*-GMA-3, and c) PTMA-*co*-GMA-5; d) charge discharge profile for crosslinked PTMA-*co*-GMA-1, -3 and -5.

Finally, the cells were cycled at 1 C for 50 cycles, **Figure 3-14**. PTMA-*co*-GMA-3 showed the best capacity retention (99.6%), followed by PTMA-*co*-GMA-5 (97.8%) and PTMA-*co*-GMA-1 (95.1%). This result was consistent with our previous swelling ratio and QCM-D measurements. Because PTMA-*co*-GMA-1 is partially crosslinked, it is more prone to partial dissolution and thus exhibited the lowest capacity retention. In comparison, the uncrosslinked cells showed capacity retentions of 86 – 94%.

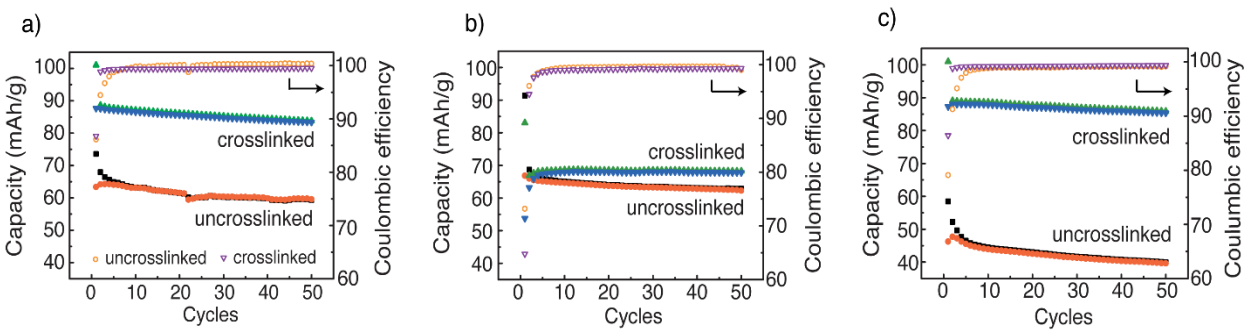

Figure 3-14. Cycling at 1 C for 50 cycles for a) PTMA-*co*-GMA-1, b) PTMA-*co*-GMA-3, and c) PTMA-*co*-GMA-5.

We calculated the absolute values of the capacities observed relative to the radical concentration. Given 100% radical functionalization and the given GMA contents, we would expect PTMA-*co*-GMA-1, -3, and -5 to have radical compositions of 99, 97, and 95%. At the same time, oxidation leads to incomplete nitroxide conversion and crosslinking also diminishes the radical content. The cells shown in **Figure 3-13 and 3-14** were crosslinked for only 3 h, and those in listed **Table 3-1** were crosslinked overnight. Therefore, we expect the radical concentrations of the copolymer to be bound by the theoretical values here and those in **Table 1**. This, in turn, would lead to possible theoretical capacities for PTMA-*co*-GMA-1, -3, and -5 of 69.5 to 90.5, 61.2 to 95.9, and 54.5 to 84 mAh g^{-1}, respectively. The fact that we observed capacities in excess of these value for some cases indicates some energy storage contribution from the carbon fiber additives. The different battery performance of PTMA-co-GMA-3 might be attributed to effects of spin concentration, crosslinking mechanism, and free volumes in the copolymer network.

3.8. Conclusion

A radical copolymer that could be solution-processed, mixed with carbon, and thermally cured into a functional organic battery cathode was developed. Prior to this report, existing radical polymers could be crosslinked but are either intolerant to including carbon in thicker electrode configurations or have a low capacity. We examined poly(2,2,6,6-tetramethylpiperidinyloxy-4-yl methacrylate) (PTMA) containing relatively low amounts of glycidyl methacrylate (GMA) crosslinker to identify the minimal amount of crosslinker required to prevent dissolution of the active material. It was determined that 3 mol% GMA crosslinker lead to the best capacity retention (99.6%) and that 1 mol% GMA crosslinker led to the highest capacity (104 mAh g^{-1}). We also compared the relative efficacy of photo-crosslinking and thermal crosslinking and determined thermal crosslinking was most effective. This was because photo-crosslinking generated undesirable side reactions that consumed active radical sites and because light could not easily penetrate through thick carbon-containing electrodes.

For future design, it is recommended to identify crosslinking chemistries that form a network with the addition of minimal amount of crosslinker, preserve radical content through the crosslinking reaction, and maintain enough free volume to facilitate penetration and transport of the electrolyte during the redox reaction. In addition, it may be useful to examine other battery electrolytes, because they may exhibit different degrees of network swelling, leading to different or improved performance.

4. INTERNAL CHARGE TRANSFER IN REGIO-REGULAR CONJUGATED RADICAL POLYMERS*

4.1. Introduction

Although PTMA exhibits a fast redox reaction, the long-range electronic conductivity in PTMA is rather low, on the order of 10^{-6} -10^{-11} S cm^{-1}.[13, 51, 83] Therefore, most cathodes contain 30 to 90 wt% conductive carbon additive to promote charge transfer at the expense of diluting active materials and energy density.[10, 15, 17, 84] More recently, conjugated radical polymers (CRPs) have been proposed as an alternative means to boost conductivity and increase capacity,[85] but no success has yet been achieved due to internal charge transfer between the radical moiety and the conjugated backbone.[86, 87]

Electron transfer in PTMA occurs via a hopping mechanism between free radicals and adjacent oxoammonium cations.[31] Specifically, the heterogeneous electron transfer (polymer electrode to current collector) rate constant (k^0) is on the order of 10^{-1} – 10^{-2} cm^2 s^{-1}, and the electron self-exchange reaction rate constant (k_{ex}) is on the order of 10^8 M^{-1} s^{-1}.[31, 45-47] In contrast, conjugated polymers facilitate charge transfer through delocalized π electrons in the conjugated backbone and achieve long-range conductivity, exhibiting redox activity through doping and de-doping of the backbone.[88-90] On the other hand, CRPs build upon typical conjugated polymer backbones such as polythiophene,[86, 91, 92] polypyrrole,[93, 94] PEDOT,[95] polydithienopyrrole,[87] and

---

* Modified and reprinted with permission from the Royal Society of Chemistry. https://doi.org/10.1039/D0SC03567J "Quantifying internal charge transfer and mixed ion-electron transfer in conjugated radical polymers" by Shaoyang Wang, Alexandra D. Easley, Ratul M. Thakur, Ting Ma, Junyeong Yun, Yiren Zhang, Christopher K. Ober, and Jodie L. Lutkenhaus, *Chemical Science*, 2020, 11, 9962 – 9970, Copyright 2020, the Royal Society of Chemistry

polyacetylene[96, 97] by installing redox active groups (usually TEMPO). Most CRPs exhibit lower capacity and conductivity than expected (24–115 mAh g^{-1} and 10^{-13} to 10^{-2} S cm^{-1}). Reasons cited include: electropolymerization leading to partly soluble (oligomeric) materials that cause capacity decay;[98] the redox potential of the conjugated backbone depends on the degree of doping, which often overlaps with the redox potentials of nitroxide radicals;[99] and the rapid redox kinetics of nitroxide radicals compete with the sluggish redox kinetics of the conjugated backbone.[85]

To summarize, the reason for the poor performance of CRPs thus far is related to the internal transfer of electrons between the redox-active side group and the redox-active conjugated backbone. The direction of electron transfer depends upon the relative redox potentials of the two species, as we have demonstrated previously for polythiophene-TEMPO and polydithienopyrrole-TEMPO CRPs.[86, 87] Specifically, we attached TEMPO pendant radicals to polythiophene (P3HT) backbones, whose redox potential was above the TEMPO radical (3.88 V and 3.6 V *vs*. Li/Li^+, respectively) to obtain P3HT-TEMPO.[86] Internal charge transfer was observed by monitoring the open circuit potential (OCP) after charging, in which the OCP dropped quickly from 4.2 V to 3.9 V within the first 1000 s.[86] This coincided with some unoxidized TEMPO transferring an electron to de-dope the oxidized polythiophene, as confirmed using spectroelectrochemistry.[86] As a result, the OCP relaxed to that of the species with the lower redox potential – TEMPO, 3.6 V *vs*. Li/Li^+.[86] We have also observed similar internal charge transfer in TEMPO-bearing poly(dithieno[3,2-b:2',3'-d]pyrrole) (poly(DTP-TEMPO)).[87] The OCP of poly(DTP-TEMPO) had a sharp decrease to from 4.1 V to 3.6 V within the first hour, and eventually relaxed to 3.0–3.1 V, which is the redox potential of the DTP unit.[87] Again, it seems that the internal charge transfer occurs so that the lowest redox potential is achieved.

In the above-mentioned studies, the polymers were synthesized using electropolymerization, leading to insoluble CRPs with poor control. This approach prevented traditional characterization such that the molar mass or regioregularity could not be examined. This prevented quantification of the internal charge transfer mechanism and reduced the phenomena to a qualitative understanding. This knowledge is important so that one might design these polymers as charge or voltage regulators in one case or as materials for energy storage in another case.

Fortunately, access to controlled regioregular P3HT-TEMPO polymers with various TEMPO loadings (**Figure 4-1**) has been recently reported by Zhang et al.[100] TEMPO units were clicked onto a polythiophene backbone made from controlled amounts of 2,5-dibromo-3-hexylthiophene (HT) and 2,5-dibromo-3-(6-bromohexyl)thiophene (BrHT), modified with an azide.[100] The final TEMPO-bearing P3HT was denoted as P3HT-TEMPO-*X*, in which *X* refers to the intended percent radical loading. The authors found that the solid-state conductivity decreased exponentially with increasing TEMPO loading for two reasons.[100] First, bulky TEMPO groups twisted the polymer backbone, making it less planar and reducing the conjugation length.[100] As a result, intrachain electron transfer through the backbone was impeded.[100] Second, the steric hinderance of TEMPO side groups disrupted polymer packing and crystallization.[100] At low TEMPO loading (25%), P3HT-TEMPO was semi-crystalline, which allowed for interchain electron transfer; at high TEMPO loading (50–75%), P3HT-TEMPO formed amorphous aggregates, causing a higher energy barrier for interchain electron transfer.[100] Although the solid-state conductivity was examined for P3HT-TEMPO-*X*, the electrochemical behavior – and likewise the internal charge transfer – remained unknown.

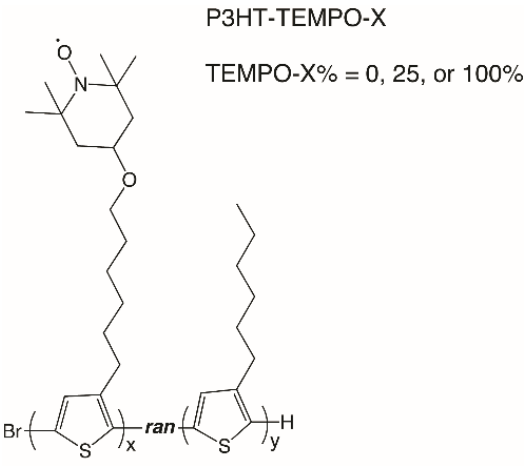

Figure 4-1. Chemical structure of P3HT-TEMPO-*X*.

Here, we quantify the internal electron transfer behavior of regioregular P3HT, P3HT-TEMPO-25 and P3HT-TEMPO-100 in the presence of nonaqueous electrolyte, along with the coupled ion transport. The general electrochemical behavior was probed using cyclic voltammetry and galvanostatic charge-discharge of the solution-cast polymers. To characterize the relative capacity contributions from the different redox-active moieties (i.e., TEMPO radicals and the conjugated backbone), galvanostatic charge-discharge at various cutoff voltages was performed. The internal charge transfer was characterized through both OCP monitoring and decoupling of the faradaic and non-faradaic contributions for the first time. This is further quantified using electrochemical quartz crystal microbalance with dissipation monitoring (EQCM-D), which examines *in situ* ion transport associated with doping of the two redox active species, for the first time. These results provide a fundamental understanding of electron transfer within the CRPs, and in return, it will guide future design of redox polymers exhibiting both high conductivity and fast charging.

4.2. Materials and Methods

4.2.1. Materials

P3HT, P3HT-TEMPO-25 and P3HT-TEMPO-100 were provided by Zhang et al., as synthesized in their recent publication.[100] The reported regioregularities of P3HT-TEMPO-25 and P3HT-TEMPO-100 were 89% and 93%, respectively, and the actual radical concentration in P3HT-TEMPO-25 was only 20% *vs*. 80% in P3HT-TEMPO-100.[100] The molecular weights of P3HT-TEMPO-25 and P3HT-TEMPO-100 were 5.9 and 9.2 kDa, respectively. The solid-state conductivities of P3HT, P3HT-TEMPO-25 and P3HT-TEMPO-100 were 7×10^{-5}, 2×10^{-7}, and 3.8×10^{-11} S cm^{-1}, respectively.[100] All other chemicals were used as received from Sigma-Aldrich unless otherwise noted.

4.2.2. Three-electrode Cell Assembly

Indium tin oxide-coated glass (ITO, Delta Technologies) was used as the substrate for the working electrode. 1 mg of P3HT and P3HT-TEMPO-25 were each dissolved in 1 ml of chloroform. 1 mg of P3HT-TEMPO-100 was dissolved in 1 ml of 1,4-dioxane with heat. 60–100 μL of the solution was drop-cast onto ITO-coated glass and the mass loading varied from 0.3 to 0.5 mg cm^{-2}. Typical active areas were 2.5–3.5 cm^2. The counter and reference electrode were both lithium foils. The electrolyte was 0.5 M lithium triflate ($LiCF_3SO_3$) in ethylene carbonate/diethyl carbonate (EC/DEC, 3/7 by volume). The electrodes were assembled in a three-neck flask under inert conditions in an argon-filled glove box.

4.2.3. Electrochemical tests

All electrochemical tests were conducted using a Solartron 1260/1280. The polymer film was conditioned at 10 mV s^{-1} for 10 cycles first, followed by cyclic voltammetry at 0.5, 1, 2, 5, 10, 25, and 50 mV s^{-1}, 3 cycles at each scan rate. Subsequently, galvanostatic charge-discharge

was conducted at 5, 10, and 20 μA cm^{-2} from 3 V to 4.2 V *vs*. Li/Li^+, three cycles at each current density. To isolate the contribution of the TEMPO radical and the conjugated backbone, the cell was charged from 3 V to various potential cutoffs at 3.5, 3.6, 3.7, 3.8, 4.0 and 4.2 V, three cycles under each voltage. Considering the difference in capacity and charge-discharge profiles, P3HT was charged at a higher current of 5 μA cm^{-2}, whereas P3HT-TEMPO-25 and P3HT-TEMPO-100 were charged at 2 μA cm^{-2}. Electron impedance spectroscopy (EIS) was performed over a frequency range of 10 mHz to 1 MHz with a perturbation voltage of 10 mV and the cell was tested at 3.6 V, 3.8 V and 4.0 V. At last, the cell was charged to 4.2 V and held at this potential for 30 min. The open circuit potential (OCP) was monitored for 6 h after removing the bias. The electrochemical cell was stored under inert conditions for the course of the experiments.

4.2.4. EQCM-D Measurements

Gold-coated, planar AT-cut quartz crystals (QSX 338) with a fundamental frequency of 4.95 MHz were used as substrates for EQCM-D (Biolin Scientific). Detailed cleaning and substrate preparation procedures are reported in our previous publications.[32, 101] The stock solution for spin-coating was prepared by dissolving 10 mg of P3HT in 1ml chloroform, and 10 mg of P3HT-TEMPO-100 in 1 ml 1,4-dioxane with medium heat. (P3HT-TEMPO-25 was not presented because it yielded inconsistent results). A thin layer of the polymer was deposited on the sensor by spin-coating 40 μL of the stock solution at 500 rpm for 1 min. Electrochemical measurements were done in a three-electrode cell in which the working electrode was the polymer-coated quartz crystal, the counter electrode was Pt plate, and the quasi-reference electrode (QRE) was silver wire. The electrolyte was 0.5 M $LiCF_3SO_3$ in propylene carbonate. The frequency and dissipation response in EQCM-D was monitored during cyclic voltammetry at various scan rates. Electrode mass was modelled using the Voigt model and the parameters

were the same as our previous publication.[32] The charge was normalized by the active area of the sensor (1.13 cm^2).

4.3. Cyclic Voltammetry

The fundamental electrochemical responses of the three polymers were first compared to examine the effect of radical loading on the redox behavior. Cyclic voltammograms of P3HT, P3HT-TEMPO-25, and P3HT-TEMPO-100 at 0.5 mV s^{-1} are plotted in **Figure 4-2 a-c**. P3HT exhibited one oxidation peak at 3.84 V and two reduction peaks at 3.80 V and 3.36 V *vs.* Li/Li^+(**Figure 4-2a**); this response is consistent with prior reports for P3HT.[102-104] P3HT-TEMPO-100 showed a similar current response as that of PTMA,[10] in which a reversible redox couple at $E_{1/2}$ = 3.68 V *vs.* Li/Li^+ was observed (**Figure 4-2c**); thus, this peak is assigned to the nitroxide radical. On the other hand, P3HT-TEMPO-25 displayed mixed behavior, in which a rectangular capacitive response was superimposed on a redox peak ($E_{1/2}$ = 3.69 V *vs.* Li/Li^+) (**Figure 4-2b**). The capacitive response is attributed to the P3HT backbone, and the peak is attributed to the TEMPO functional group.

As scan rate increases, the redox peaks become less obvious and the cyclic voltammograms become distorted for all three polymers (**Figure 4-2 d-f**). Specifically, the anodic peaks disappear when the scan rate is above 2 mV s^{-1}, 10 mV s^{-1}, and 10 mV s^{-1} for P3HT, P3HT-TEMPO-25, and P3HT-TEMPO-100, respectively. On the contrary, most cathodic peaks remain present with increasing scan rate. The cathodic peaks persist up to a scan rate of 5 mV s^{-1} for P3HT and persist for all scan rates for P3HT-TEMPO-25 and P3HT-TEMPO-100. Such asymmetry between anodic and cathodic scans is commonly seen in conjugated polymers.[58, 103, 105]

Notably, the shape of the cathodic current response is largely affected by the radical loading. As the TEMPO loading increased from P3HT-TEMPO-25 to P3HT-TEMPO-100, the cathodic peak became sharper and closer to the current response of homopolymer PTMA.[10] This reflects that the process shifted from delocalized electron transport to localized electron hopping under higher radical loading.

In P3HT-TEMPO-100, electron transfer likely occurs via hopping between adjacent TEMPO sites, because the bulky TEMPO radicals impede polymer packing which then prevents charge transfer along the conjugated polythiophene backbone. In P3HT-TEMPO-25, charge transfer occurs both through the TEMPO radicals and along the conjugated backbone. When the radical loading is relatively low, the bulky TEMPO groups are spatially distant, which permits partial charge transfer through the conjugated backbone; this mixed behavior results in both the capacitive and the redox characters in **Figure 4-2b**.

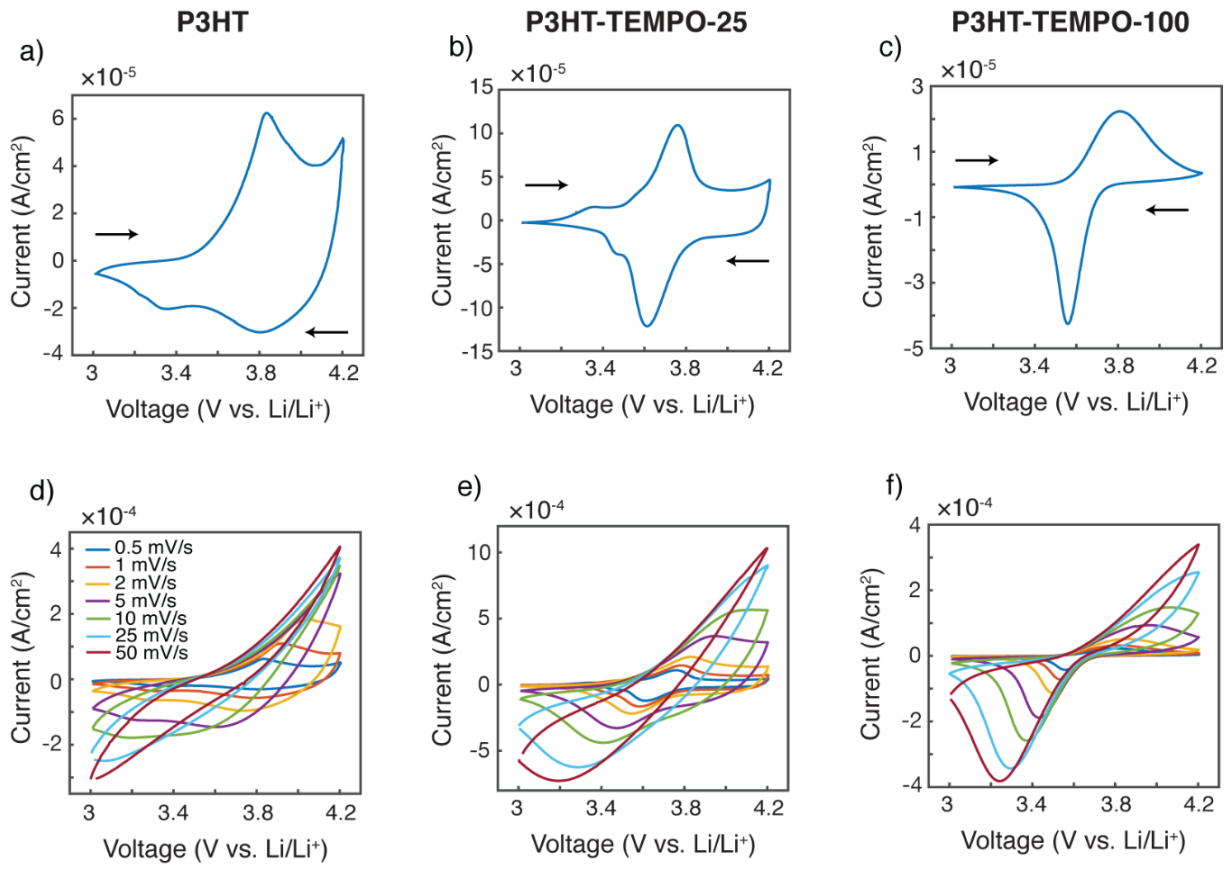

Figure 4-2. Cyclic voltammetry at 0.5 mV s^{-1} for a) P3HT, b) P3HT-TEMPO-25, and c) P3HT-TEMPO-100. Overlapped cyclic voltammograms of d) P3HT, e) P3HT-TEMPO-25, and f) P3HT-TEMPO-100 at scan rates of 0.5 to 50 mV s^{-1}. The working electrode was made by drop-casting the polymer solution on indium tin oxide (ITO) coated glass. The counter and reference electrodes were both lithium ribbons. The electrolyte was 0.5 M $LiCF_3SO_3$ in EC/DEC (3/7 by volume).

The relationship between peak current and scan rate was next inspected to further understand the redox mechanism. Only the cathodic scan was examined because the anodic scans were distorted at higher scan rates. The CV distortion might be due to limited ion diffusion in the relatively thick polymer films prepared from drop-casting. **Figure 4-3** shows the cathodic peak current *vs*. scan rate$^{1/2}$ (**Figure 4-3 a-c**) and *vs*. scan rate (**Figure 4-3 d-f**). Because P3HT does not show a clear reduction peak at higher scan rates, the cathodic current at 3.80 V was plotted

instead. The current response of P3HT shows a linear relationship with neither scan rate$^{1/2}$ nor scan rate, probably because of the distorted response even in the cathodic scans. The cathodic peak current values of P3HT-TEMPO-25 and P3HT-TEMPO-100 were linearly proportional to scan rate$^{1/2}$, except at the highest two scan rates (25 and 50 mV s^{-1}). This indicates that charge transfer in both CRPs is diffusion-controlled at lower scan rates, consistent with our previous observation in non-regioregular TEMPO bearing polythiophenes.[87]

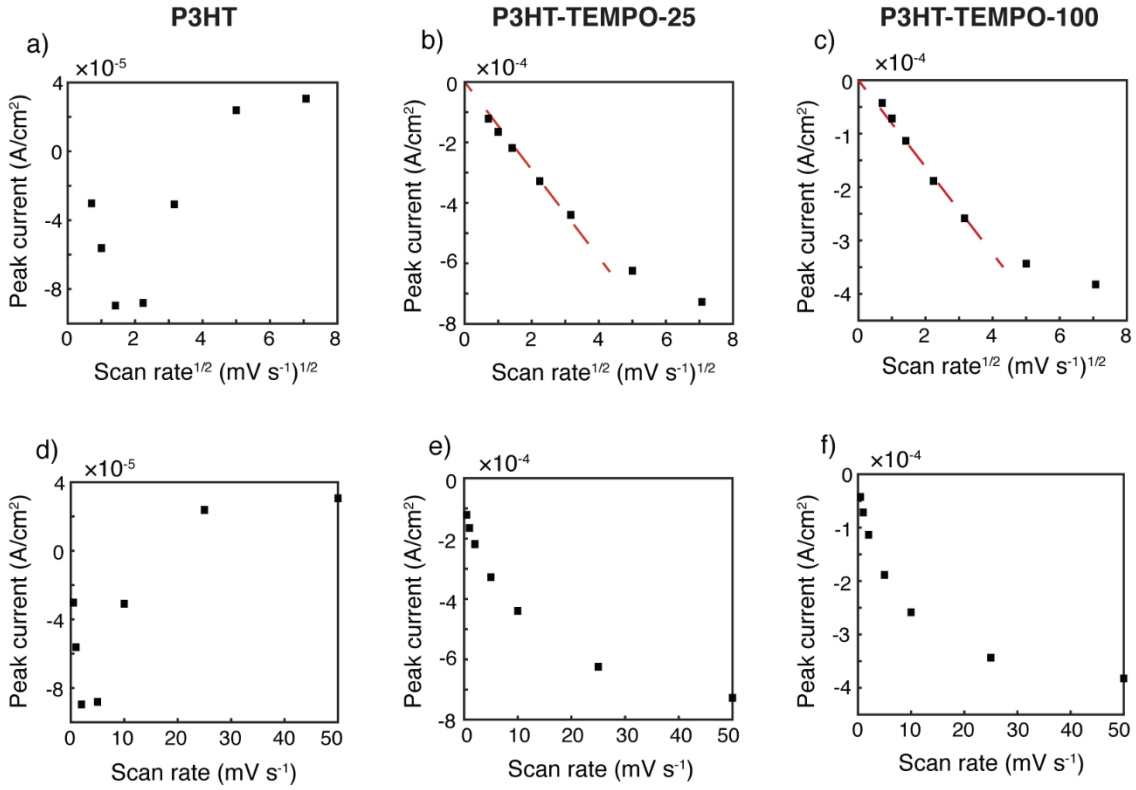

Figure 4-3. Peak current *vs*. scan rate1/2 for a) P3HT, b) P3HT-TEMPO-25, and c) P3HT-TEMPO-100 and *vs*. scan rate for d) P3HT, e) P3HT-TEMPO-25, and f) P3HT-TEMPO-100. Data are analyzed from cyclic voltammograms shown in Figure 4-2. Red dashed lines indicate linear regions.

4.4. Current Deconvolution

Cyclic voltammograms at 10 mV s^{-1} were further deconvoluted to estimate the faradaic *vs*. non-faradaic contributions to the total charge transfer for the three polymers following the method of Sathiya et al.[106] For this analysis, we utilized CVs from thin films obtained with EQCM-D (see below) to reduce diffusion limitations. Detailed current deconvolution to separate faradaic and non-faradaic current is described below.

The current response at a single voltage can be aexpressed by

$$\mathrm{i(V)} = a_1 v^{0.5} + a_2 v \qquad \text{(Equation 4-1)}$$

where i(V) is the current response at a given potential, v is scan rate, and a_1 and a_2 are constants. The faradaic current is expressed as $a_1 v^{0.5}$, and the non-faradaic portion is $a_2 v$.

By deviding $v^{0.5}$ on both sides, the above equation is re-arranged to

$$\frac{i(V)}{v^{0.5}} = a_1 + a_2 v^{0.5} \qquad \text{(Equation 4-2)}$$

The values of a_1 and a_2 can be determined by plotting $\frac{i(V)}{v^{0.5}}$ *vs*. $v^{0.5}$ and fitting with linear regression, where the slope is a_2 and the intercept is a_1.

Thus, the faradaic current ($a_1 v^{0.5}$) and non-faradaic current ($a_2 v$) were deconvoluted from the raw cyclic voltammogram.

Figure 4-4 below are a representation of the $\frac{i(V)}{v^{0.5}}$ *vs.* $v^{0.5}$. In the real calculation, our voltage increment was 0.02 V. Due to the discontinuity between low and high scan rates, we fit $\frac{i(V)}{v^{0.5}}$ *vs.* $v^{0.5}$ only for scan rates of 10–50 mV s^{-1}.

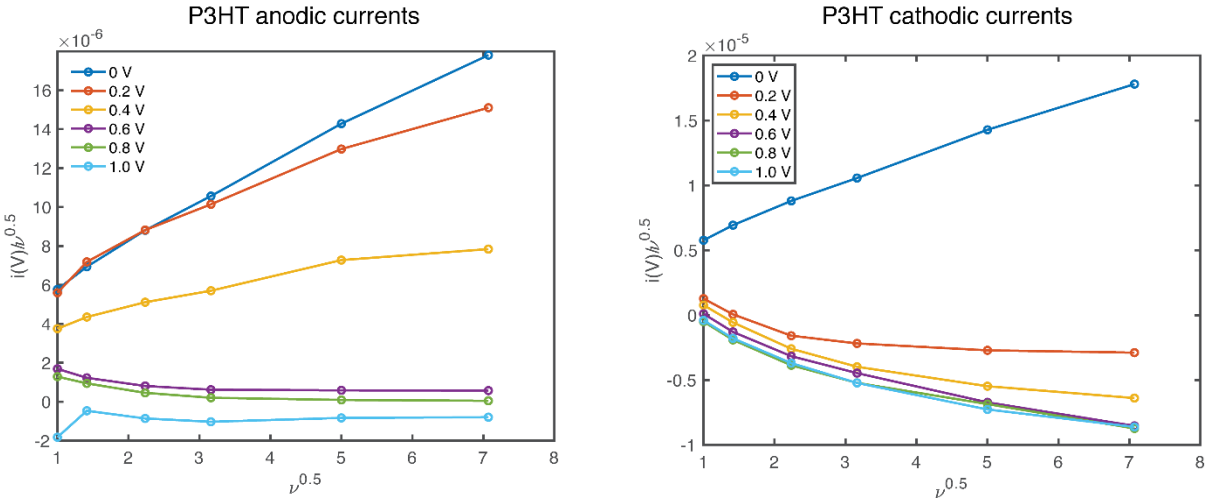

Figure 4-4. Example of deconvolution for the faradic and non-faradic current response.

It is clearly seen that the faradaic process was the major charge transfer mechanism for P3HT (**Figure 4-5a**). For P3HT-TEMPO-25, we were not able to reliably deconvolute the CVs, as any attempts at linear fits resulted in R^2 values lower than 0.8; this could be a result of internal charge transfer, but other methods are needed for such a claim. As for P3HT-TEMPO-100, the deconvolution was much better behaved (**Figure 4-5b**), in which a sharp non-faradaic peak associated with TEMPO competes with faradaic processes assigned to P3HT. In comparing P3HT and P3HT-TEMPO-100, the presence of the TEMPO radical causes the charge transfer to be dominated by the TEMPO group in its active potential window, leaving faradic processes to

occur at higher potentials. This difference could be ascribed to internal charge transfer as well as the rapid TEMPO redox kinetics. **Figure 4-6** displays the respective charge contributions, obtained from the integrated, deconvoluted cyclic voltammograms.

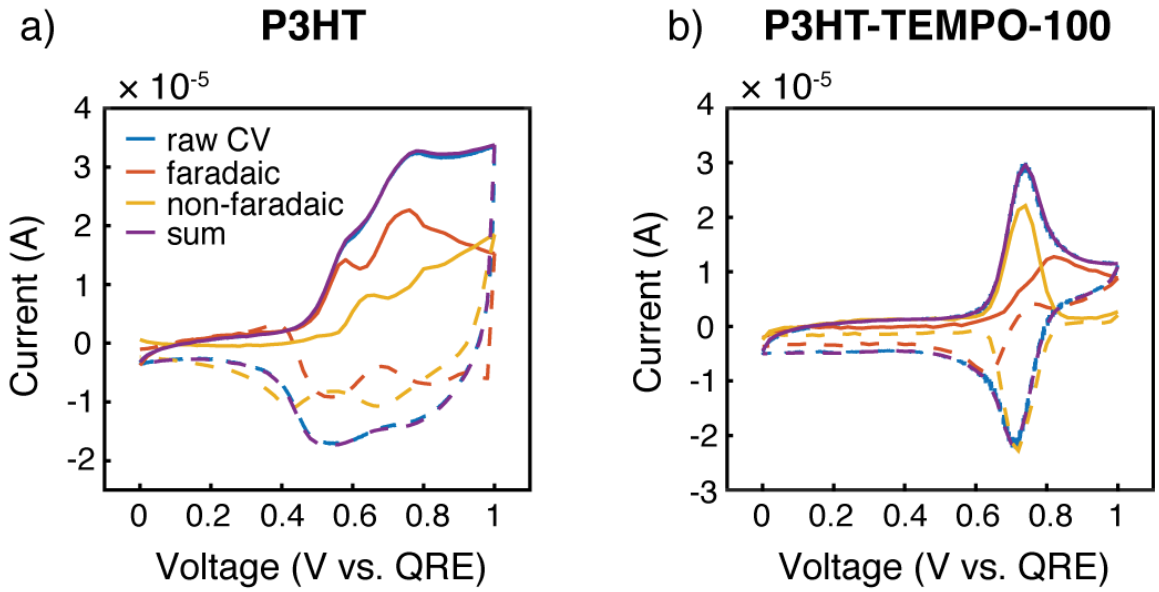

Figure 4-5. Cyclic voltammetry deconvolutions for a) P3HT and b) P3HT-TEMPO-100 at 10 mV s^{-1}. The anodic currents are solid lines, and the cathodic currents are dashed lines. The faradaic and non-faradaic contributions to the total current (blue) are red and yellow, respectively. The sum of calculated faradaic and non-faradaic contributions is purple. The measurements were conducted in an EQCM-D chamber, in which the working electrode was P3HT/P3HT-TEMPO-100-coated quartz crystal, the counter electrode was Pt plate, and the quasi-reference electrode was silver wire. The electrolyte was 0.5 M $LiCF_3SO_3$ in propylene carbonate.

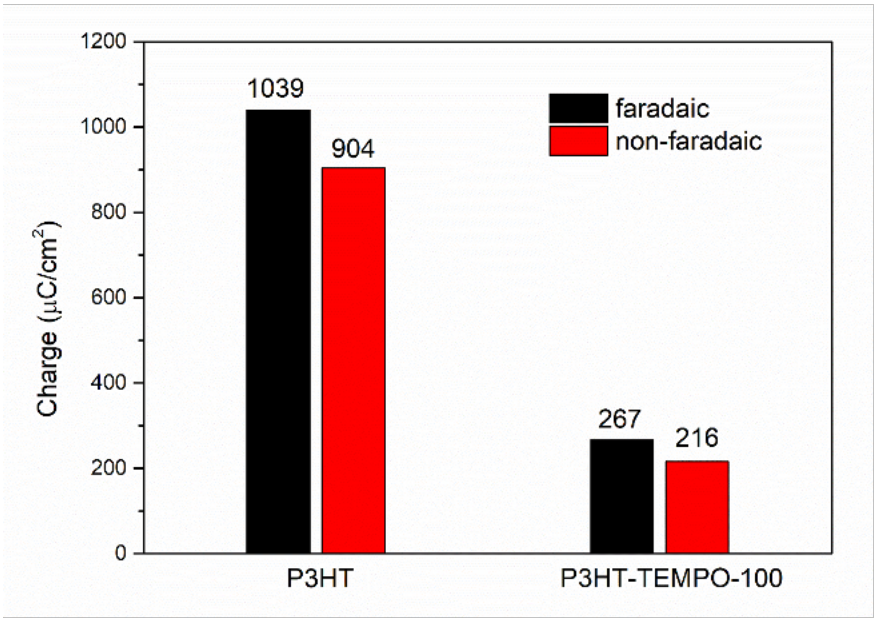

Figure 4-6. Faradaic *vs*. non-faradaic contributions to charge transfer for P3HT and P3HT-TEMPO-100 thin film electrodes.

4.5. Galvanostatic Charge-Discharge

Galvanostatic charge-discharge was next applied to examine each polymer's response to a constant current, **Figure 4-7**. P3HT exhibited a sloping voltage profile (**Figure 4-7a**), which is typical for conjugated polymers.[90] The minor plateau between 4.1 to 4.2 V is likely from slow charging under a low current density of 5 μA cm^{-2}. At current densities of 10 and 20 μA cm^{-2}, the plateau was not observed. P3HT-TEMPO-100 shows a similar charge-discharge profile consistent with homopolymer PTMA,[81] having a flat plateau from 3.6 to 3.7 V and little capacity contribution from voltages above and below the plateau (**Figure 4-7c**). Again, P3HT-TEMPO-25 exhibited mixed behavior, in which both a sloping discharge profile and plateau were observed (**Figure 4-7b**); this short plateau appeared between 3.6 and 3.8 V, and then the voltage increased gradually above 3.8 V. For P3HT-TEMPO-25, this mixed behavior shows that the low TEMPO

loading permits electron transfer through both the conjugated backbone and the radical sites. Also, it is notable that this voltage plateau is more obvious in the discharge profile than in the charge profile; this observation is consistent with the more distinct cathodic peaks in the cyclic voltammograms (**Figure 4-2e**).

The capacity values also vary with radical loading. P3HT shows the highest capacity under all current densities. Specifically, the areal discharge capacities of P3HT were 9.6, 8.8 and 7.8 μAh cm^{-2} at 5, 10 and 20 μA cm^{-2}, respectively (**Figure 4-7a**). Although bearing a second redox-active moiety, P3HT-TEMPO-100 yielded lower areal discharge capacities of 2.9, 2.6 and 2.4 μAh cm^{-2} at 5, 10 and 20 μA cm^{-2}, respectively (**Figure 4-7c**). On the other hand, P3HT-TEMPO-25 exhibited a moderate discharge capacity of 4.2 μAh cm^{-2} at 5 μA cm^{-2}, but its capacity drastically dropped to 1.6 and 0.4 μAh cm^{-2} at 10 and 20 μA cm^{-2}, respectively, having the lowest areal capacities among the three (**Figure 4-7b**). We note that the samples are thin and have low mass loadings (0.3-0.5 mg cm^{-2}), so capacity is best displayed using an areal basis. However, we also display specific capacity in **Figure 4-7** for comparison to the reader.

Interestingly, the trend in radical loading with capacity is counterintuitive. Specifically, the theoretical capacities for P3HT, P3HT-TEMPO-25, and P3HT-TEMPO-100 are 161.4, 160.9, and 159.5 mAh g^{-1} (assuming one electron transferred per P3HT unit and another one transferred per TEMPO unit). However, the obtained capacities, in order from lowest to highest, were P3HT-TEMPO-100 < P3HT-TEMPO-25 < P3HT, respectively. Electrochemical impedance spectroscopy of the three polymers also revealed a supporting trend, in which the charge transfer resistance at 4.0 V *vs*. Li/Li^+ was highest for P3HT-TEMPO-100 and lowest for P3HT, **Figure 4-8** and **Table 4-1.** This is explained by the phenomena of internal charge transfer between the loaded TEMPO and the conjugated backbone.[86, 87] The effect of radical loading on internal

transfer has not been examined before, and these results show that even with 25% TEMPO loading, internal transfer still occurs.

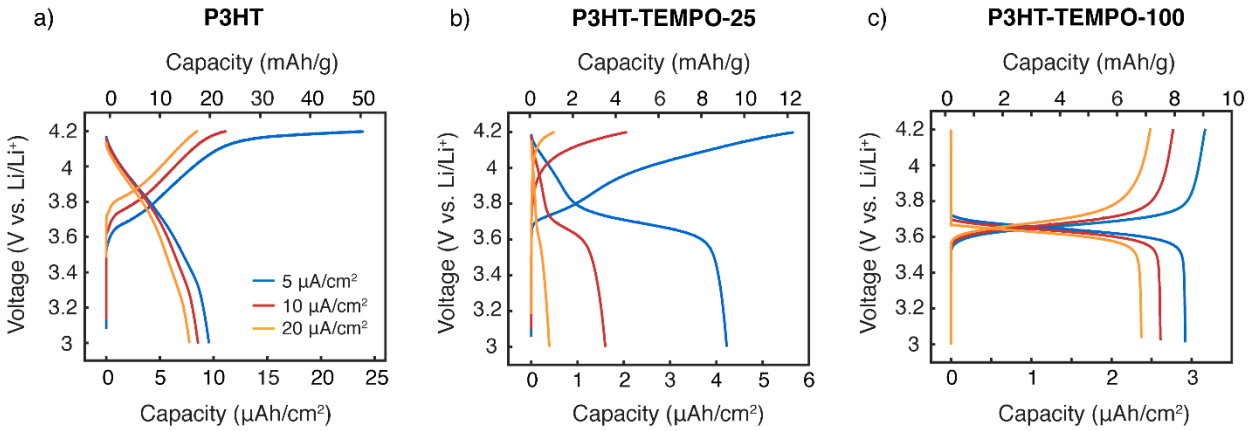

Figure 4-7. Charge-discharge profiles for a) P3HT, b) P3HT-TEMPO-25, and c) P3HT-TEMPO-100.

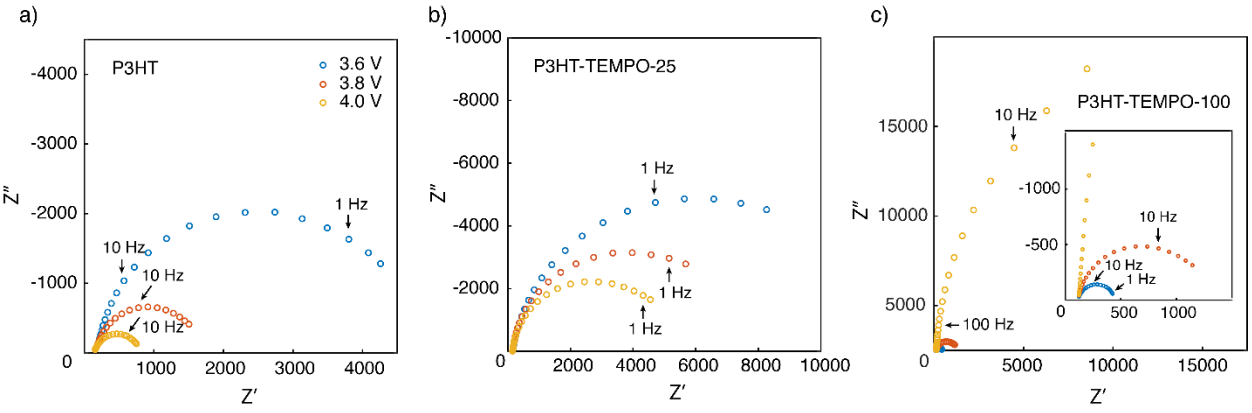

Figure 4-8. Electron impedance spectroscopy of a) P3HT, b) P3HT-TEMPO-25, and c) P3HT-TEMPO-100.

Table 4-1. Summary of EIS data.

	P3HT			P3HT-TEMPO-25			P3HT-TEMPO-100		
	3.6 V	3.8 V	4.0 V	3.6 V	3.8 V	4.0 V	3.6 V	3.8 V	4.0 V
R_s/Ω	164	153	142	152	153	153	114	120	121
R_{ct}/Ω	4,850	1,590	671	11,500	7,140	4,990	338	1,110	42,100
$Q_{dl}/10^{-5}.F\ s^{n-1}$	2.12	2.23	2.44	2.11	1.49	1.33	2.26	1.40	1.07
n_{dl}	0.89	0.87	0.86	0.90	0.93	0.94	0.88	0.93	0.96

4.6. Capacity Contribution Analysis

The capacity contributions from the nitroxide group and the polythiophene backbone were estimated by charging the polymers to various potential cutoffs from 3.5 to 4.2 V. **Figure 4-9 a-c** shows the calculated areal capacities at each cutoff voltage for P3HT, P3HT-TEMPO-25, and P3HT-TEMPO-100, respectively; **Figure 4-9d** shows the normalized charge capacity, which is the ratio of charging capacity at a particular cutoff voltage over the highest capacity among all tested voltages. In other words, the normalized charge capacity reflects the capacity contributions from each cutoff voltage to the "total" charging capacity.

The charging profile of P3HT increases with potential and the highest charging capacity is obtained at 4.2 V (**Figure 4-9a**). The capacity at 3.8 V is 12% of the total capacity. Further charging to 4 V leads to 68% of the "total" capacity. The voltage plateau from 4.1 to 4.2 V is again a result of long charging time from a small current density (5 $\mu A\ cm^{-2}$), and it contributes to 32% of the "total" capacity. The charging profile in P3HT is consistent with the charge discharge profile presented in **Figure 4-7a**. Thus, at a higher discharge current density, the capacity contribution above 4 V is reduced.

In P3HT-TEMPO-100, the highest capacity is obtained at 3.8 V, and this value is used as "total" capacity (**Figure 4-9c**). The plateau from 3.6–3.7 V dominates the charge transfer process and contributes to 84% of the total capacity. Similar capacity contributions are also reported in our previous study for non-regioregular TEMPO-bearing polythiophene.[11] Further charging from 3.7 to 4.2 V only accounts for 16% of the overall capacity. Note that the capacity at 4.2 V is less than that at 3.8 V. This is a result from internal charge transfer, which appears to be more severe in the P3HT-TEMPO-100 case. In P3HT-TEMPO-25, the charging curve shows a short plateau from 3.7 to 3.8 V, and above that the capacity increases with voltage (**Figure 4-9b**). This is consistent with the charging profile shown earlier in **Figure 4-7b**. Charging to 3.8 V and 4.0 V accounts for 14% and 54% of the total capacity, respectively.

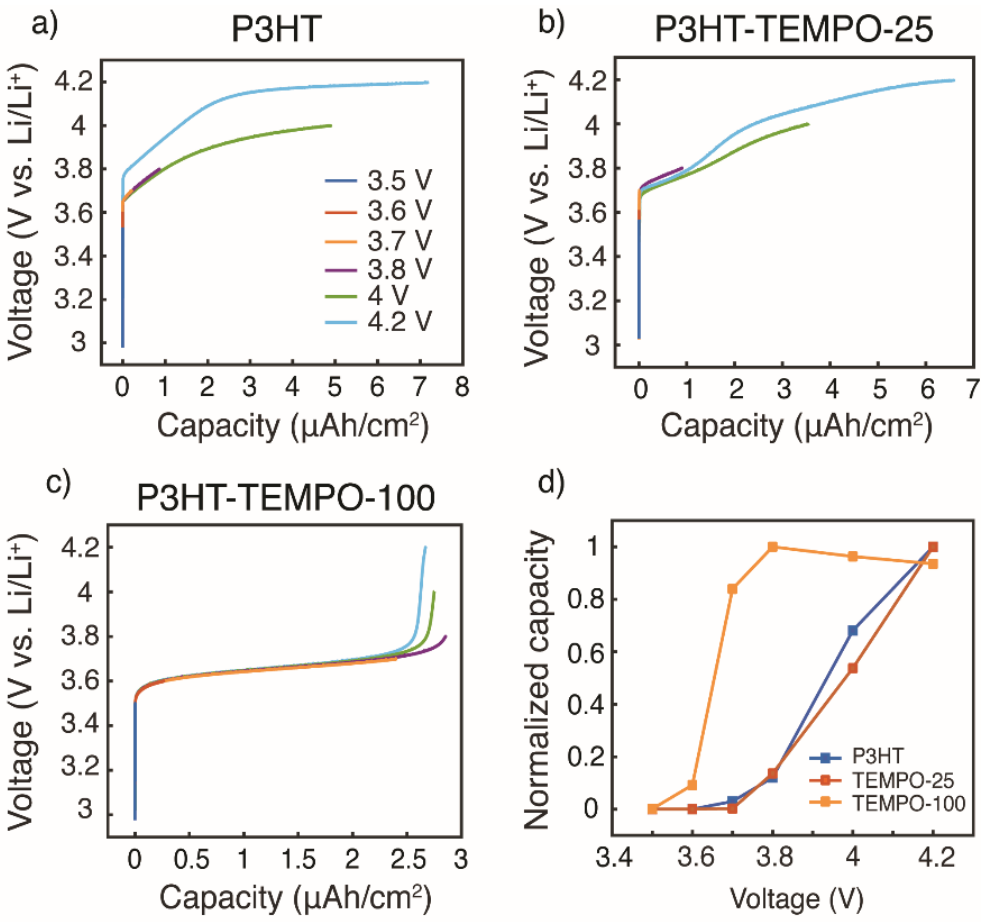

Figure 4-9. Galvanic charging to various potential cutoffs for a) P3HT-TEMPO-25, and b) P3HT-TEMPO-100. Normalized specific capacities of c) P3HT-TEMPO-25, and d) P3HT-TEMPO-100.

4.7. Open Circuit Potential

At last, open circuit potential (OCP) was monitored for 6 hours to investigate internal charge transfer (**Figure 4-10**). The three polymers were charged to 4.2 V, and the potential was held constant for 30 mins. After removing the bias, the OCP for P3HT gradually decayed to 3.93 V. On the contrary, the OCP for P3HT-TEMPO-100 sharply decreased to 3.8 V in the first 130 s and then the OCP stabilized to 3.67 V after 6 hours, consistent with the redox potential of

TEMPO radicals. P3HT-TEMPO-25 exhibited a gradual OCP decay similar to P3HT, but the OCP eventually stabilized to 3.8 V, which is the redox potential of polythiophene.

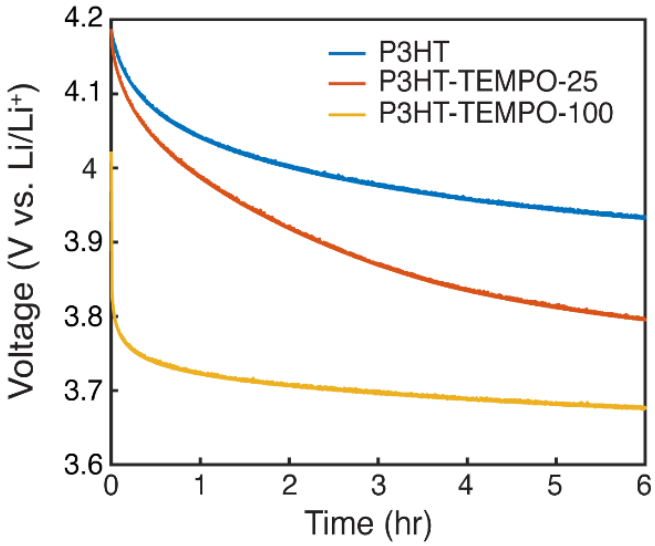

Figure 4-10. Open circuit potential monitoring for 6 hours.

The rapid OCP drop in P3HT-TEMPO-100 reflects internal charge transfer from the nitroxide radical to the conjugated polythiophene backbone. At 4.2 V, the majority of nitroxide radicals and polythiophene backbone are oxidized and doped. Since the oxidation reaction does not proceed to full completion, there remains a small amount of unoxidized TEMPO that is capable of transferring one electron to reduce the doped polythiophene backbone. Thus, following 6 h of relaxation, the OCP reflects the redox potential of TEMPO. A similar OCP response was also reported in our earlier studies.[87]

These results clearly show that regioregularity has a minor (if any) effect on electron transfer and internal charge transfer. The electrochemical responses of the regioregular P3HT-TEMPO-100 (93% regioregularity) were very similar to the non-regioregular TEMPO bearing P3HT[87] synthesized using electropolymerization, indicating that electron transfer in P3HT-TEMPO-100 still occurs via a hopping mechanism. Under a high radical loading, the regioregular backbone was twisted and distorted by the bulky TEMPO side chains, which impedes the formation of crystalline regions.[100] As a result, the polymers with high TEMPO loading remain amorphous regardless of the backbone regioregularity, and delocalized electron transfer through the conjugated backbone is prohibited. Both regioregular and non-regioregular P3HT-TEMPOs exhibited internal charge transfer, which will occur as long as the two redox-active moieties have different redox potentials because electron transfer from a species with lower redox potential to another species with higher redox potential is thermodynamically favorable. Thus, electrons transfer from TEMPO ($E_{1/2}$ = 3.6 V *vs*. Li/Li^+), having a lower redox potential, to the polythiophene backbone ($E_{1/2}$ = 3.8 V *vs*. Li/Li^+) after charging the CRP.

We conclude that the extent of internal charge transfer is dominated by the TEMPO loading, rather than the regioregularity. In support of this, we discuss radical coupling with respect to TEMPO loading and the OCP decay results displayed in **Figure 4-10**. Zhang et al. measured the radical concentration in the P3HT-TEMPO-25 and P3HT-TEMPO-100 using electron paramagnetic resonance (EPR).[100] P3HT-TEMPO-25 showed a hyperfine-induced triplet similar to TEMPO small molecules, indicating that the loaded TEMPO radicals are scattered through the polymer chain and local radical concentration is rather low.[100] On the contrary, P3HT-TEMPO-100 showed a broad EPR peak resulting from spin-spin interactions between closely installed TEMPO radicals.[100] The scattered *vs*. dense loading for P3HT-

TEMPO-25 *vs*. P3HT-TEMPO-100 manifests as differences in the decay of the OCP after charging and equilibration to 4.2 V. The sharp potential decay is not observed for P3HT-TEMPO-25, because only a small amount of the polythiophene is reduced by unoxidized TEMPO radicals in P3HT-TEMPO-25, and the majority of the polythiophene remains in the doped state. As a result, the OCP decayed faster than that for P3HT, but the OCP still stabilized near the redox potential of polythiophene (3.8 V), indicating that there was less internal charge transfer. Thus, internal charge transfer in P3HT-TEMPO-25 was limited by the low concentration of un-oxidized TEMPO units. In contrast, P3HT-TEMPO-100 exhibited sharp OCP decay and stabilization to the redox potential of the TEMPO units. Altogether, the extent of internal charge transfer is balanced by which redox units are majority-minority components.

4.8. The Doping Mechanism of P3HT-TEMPO-100

At last, we conducted EQCM-D to examine the doping mechanism in the CRP to compare with prior findings for homopolymer PTMA.[32] **Figure 4-11** shows the raw EQCM-D data collected during cyclic voltammetry for P3HT-TEMPO-100. During oxidation, the TEMPO radical was oxidized to an oxoammonium cation. To maintain charge neutrality, anions in the electrolyte (in this case, $CF_3SO_3^-$) dope the created oxoammonium cation. In consideration of the polythiophene backbone, doping may also occur, also accompanying the uptake of a $CF_3SO_3^-$ anion. The doping process is reflected by a decrease in frequency and an increase in dissipation, which corresponds to an increase in mass increase and electrode softening, respectively. During reduction, the polymer electrode was reduced and de-doped, accordingly, the mass decrease and electrode stiffening were reflected by the reverse trend in frequency and dissipation. The step change observed for PTMA-TEMPO-100 is consistent with the EQCM-D response of

homopolymer PTMA. [32] This result further confirms that charge transfer in P3HT-TEMPO-100 is dominated by the hopping mechanism associated with the TEMPO unit.

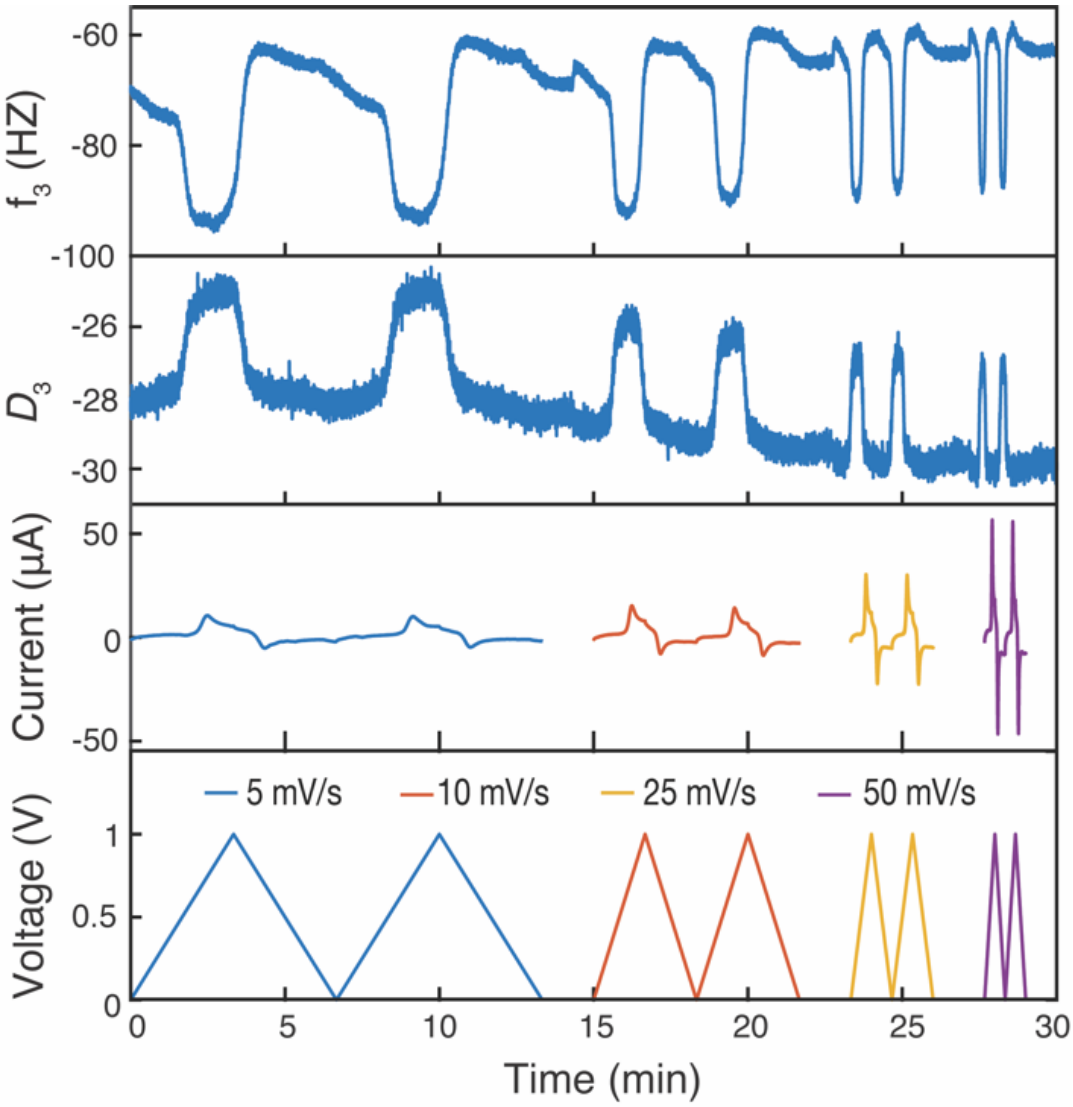

Figure 4-11. Frequency (f_3) and dissipation (D_3) responses of the third overtone from EQCM-D during cyclic voltammetry for P3HT-TEMPO-100. Two cycles were performed at each indicated scan rate, followed by equilibration in the liquid electrolyte for 100 s. The working electrode was P3HT-TEMPO-100-coated quartz crystal. The counter and reference electrode were Pt plate and silver wire, respectively. The electrolyte was 0.5 M $LiCF_3SO_3$ in propylene carbonate.

To gain more insight into the doping mechanism, we examined the shape of the cyclic voltammogram and calculated the mass change with the cumulative charge transfer (**Figure 4-12**). In our previous report on homopolymer PTMA, we showed that two doping processes exist – doping by Li-ion expulsion and anion uptake.[32] The two processes corresponded to two cyclic voltammetry peaks, in which doping by Li-ion expulsion occurred at a lower potential. However, **Figure 4-12a** only shows a single peak, indicating that one doping mechanism is dominating over the other, namely anion uptake. Using viscoelastic modeling of the raw data, the change in electrode mass was overlaid with the corresponding cyclic voltammogram at 25 mV s^{-1}, **Figure 4-12b**. The mass change coincided well with the redox peak, confirming significant mass changes affiliated with the TEMPO redox process.

Finally, the change in mass was plotted against the integrated current, taken from the oxidation scan in the voltage range of 0.595 to 1.0 V *vs*. QRE, to examine ion transport coinciding with those regions in which internal charge transfer had been observed, **Figure 4-12c**. The mass increased linearly with the charge transferred, and the slope of this linear relationship ($\Delta m/Q$) gave a measure of the doping process. Assuming that each TEMPO radical is doped by an anion from the bulk electrolyte (because it appears to be the dominating species), the theoretical $\Delta m/Q$ value is simply the ratio of the molecular weight of the balancing anion (in this case, $CF_3SO_3^-$) over Faraday's constant, yielding 1.55 mg C^{-1}. In **Figure 4-12c,** the slope of Δm *vs*. Q was 2.65 mg C^{-1}, which means that either 1) doping occurs mainly via anion uptake with solvent participation or 2) the electrolyte may transfer in ion pairs with or without solvent. We speculate the former process is dominating because individual anions are likely easier to transport than ion pairs or clusters. In that case, we calculate by a mass balance that 1 propylene

carbonate molecule accompanies each triflate anion during the oxidation process at this specific scan rate.

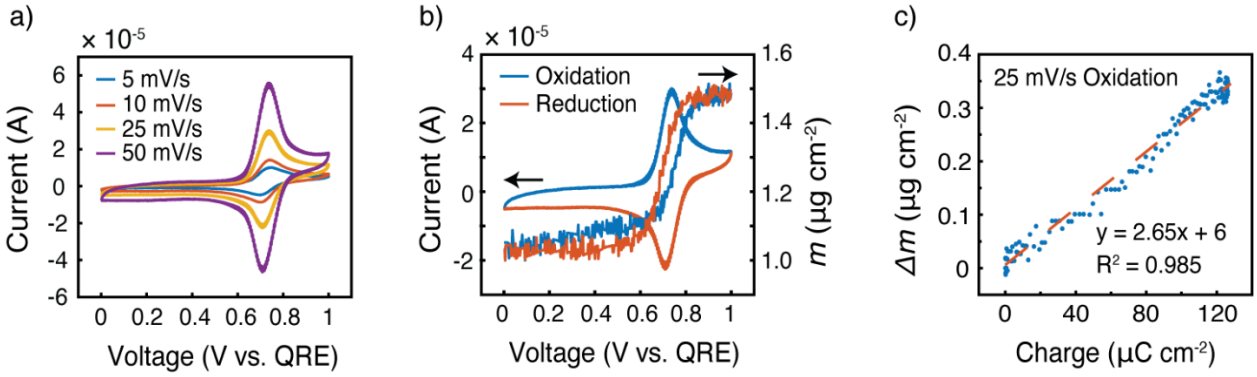

Figure 4-12. a) Cyclic voltammetry of P3HT-TEMPO-100, b) cyclic voltammetry of P3HT-TEMPO-100 at 25 mV s^{-1} overlapped with electrode mass, and c) change in electrode mass *vs*. charge passed during oxidation at 25 mV s^{-1} via EQCM-D from 0.595 to 1.0 V *vs*. QRE.

4.9. Conclusion

This work quantified internal charge transfer in CRPs consisting of polythiophene backbones and TEMPO side groups. This was accomplished by using CRPs of varying TEMPO loadings (0, 25, 100%). P3HT-TEMPO-100's behavior was dominated by the TEMPO radical, due to internal transfer. Specifically, this was distinguished by the mixed faradaic and non-faradic contributions from the conjugated backbone and radical side groups. P3HT-TEMP-25 exhibited features of both the conjugated backbone and the TEMPO radical, suggesting that radical loading strongly influences the electron transfer behavior. From comparison, we conclude that the extent of internal charge transfer depends on the radical loading, similar to the consideration of limiting and excess "reactants", as exhibited by the final OCPs during relaxation

monitoring. Finally, coupled electron-ion transport was observed in situ for the first time for P3HT-TEMPO-100; it was suggested that ~1 propylene carbonate molecule accompanies a triflate ion upon each doping event of the CRP during cyclic voltammetry at 25 mV s^{-1}.

All together, these findings confirm the underlying reasons for these CRP's generally low conductivity and capacity. On the other hand, these findings suggest that CRPs such as these might be useful as voltage regulating materials, in which the CRP might mitigate voltage excursions through internal charge transfer. For future design, the trade-off between radical loading and electronic conductivity need to be balanced. Novel molecular design that decouples the radical unit and the charge conducting pathway might be desirable to reach a high specific capacity. In addition, the direction of internal charge transfer between the two redox moieties need to be carefully considered.

5. CONCLUSIONS

5.1. Conclusions

In conclusion, this dissertation focuses on organic radical polymers research in two aspects – electron-ion transfer during redox reactions and their applications as battery electrodes. The former aimed to understand the fundamental reaction mechanism that governs the electrochemical behavior of the organic radical polymers, while the latter tackled practical electrode dissolution issue by a synthetic approach. Three electrochemical systems were investigated: homogeneous PTMA in contact with varied lithium salts in the electrolyte, crosslinked PTMA electrode with varied crosslinking density, and conjugated radical polymers with varied radical loading. In particular, electrochemical quartz crystal microbalance with dissipation (EQCM-D) was applied extensively to characterize the doping mechanism of the organic radical polymers during redox reactions. The fundamental knowledge of these reaction systems provides essential guidelines and considerations for the future design of polymer electrodes.

For the first time, in-situ ion transport and doping in organic radical polymers were observed quantitatively via EQCM-D. In addition, a dual doping process – doping by lithium expulsion and anion uptake was revealed. In the first case, an anion imbibed in the swollen PTMA doped the oxoammonium cation, resulting in the expulsion of a lithium cation into the bulk electrolyte. In the second case, an anion diffused from the bulk electrolyte into the polymer electrode doped either the oxoammonium cation or the lithium cation. The relative extent of the two doping mechanisms was directly related to solvent-dopant, polymer-solvent, and polymer-dopant interactions, which were affected by anion type, electrolyte concentration, and

experimental timescale. The dual doping mechanism and this EQCM-D methodology could apply to other electrochemical systems in which the non-conjugated redox-active polymers interact with the electrolytes, such as electrochromics, sensors, and energy storage (i.e., batteries).

These results provide insight into the working principle of non-conjugated organic radical polymers and direct the future electrolyte design. The relative doping contributions of the lithium expulsion and anion uptake will largely depend on the choice of solvents and salts, which results from variations in ion dissociation and mobility in the electrolyte. It is desirable to have some degree of lithium expulsion because it occurs at a lower redox potential, and sufficient swelling of the polymer and salts facilitates its rapid redox reaction. On the other hand, since anion uptake dominates under fast charging, the electrolyte that shows less solvent transport with the dopant ions is favorable, which could possibly reduce the electrode volumetric change upon doping. Thus, future mass transfer studies are needed to further quantify the doping mechanism under various electrolyte compositions, such as different electrolyte concentrations, solvent types, anion types, and electrolyte additives.

In chapter 3, a one-step post-synthetic, carbon-compatible crosslinking method was developed to efficiently crosslink PTMA and prevent its dissolution. Glycidyl methacrylate was used as a crosslinker and the amount added into the monomer was varied to find an optimum crosslinking density. The as-synthesized PTMA-*co*-GMA copolymers were soluble in organic solvents, which allowed easy solution-processing of the copolymer electrodes. Crosslinking was carried out above the glass transition temperature of the copolymers under the presence of carbon additives. It was determined that 3 mol% GMA crosslinker led to the best capacity retention (99.6%) and that 1 mol% GMA crosslinker led to the highest capacity (104 mAh g^{-1}). In

addition, the doping behavior of the crosslinked electrodes was characterized in situ by EQCM-D and both lithium expulsion and anion uptake were observed. Crosslinking density (or free volume) was identified as a new factor that affected the relative dominance of the two doping modes in crosslinked polymer electrodes.

This study points to the importance of preserving radical content during synthesis and crosslinking. The synthesis and oxidation method should be modified to maximize radical loading, and the crosslinking process should avoid eliminating the redox-active radical sites. In the future, a post-crosslinking method that allows easy solution processing but, at the same time, produces composite electrodes with high capacity and reasonable thickness (>10 μm) is desired. This will require a balance between crosslinking density, radical concentration, and electron transport to combat the issue of active material dissolution.

In chapter 4, the electron and ion transfer were investigated in conjugated radical polymers (CRPs) consisting of polythiophene backbones and TEMPO side groups. Specifically, the extent of internal charge transfer between the free electron in the pendant radical and delocalized π electrons in the conjugated backbone was quantified by using CRPs with varied TEMPO loadings (0, 25, 100%, named as P3HT, P3HT-TEMPO-25 and P3HT-TEMPO-100, respectively). Results showed that the electron transfer shifted from delocalized electron transport (P3HT) to localized electron hopping under higher radical loading (P3HT-TEMPO-100), because the bulky TEMPO side groups impeded inter- and intra- molecular charge transfer through the conjugated backbone. The extent of internal charge transfer was proportional to the radical loading. Finally, coupled electron-ion transport was observed in situ for the first time for P3HT-TEMPO-100; it was suggested that approximately 1 propylene carbonate molecule

accompanied a triflate ion upon each doping event of the CRP during cyclic voltammetry at 25 mV s^{-1}.

Altogether, these findings confirm the underlying reasons for CRP's generally low conductivity and capacity. For future design, the trade-off between radical loading and electronic conductivity should be balanced. Since internal charge transfer will exist when the potentials of the redox moieties are different, it might be necessary to decouple the radical unit and the charge conductivity pathway through novel molecular design or materials processing.

REFERENCES

1. Song, Z.; Zhou, H., Towards sustainable and versatile energy storage devices: an overview of organic electrode materials. *Energy & Environmental Science* **2013,** *6* (8), 2280-2301.

2. Janoschka, T.; Teichler, A.; Krieg, A.; Hager, M. D.; Schubert, U. S., Polymerization of free secondary amine bearing monomers by RAFT polymerization and other controlled radical techniques. *Journal of Polymer Science Part A: Polymer Chemistry* **2012,** *50* (7), 1394-1407.

3. Nishide, H.; Suga, T., Organic radical battery. *Electrochemical Society Interface* **2005,** *14* (4), 32-36.

4. Suga, T.; Pu, Y.-J.; Oyaizu, K.; Nishide, H., Electron-transfer kinetics of nitroxide radicals as an eectrode-active material. *Bulletin of the Chemical Society of Japan* **2004,** *77* (12), 2203-2204.

5. Nevers, D. R.; Brushett, F. R.; Wheeler, D. R., Engineering radical polymer electrodes for electrochemical energy storage. *Journal of Power Sources* **2017,** *352*, 226-244.

6. Tarascon, J. M.; Armand, M., Issues and challenges facing rechargeable lithium batteries. *Nature* **2001,** *414*, 359-367.

7. Arico, A. S.; Bruce, P.; Scrosati, B.; Tarascon, J.-M.; Van Schalkwijk, W., Nanostructured materials for advanced energy conversion and storage devices. *Nature Materials* **2005,** *4* (5), 366-377.

8. Janoschka, T.; Hager, M. D.; Schubert, U. S., Powering up the future: radical polymers for battery applications. *Advanced Materials* **2012,** *24* (48), 6397-409.

9. Suga, T.; Pu, Y.-J.; Kasatori, S.; Nishide, H., Cathode- and anode-active poly(nitroxylstyrene)s for rechargeable batteries: p- and n-type redox switching via substituent effects. *Macromolecules* **2007,** *40* (9), 3167-3173.

10. Nakahara, K.; Iwasa, S.; Satoh, M.; Morioka, Y.; Iriyama, J.; Suguro, M.; Hasegawa, E., Rechargeable batteries with organic radical cathodes. *Chemical Physics Letters* **2002,** *359* (5-6), 351-354.

11. Mukherjee, S.; Boudouris, B. W., *Organic Radical Polymers: New Avenues in Organic Electronics*. Springer: 2017.

12. Hauffman, G.; Rolland, J.; Bourgeois, J. P.; Vlad, A.; Gohy, J. F., Synthesis of nitroxide-containing block copolymers for the formation of organic cathodes. *Journal of Polymer Science Part A: Polymer Chemistry* **2013,** *51* (1), 101-108.

13. Rostro, L.; Baradwaj, A. G.; Boudouris, B. W., Controlled radical polymerization and quantification of solid state electrical conductivities of macromolecules bearing pendant stable radical groups. *ACS Applied Materials & Interfaces* **2013,** *5* (20), 9896-9901.

14. Suga, T.; Konishi, H.; Nishide, H., Photocrosslinked nitroxide polymer cathode-active materials for application in an organic-based paper battery. *Chemical Communications* **2007,** (17), 1730-1732.

15. Iwasa, S.; Nishi, T.; Sato, H.; Nakamura, S., Flexibility and high-rate discharge properties of organic radical batteries with gel-state electrodes. *Journal of The Electrochemical Society* **2017,** *164* (4), A884-A888.

16. Sukegawa, T.; Omata, H.; Masuko, I.; Oyaizu, K.; Nishide, H., Anionic polymerization of 4-methacryloyloxy-TEMPO using an MMA-capped initiator. *ACS Macro Letters* **2014,** *3* (3), 240-243.

17. Bugnon, L.; Morton, C. J.; Novak, P.; Vetter, J.; Nesvadba, P., Synthesis of poly (4-methacryloyloxy-TEMPO) via group-transfer polymerization and its evaluation in organic radical battery. *Chemistry of Materials* **2007,** *19* (11), 2910-2914.

18. Oyaizu, K.; Kawamoto, T.; Suga, T.; Nishide, H., Synthesis and charge transport properties of redox-active nitroxide polyethers with large site density. *Macromolecules* **2010,** *43* (24), 10382-10389.

19. Vlad, A.; Rolland, J.; Hauffman, G.; Ernould, B.; Gohy, J. F., Melt-polymerization of TEMPO methacrylates with nano carbons enables superior battery materials. *ChemSusChem* **2015,** *8* (10), 1692-1696.

20. Kurosaki, T.; Lee, K. W.; Okawara, M., Polymers having stable radicals. I. Synthesis of nitroxyl polymers from 4-methacryloyl derivatives of 2, 2, 6, 6-tetramethylpiperidine. *Journal of Polymer Science Part A-1: Polymer Chemistry* **1972,** *10* (11), 3295-3310.

21. Hauffman, G.; Vlad, A.; Janoschka, T.; Schubert, U.; Gohy, J.-F., Nanostructured organic radical cathodes from self-assembled nitroxide-containing block copolymer thin films. *Journal of Materials Chemistry A* **2015,** *3* (38), 19575-19581.

22. Rostro, L.; Baradwaj, A. G.; Muller, A. R.; Laster, J. S.; Boudouris, B. W., Synthesis and thin-film self-assembly of radical-containing diblock copolymers. *MRS Communications* **2015,** *5* (2), 257-263.

23. Liedel, C.; Moehle, A.; Fuchs, G. D.; Ober, C. K., Block copolymers with stable radical and fluorinated groups by ATRP. *MRS Communications* **2015,** *5* (3), 441-446.

24. Nishide, H.; Iwasa, S.; Pu, Y.-J.; Suga, T.; Nakahara, K.; Satoh, M., Organic radical battery: nitroxide polymers as a cathode-active material. *Electrochimica Acta* **2004,** *50* (2-3), 827-831.

25. Karrer, F. E., Polymere 2,2,6,6,-Tetraalkylpiperidin-derivate, 1.tetra-und pentaalkylpiperidin-derivate von polyacryl-und polymethacrylestern, polyacryl-und polymethacrylamiden. *Die Makromolekulare Chemie: Macromolecular Chemistry and Physics* **1980,** *181* (3), 595-633.

26. Kemper, T. W.; Larsen, R. E.; Gennett, T., Relationship between molecular structure and electron transfer in a polymeric nitroxyl-radical energy storage material. *The Journal of Physical Chemistry C* **2014,** *118* (31), 17213-17220.

27. Kemper, T. W.; Larsen, R. E.; Gennett, T., Density of states and the role of energetic disorder in charge transport in an organic radical polymer in the solid state. *The Journal of Physical Chemistry C* **2015,** *119* (37), 21369-21375.

28. Kemper, T. W.; Gennett, T.; Larsen, R. E., Molecular Dynamics Simulation Study of Solvent and State of Charge Effects on Solid-Phase Structure and Counterion Binding in a Nitroxide Radical Containing Polymer Energy Storage Material. *The Journal of Physical Chemistry C* **2016,** *120* (45), 25639-25646.

29. Joo, Y.; Agarkar, V.; Sung, S. H.; Savoie, B. M.; Boudouris, B. W., A nonconjugated radical polymer glass with high electrical conductivity. *Science* **2018,** *359* (6382), 1391.

30. Allgaier, J.; Finkelmann, H., Anionic polymerization of 4-methacryloyloxy-2,2,6,6-tetramethylpiperidin-1-oxyl and the magnetic properties of the polymer. *Die Makromolekulare Chemie, Rapid Communications* **1993,** *14* (5), 267-271.

31. Sato, K.; Ichinoi, R.; Mizukami, R.; Serikawa, T.; Sasaki, Y.; Lutkenhaus, J.; Nishide, H.; Oyaizu, K., Diffusion-cooperative model for charge transport by redox-active nonconjugated polymers. *Journal of the American Chemical Society* **2018,** *140* (3), 1049-1056.

32. Wang, S.; Li, F.; Easley, A. D.; Lutkenhaus, J. L., Real-time insight into the doping mechanism of redox-active organic radical polymers. *Nature Materials* **2019,** *18* (1), 69-75.

33. Yang, Z.; Dixon, M. C.; Erck, R. A.; Trahey, L., Quantification of the mass and viscoelasticity of interfacial films on tin anodes using EQCM-D. *ACS Applied Materials & Interfaces* **2015,** *7* (48), 26585-26594.

34. Levi, M. D.; Levy, N.; Sigalov, S.; Salitra, G.; Aurbach, D.; Maier, J., Electrochemical quartz crystal microbalance (EQCM) studies of ions and solvents insertion into highly porous activated carbons. *Journal of the American Chemical Society* **2010,** *132* (38), 13220-13222.

35. Tsai, W.-Y.; Taberna, P.-L.; Simon, P., Electrochemical quartz crystal microbalance (EQCM) study of ion dynamics in nanoporous carbons. *Journal of the American Chemical Society* **2014,** *136* (24), 8722-8728.

36. Oyama, N.; Ohsaka, T., Coupling between electron and mass transfer kinetics in electroactive polymer films — An application of the in situ quartz crystal electrode. *Progress in polymer science* **1995,** *20* (5), 761-818.

37. Sano, N.; Tomita, W.; Hara, S.; Min, C.-M.; Lee, J.-S.; Oyaizu, K.; Nishide, H., Polyviologen hydrogel with high-rate capability for anodes toward an aqueous electrolyte-type and organic-based rechargeable device. *ACS Applied Materials & Interfaces* **2013,** *5* (4), 1355-1361.

38. Daifuku, H.; Kawagoe, T.; Matsunaga, T.; Yamamoto, N.; Ohsaka, T.; Oyama, N., Quartz crystal microbalance study on redox reaction mechanism of polyaniline. *Synthetic metals* **1991,** *43* (1-2), 2897-2900.

39. Mizunuma, M.; Ohsaka, T.; Miyamoto, H.; Oyama, N., Investigation of ion and solvent transport accompanying redox reactions of polyvinylferrocene films using an in situ electrochemical quartz crystal microbalance technique. *Bulletin of the Chemical Society of Japan* **1991,** *64* (10), 2887-2893.

40. McCubbin, G. A.; Praporski, S.; Piantavigna, S.; Knappe, D.; Hoffmann, R.; Bowie, J. H.; Separovic, F.; Martin, L. L., QCM-D fingerprinting of membrane-active peptides. *European Biophysics Journal* **2011,** *40* (4), 437-446.

41. Saubrey, G., The use of quartz crystal oscillators for weighing thin layers and for microweighing applications. *Zeitschrift für Physik.* **1959,** *155*, 206-222.

42. Rodahl, M.; Höök, F.; Krozer, A.; Brzezinski, P.; Kasemo, B., Quartz crystal microbalance setup for frequency and Q‐factor measurements in gaseous and liquid environments. *Review of Scientific Instruments* **1995,** *66* (7), 3924-3930.

43. Dixon, M. C., Quartz crystal microbalance with dissipation monitoring: enabling real-time characterization of biological materials and their interactions. *Journal of Biomolecular Techniques: JBT* **2008,** *19* (3), 151-158.

44. Rodahl, M.; Höök, F.; Fredriksson, C.; Keller, C. A.; Krozer, A.; Brzezinski, P.; Voinova, M.; Kasemo, B., Simultaneous frequency and dissipation factor QCM measurements of biomolecular adsorption and cell adhesion. *Faraday Discussions* **1997,** *107*, 229-246.

45. Oyaizu, K.; Nishide, H., Radical polymers for organic electronic devices: a radical departure from conjugated polymers? *Advanced Materials* **2009,** *21* (22), 2339-2344.

46. Oyaizu, K.; Ando, Y.; Konishi, H.; Nishide, H., Nernstian adsorbate-like bulk layer of organic radical polymers for high-density charge storage purposes. *Journal of the American Chemical Society* **2008,** *130* (44), 14459-14461.

47. Nakahara, K.; Oyaizu, K.; Nishide, H., Electrolyte anion-assisted charge transportation in poly (oxoammonium cation/nitroxyl radical) redox gels. *Journal of Materials Chemistry* **2012,** *22* (27), 13669-13673.

48. Rostro, L.; Wong, S. H.; Boudouris, B. W., Solid state electrical conductivity of radical polymers as a function of pendant group oxidation state. *Macromolecules* **2014,** *47* (11), 3713-3719.

49. Karlsson, C.; Suga, T.; Nishide, H., Quantifying TEMPO redox polymer charge transport toward the organic radical battery. *ACS Applied Materials & Interfaces* **2017,** *9* (12), 10692-10698.

50. Joo, Y.; Agarkar, V.; Sung, S. H.; Savoie, B. M.; Boudouris, B. W., A nonconjugated radical polymer glass with high electrical conductivity. *Science* **2018,** *359* (6382), 1391-1395.

51. Zhang, Y.; Park, A.; Cintora, A.; McMillan, S. R.; Harmon, N. J.; Moehle, A.; Flatté, M. E.; Fuchs, G. D.; Ober, C. K., Impact of the synthesis method on the solid-state charge transport of radical polymers. *Journal of Materials Chemistry C* **2018,** *6* (1), 111-118.

52. Voinova, M. V.; Rodahl, M.; Jonson, M.; Kasemo, B., Viscoelastic acoustic response of layered polymer films at fluid-solid interfaces: continuum mechanics approach. *Physica Scripta* **1999,** *59* (5), 391.

53. He, J.; Mukherjee, S.; Zhu, X.; You, L.; Boudouris, B. W.; Mei, J., A highly transparent crosslinkable radical copolymer thin film as the ion storage layer in organic electrochromic devices. *ACS Applied Materials & Interfaces* **2018**.

54. Gagne, R. R.; Koval, C. A.; Lisensky, G. C., Ferrocene as an internal standard for electrochemical measurements. *Inorganic Chemistry* **1980,** *19* (9), 2854-2855.

55. Bard, A. J.; Faulkner, L. R.; Leddy, J.; Zoski, C. G., *Electrochemical methods: fundamentals and applications*. Wiley New York: 1980; Vol. 2.

56. Tokue, H.; Murata, T.; Agatsuma, H.; Nishide, H.; Oyaizu, K., Charge-discharge with rocking-chair-type Li^+ migration characteristics in a zwitterionic radical copolymer composed of tempo and trifluoromethanesulfonylimide with carbonate electrolytes for a high-rate Li-ion battery. *Macromolecules* **2017,** *50* (5), 1950-1958.

57. Mike, J. F.; Shao, L.; Jeon, J.-W.; Lutkenhaus, J. L., Charge storage in decyl-and 3,6,9-trioxadecyl-substituted poly(dithieno[3,2-b:2,3-d]pyrrole) electrodes. *Macromolecules* **2013,** *47* (1), 79-88.

58. Jeon, J.-W.; Ma, Y.; Mike, J. F.; Shao, L.; Balbuena, P. B.; Lutkenhaus, J. L., Oxidatively stable polyaniline: polyacid electrodes for electrochemical energy storage. *Physical Chemistry Chemical Physics* **2013,** *15* (24), 9654-9662.

59. Huang, W.; Frech, R.; Wheeler, R., Molecular structures and normal vibrations of trifluoromethane sulfonate ($CF3SO3^-$) and its lithium ion pairs and aggregates. *Journal of Physical Chemistry* **1994,** *98* (1), 100-110.

60. Foley, M. P.; Worosz, C.; Sweely, K.; Henderson, W.; De Long, H.; Trulove, P. C., Phase behavior and solvation of lithium trifluoromethanesulfonate in propylene carbonate. *ECS Transactions* **2013,** *45* (29), 41-47.

61. Xu, K., Nonaqueous liquid electrolytes for lithium-based rechargeable batteries. *Chemical Reviews* **2004,** *104* (10), 4303-4418.

62. Payne, R.; Theodorou, I. E., Dielectric properties and relaxation in ethylene carbonate and propylene carbonate. *Journal of Physical Chemistry.* **1972,** *76* (20), 2892-2900.

63. Baradwaj, A. G.; Rostro, L.; Alam, M. A.; Boudouris, B. W., Quantification of the solid-state charge mobility in a model radical polymer. *Applied Physics Letters* **2014,** *104*.

64. Ue, M., Mobility and ionic association of lithium and quaternary ammonium salts in propylene carbonate and γ -butyrolactone. *Journal of the Electrochemical Society* **1994,** *141* (12), 3336-3342.

65. Ue, M.; Mori, S., Mobility and ionic association of lithium salts in a propylene carbonate - ethyl methyl carbonate mixed solvent. *Journal of the Electrochemical Society* **1995,** *142* (8), 2577-2581.

66. Lutkenhaus, J., A radical advance for conducting polymers. *Science* **2018,** *359* (6382), 1334-1335.

67. Kemper, T. W.; Gennett, T.; Larsen, R. E., Molecular dynamics simulation study of solvent and state of charge effects on solid-phase structure and counterion binding in a nitroxide radical containing polymer energy storage material. *Journal of Physical Chemistry C* **2016,** *120* (45), 25639-25646.

68. Kemper, T. W.; Larsen, R. E.; Gennett, T., Relationship between molecular structure and electron transfer in a polymeric nitroxyl-radical energy storage material. *Journal of Physical Chemistry C* **2014,** *118* (31), 17213-17220.

69. Bobela, D. C.; Hughes, B. K.; Braunecker, W. A.; Kemper, T. W.; Larsen, R. E.; Gennett, T., Close packing of nitroxide radicals in stable organic radical polymeric materials. *Journal of Physical Chemistry Letters* **2015,** *6* (8), 1414-1419.

70. Nakahara, K.; Oyaizu, K.; Nishide, H., Electrolyte anion-assisted charge transportation in poly(oxoammonium cation/nitroxyl radical) redox gels. *Journal of Materials Chemistry* **2012,** *22* (27), 13669-13673.

71. Hauffman, G.; Rolland, J.; Bourgeois, J.-P.; Vlad, A.; Gohy, J.-F., Synthesis of nitroxide-containing block copolymers for the formation of organic cathodes. *Journal of Polymer Science Part A: Polymer Chemistry* **2013,** *51* (1), 101-108.

72. Bertrand, O.; Ernould, B.; Boujioui, F.; Vlad, A.; Gohy, J.-F., Synthesis of polymer precursors of electroactive materials by SET-LRP. *Polymer Chemistry* **2015,** *6* (33), 6067-6072.

73. Zhang, K.; Hu, Y.; Wang, L.; Fan, J.; Monteiro, M. J.; Jia, Z., The impact of the molecular weight on the electrochemical properties of poly (TEMPO methacrylate). *Polymer Chemistry* **2017,** *8* (11), 1815-1823.

74. Zheng, L.; Mukherjee, S.; Wang, K.; Hay, M. E.; Boudouris, B. W.; Gong, X., Radical polymers as interfacial layers in inverted hybrid perovskite solar cells. *Journal of Materials Chemistry A* **2017,** *5* (45), 23831-23839.

75. Ibe, T.; Frings, R. B.; Lachowicz, A.; Kyo, S.; Nishide, H., Nitroxide polymer networks formed by Michael addition: on site-cured electrode-active organic coating. *Chemical Communications* **2010,** *46* (20), 3475-3477.

76. Janoschka, T.; Teichler, A.; Häupler, B.; Jähnert, T.; Hager, M. D.; Schubert, U. S., Reactive inkjet printing of cathodes for organic radical batteries. *Advanced Energy Materials* **2013,** *3* (8), 1025-1028.

77. Ellis, B., *Chemistry and technology of epoxy resins*. Springer: 1993.

78. Takahashi, K.; Korolev, K.; Tsuji, K.; Oyaizu, K.; Nishide, H.; Bryuzgin, E.; Navrotskiy, A.; Novakov, I., Facile grafting-onto-preparation of block copolymers of TEMPO and glycidyl methacrylates on an oxide substrate as an electrode-active layer. *Polymer* **2015,** *68*, 310-314.

79. Qian, J.; Wiener, C. G.; Zhu, Y.; Vogt, B. D., Swelling and plasticization of polymeric binders by Li-containing carbonate electrolytes using quartz crystal microbalance with dissipation. *Polymer* **2018,** *143*, 237-244.

80. Wang, F.; Varenne, F.; Ortiz, D.; Pinzio, V.; Mostafavi, M.; Le Caër, S., Degradation of an ethylene carbonate/diethyl carbonate mixture by using ionizing radiation. *ChemPhysChem* **2017,** *18* (19), 2799-2806.

81. Nishide, H.; Iwasa, S.; Pu, Y.-J.; Suga, T.; Nakahara, K.; Satoh, M., Organic radical battery: nitroxide polymers as a cathode-active material. *Electrochimica Acta* **2004,** *50* (2–3), 827-831.

82. Ehlers, J.-E.; Rondan, N. G.; Huynh, L. K.; Pham, H.; Marks, M.; Truong, T. N., Theoretical study on mechanisms of the epoxy− amine curing reaction. *Macromolecules* **2007,** *40* (12), 4370-4377.

83. Baradwaj, A. G.; Wong, S. H.; Laster, J. S.; Wingate, A. J.; Hay, M. E.; Boudouris, B. W., Impact of the addition of redox-active salts on the charge transport ability of radical polymer thin films. *Macromolecules* **2016,** *49* (13), 4784-4791.

84. Kim, J.-K.; Kim, Y.; Park, S.; Ko, H.; Kim, Y., Encapsulation of organic active materials in carbon nanotubes for application to high-electrochemical-performance sodium batteries. *Energy & Environmental Science* **2016,** *9* (4), 1264-1269.

85. Xie, Y.; Zhang, K.; Monteiro, M. J.; Jia, Z., Conjugated nitroxide radical polymers: synthesis and application in flexible energy storage devices. *ACS Applied Materials & Interfaces* **2019,** *11* (7), 7096-7103.

86. Li, F.; Gore, D. N.; Wang, S.; Lutkenhaus, J. L., Unusual internal electron transfer in conjugated radical polymers. *Angewandte Chemie International Edition* **2017,** *56* (33), 9856-9859.

87. Li, F.; Wang, S.; Zhang, Y.; Lutkenhaus, J. L., Electrochemical energy storage in poly(dithieno[3, 2-b:2',3'-d]pyrrole) bearing pendant nitroxide radicals. *Chemistry of Materials* **2018,** *30* (15), 5169-5174.

88. Fratini, S.; Nikolka, M.; Salleo, A.; Schweicher, G.; Sirringhaus, H., Charge transport in high-mobility conjugated polymers and molecular semiconductors. *Nature Materials* **2020**.

89. Paulsen, B. D.; Tybrandt, K.; Stavrinidou, E.; Rivnay, J., Organic mixed ionic–electronic conductors. *Nature Materials* **2020,** *19* (1), 13-26.

90. Muench, S.; Wild, A.; Friebe, C.; Häupler, B.; Janoschka, T.; Schubert, U. S., Polymer-based organic batteries. *Chemical Reviews* **2016,** *116* (16), 9438-9484.

91. Kunz, T. K.; Wolf, M. O., Electrodeposition and properties of TEMPO functionalized polythiophene thin films. *Polymer Chemistry* **2011,** *2* (3), 640-644.

92. Almubayedh, S.; Chahma, M. h., Electrosynthesis and characterization of stable radical-functionalized oligo/polythiophenes. *New Journal of Chemistry* **2015,** *39* (10), 7738-7741.

93. Xu, L.; Yang, F.; Su, C.; Ji, L.; Zhang, C., Synthesis and properties of novel TEMPO-contained polypyrrole derivatives as the cathode material of organic radical battery. *Electrochimica Acta* **2014,** *130*, 148-155.

94. Lu, J.-j.; Ma, J.-q.; Yi, J.-m.; Shen, Z.-l.; Zhong, Y.-j.; Ma, C.-a.; Li, M.-c., Electrochemical polymerization of pyrrole containing TEMPO side chain on Pt electrode and its electrochemical activity. *Electrochimica Acta* **2014,** *130*, 412-417.

95. Casado, N.; Hernández, G.; Veloso, A.; Devaraj, S.; Mecerreyes, D.; Armand, M., PEDOT radical polymer with synergetic redox and electrical properties. *ACS Macro Letters* **2016,** *5* (1), 59-64.

96. Katsumata, T.; Satoh, M.; Wada, J.; Shiotsuki, M.; Sanda, F.; Masuda, T., Polyacetylene and polynorbornene derivatives carrying TEMPO. Synthesis and properties as organic radical battery materials. *Macromolecular Rapid Communications* **2006,** *27* (15), 1206-1211.

97. Qu, J.; Katsumata, T.; Satoh, M.; Wada, J.; Masuda, T., Synthesis and properties of polyacetylene and polynorbornene derivatives carrying 2,2,5,5-tetramethyl-1-pyrrolidinyloxy moieties. *Macromolecules* **2007,** *40* (9), 3136-3144.

98. Assumma, L.; Kervella, Y.; Mouesca, J. M.; Mendez, M.; Maurel, V.; Dubois, L.; Gutel, T.; Sadki, S., A New conducting copolymer bearing electro-active nitroxide groups as organic electrode materials for batteries. *ChemSusChem* **2020,** *13* (9), 2419-2427.

99. Chiang, C.; Blubaugh, E.; Yap, W., Electrochemical studies on doping of polyacetylene. *Polymer* **1984,** *25* (8), 1112-1116.

100. Zhang, Y.; Park, A. M.; McMillan, S. R.; Harmon, N. J.; Flatté, M. E.; Fuchs, G. D.; Ober, C. K., Charge transport in conjugated polymers with pendent stable radical groups. *Chemistry of Materials* **2018,** *30* (14), 4799-4807.

101. Shaoyang Wang, A. M. G. P., Paraskevi Flouda, Alexandra D. Easley, Fei Li, Ting Ma, Gregory D. Fuchs, and Jodie L. Lutkenhaus, Solution-processable thermally crosslinked organic radical polymer battery cathodes. *ChemSusChem* **2020**.

102. Waltman, R. J.; Bargon, J.; Diaz, A., Electrochemical studies of some conducting polythiophene films. *The Journal of Physical Chemistry* **1983,** *87* (8), 1459-1463.

103. Chen, X.; Inganäs, O., Three-step redox in polythiophenes: Evidence from electrochemistry at an ultramicroelectrode. *The Journal of Physical Chemistry* **1996,** *100* (37), 15202-15206.

104. Ryu, K. S.; Lee, Y.; Han, K.-S.; Kim, M. G., The electrochemical performance of polythiophene synthesized by chemical method as the polymer battery electrode. *Materials Chemistry and Physics* **2004,** *84* (2-3), 380-384.

105. Mike, J. F.; Shao, L.; Jeon, J.-W.; Lutkenhaus, J. L., Charge storage in decyl- and 3,6,9-trioxadecyl-substituted poly(dithieno[3,2-b:2,3-d]pyrrole) electrodes. *Macromolecules* **2013,** *47* (1), 79-88.

106. Sathiya, M.; Prakash, A.; Ramesha, K.; Tarascon, J. M.; Shukla, A. K., V_2O_5-anchored carbon nanotubes for enhanced electrochemical energy storage. *Journal of the American Chemical Society* **2011,** *133* (40), 16291-16299.